UNIVERSITY OF CALIFORNIA, SAN DIEGO

Non-destructive and Semi-destructive Methods for Thermal Stress Measurement in Continuous Welded Rails

A dissertation submitted in partial satisfaction of the requirements for the degree
Doctor of Philosophy

in

Structural Engineering

by

Xuan Zhu

Committee in Charge:

Professor Francesco Lanza di Scalea, Chair
Professor Kenneth J. Loh
Professor Daniele Micciancio
Professor Michael D. Todd
Professor Chia-Ming Uang

2016

The Dissertation of Xuan Zhu is approved, and it is acceptable in quality and form for publication on microfilm and electronically:

_____

_____

_____

_____

_____

Chair

University of California, San Diego

2016

DEDICATION

To my parents, my brother, and my wife for their constant love and encouragement.

TABLE OF CONTENTS

LIST OF FIGURES

LIST OF TABLES

ACKNOWLEGEMENTS

I would like to express my deepest and most sincere gratitude towards to Dr. Francesco Lanza di Scalea for his guidance and support in the past five years. He provided an inspiring and flexible environment for embracing and experimenting different ideas. It has been a great experience to work with and learn from him in the aspects of time management and mental toughness. I would also thank him for all of his input on this dissertation and his role in getting this document into its final form.

Special thanks are given to all the members of my doctoral committee, Professors Kenneth J. Loh, Daniele Micciancio, Michael D. Todd and Chia-Ming Uang who dedicated their time to help me with the technical issues related to my research. Professor Todd is acknowledged for his guidance and insights on the electromechanical impedance modeling; Professor Uang is acknowledged in particular for his advice on experimental setup and residual stress measurement.

I am grateful also to Professor Piervincenzo Rizzo from University of Pittsburgh, who strongly recommended me to work with Prof. Lanza di Scalea. Thanks to all the colleagues present and past in the NDE/SHM Laboratory: Dr. Arun Manohar, Dr. Claudio Nucera, Dr. Jeff Tippmann, Dr. Stefano Mariani, Dr. Thompson Nguyen, Dr. Piotr Kijanka, Simone Sternini, Margherita Capriotti and Yichao Yang for their technical inputs, humor and

friendship. A special thanks to Dr. Robert Phillips for his invaluable help and mentorship during my first two years at UCSD. I wish to thank my friends at the structural engineering department of UCSD: Dr. Zhu Mao, Dr. Xiaowei Deng, Dr. Yong Li, Dr. Hefu Pu, Dr. Weian Liu, Dr. Xiang Wang, Dr. Jinhui Yan and Yewei Zheng. Additionally I want to recognize the staff of the Powell laboratories on campus: Paul Greco, Dr. Christopher Latham, and Noah Aldrich, Darren McKay for their help and assistance in my experiments.

The most sincere and deepest gratitude to my loving family: Xiaolin Zhu, Xiaofang Shi, and Longcheng Zhu for their love, care and encouragement. Without them, the pursuit of my dream in U.S. would become unnecessary. I am most grateful to my wife Yangyuan Chen, for her love, patience and confidence to support me during this journey.

The research presented within this thesis was partially funded by the U.S. Federal Railroad Administration under University grant# FR-RRD-0059-14-01with Mahmood Fateh from the FRA Office of Research and Development as the Program Manager. It was also partially funded by the Dissertation fellowship from engineering department of UCSD.

Chapter 2, in part, has been accepted for publication by Experimental Mechanics, Zhu, Xuan; Lanza di Scalea, Francesco; (2016). The title of this paper is *Sensitivity to Axial Stress of Electro-Mechanical Impedance Measurements*. The dissertation author was the primary investigator and primary author of this paper.

Chapter 3, in part, is currently in preparation for submission to the Journal of Intelligent Material Systems and Structures, Zhu, Xuan; Lanza di Scalea, Francesco; (2016). The running title of this paper is *Thermal Stress Measurement Using the Electro-Mechanical Impedance Method and its application in Continuous Welded Rails*. The dissertation author will be the primary investigator and primary author of this paper.

Chapter 4, in part, has been accepted for publication by Experimental Mechanics, Zhu, Xuan; Lanza di Scalea, Francesco; (2016). *Thermal Stress Measurement in Continuous Welded Rails Using the Hole-Drilling Method.* The dissertation author was the primary investigator and primary author of this article.

VITA

2008	Bachelor Degree in Mechanical Engineering, Beijing University of Aeronautics and Astronautics, China
2008-2010	Research Assistant, University of Pittsburgh
2010	Master of Science, University of Pittsburgh
2011-2016	Research Assistant, University of California, San Diego
2016	Doctor of Philosophy, University of California, San Diego

JOURNAL ARTICLES

1. Mariani, S., Nguyen, T. V., Zhu, X., Lanza di Scalea, F. "Field Test Performance of Non-contact Ultrasonic Rail Inspection System," in process for *Journal of Transportation Engineering (ASCE)*

2. Zhu, X., Lanza di Scalea, F. "Thermal stress characterization using the Impedance-based Structural Health Monitoring system," in process for *Journal of Intelligent Material Systems and Structures*

3. Zhu, X., Lanza di Scalea, F. "Thermal Stress Measurement in Continuous Welded Rails Using the Hole-Drilling Method," *Experimental Mechanics* (accepted)

4. Zhu, X., Lanza di Scalea, F. "Sensitivity to Axial Stress of Electro-Mechanical Impedance Measurements," *Experimental Mechanics* (accepted)

5. Kijanka, P., Packo, P., Zhu, X., Staszewski, W., Lanza di Scalea, F. (2015) "Three-Dimensional Temperature Effect Modelling of Piezoceramic Transducers Used for Lamb

Wave Based Damage Detection," *Smart Materials and Structures*, 24 (6), 0605005.

6. Tippmann, J. D., Zhu, X., Lanza di Scalea, F. (2015) “Application of damage detection methods using passive reconstruction of impulse response functions,” *Philosophical Transactions of the Royal Society A Mathematical Physical and Engineering Sciences*, 373(2035).

7. Zhu, X., Rizzo, P. (2014) “Sensors Array for the Health Monitoring of Truss Structures by means of Guided Ultrasonic Waves,” *Journal of Civil Structural Health Monitoring*, Volume 4, Issue 3, 221-234

8. Zhu, X., Rizzo, P. (2013) “Guided Ultrasonic Waves for the Health Monitoring of sign Support Structures Under Varying Environmental Conditions,” *Structural Control and Health Monitoring*, Volume 20, Issue 2, pp. 156–172, February.

9. Phillips, R., Zhu, X., Lanza di Scalea, F. (2012) “The Influence of Stress on Electro-mechanical Impedance Measurements in Rail Steel,” *Material Evaluation*, Oct. Vol. 70, No. 10, 1213-1218.

10. Zhu, X., Rizzo, P. (2012) “‘A unified approach for the structural health monitoring of waveguides,” *Structural Health Monitoring*, August, doi:10.1177/1475921712438569.

11. Zhu, X., Rizzo, P., Marzani, A., and Bruck, J. (2010) “Ultrasonic Guided Waves for NDE/SHM of Trusses,” *Measurement Science and Technology*, 21, 045701, doi: 10.1088/0957-0233/21/4/045701.

ABSTRACT OF THE DISSERTATION

Non-destructive and Semi-destructive Methods for Thermal Stress Measurement in Continuous Welded Rails

by

Xuan Zhu

Doctor of Philosophy in Structural Engineering

University of California, San Diego, 2016

Professor Francesco Lanza di Scalea, Chair

In-situ stress determination in structures under environmental variability without a reference value is a challenging experimental mechanics task. One potential application of this task is the management of longitudinal loads in railroad structures: the absence of expansion

joints in Continuous Welded Rail (CWR) has created the need for the railroad industry to determine the *in-situ* thermal stress levels for rail buckling and breakage prevention.

This dissertation examines the potentials of a nondestructive method, namely the Electro-Mechanical Impedance (EMI) method, and a semi-destructive method, the hole-drilling method, to provide an estimation of the axial stress state of the in-service structures. The EMI method is completely non-destructive, as it simply involves bonding a piezoelectric element on the host structure and measuring the electrical admittance signature of the PZT-structure assembly in selected frequency ranges. This non-invasive approach features easiness of implementation and interpretation, while it is notoriously known for being vulnerable to environmental variability. A comprehensive analytical model is proposed to relate the measured electric admittance signatures to uniaxial applied stress and temperature, respectively, as functions of relevant parameters of the EMI monitoring system. The model results compare favorably to the experimental ones, where the sensitivities of features extracted from the admittance signatures to the varying stress levels and temperatures are determined. Temperature compensation algorithms are proposed, and the final results illustrate that the frameworks are capable of eliminating the temperature effect and highlighting the ones from the thermally-induced stress.

On the other hand, the semi-destructive hole-drilling method is explored as a possible alternate solution for thermal stress measurement. A new set of calibration coefficients to

compute the stress field relieved by fine hole depth increments required by the high strength steel is determined. The new calibration coefficients are experimentally validated on an aluminum plate subjected to a known uniaxial load. The thermal stress levels of constrained rails are estimated after compensation for the residual stress components, based on statistical relationships developed experimentally between the longitudinal and the vertical residual stresses. The results show that the hole-drilling procedure, with appropriate calibration coefficients and residual stress compensation, can estimate the *in-situ* rail thermal stresses, and therefore the neutral temperature of the CWR, with an expected accuracy that is within the industry acceptable levels.

1. Introduction

In-situ stress determination in structures without a reference value is a challenging experimental mechanics task. This dissertation examines the potentials of a nondestructive approach, namely the electro-mechanical impedance (EMI) method, and a semi-destructive test procedure, the hole-drilling method, to estimate the stress state for the in-service structures. One potential application of this task is the management of longitudinal loads in railroad structures. In this chapter, the background of the EMI method and the hole-drilling test procedure is reviewed. Then it states the motivation of the research, which is the thermal stress measurement for Continuous Welded Rail (CWR). Finally, the outline of the dissertation is presented.

1.1 Background

1.1.1 Basics of the electromechanical impedance method

Structural Health Monitoring (SHM) has attracted the researchers' focus as a solution to monitor and assess the aging infrastructure systems all over the world. As one of the emerging technologies, the Electro-Mechanical Impedance (EMI) method was introduced in early 1990s [1-3] and has great number of potential applications in the SHM of civil, mechanical and aerospace industries.

The EMI method is an active sensing technique that determines the local dynamic stiffness of the host structure by measuring the electrical impedance (or admittance) of a bonded lead zirconate titanate (PZT) element [1-7]. The electrical admittance of the bonded PZT patch is a function of the stiffness, mass, and damping of the host structure, the length, width, thickness, orientation, and mass of the PZT patch, as well as the adhesive utilized to bond the PZT to the structure.

To demonstrate how the electrical admittance of the bonded PZT is associated to structural conditions, the one-dimensional model of electro-mechanical coupling mechanism [4] is reviewed (Fig. 1.1).

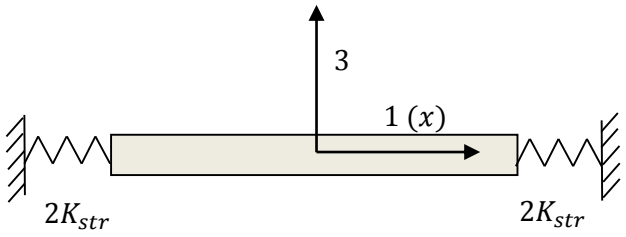

Figure 1.1 PZT wafer constrained by structural stiffness

Consider a PZT patch of length l_{PZT}, thickness h_{PZT}, and width b_{PZT}, undergoing longitudinal expansion u_1, induced by the thickness polarization electric field E_3. The electric field is produced by the application of a harmonic voltage $V(t) = \hat{V}e^{i\omega t}$ between the top and bottom surfaces. The resulting electric field $E = V/h_{PZT}$ is assumed constant through the thickness (direction 3). The PZT-structural dynamic interaction is determined by coupling the

constitutive relation of the PZT and the structure with their equations of motion. The linear constitutive relations of the PZT (T, E type) can be represented as:

$$\begin{cases} S_1 = s_{11}^E T_1 + d_{31} E_3 \\ D_3 = \varepsilon_{33}^T E_3 + d_{31} T_1 \end{cases} \tag{1.1}$$

where S_1 is the strain, T_1 is the stress, D_3 is the electric displacement, s_{11}^E is the mechanical compliance at zero field, ε_{33}^T is the dielectric constant at zero stress, d_{31} is the piezoelectric parameter.

Considering the force equilibrium at the boundaries:

$$T_1\left(\frac{l_{PZT}}{2}\right) b_{PZT} h_{PZT} = -2K_{str} u_1\left(\frac{l_{PZT}}{2}\right) \tag{1.2}$$

$$T_1\left(-\frac{l_{PZT}}{2}\right) b_{PZT} h_{PZT} = 2K_{str} u_1\left(-\frac{l_{PZT}}{2}\right) \tag{1.3}$$

Substituting Eqs. (1.2) and (1.3) into Eq. (1.1), the strains at both ends of the PZT patch can be represented as:

$$u_1'\left(\frac{l_{PZT}}{2}\right) = -s_{11}^E \frac{2K_{str}}{b_{PZT} h_{PZT}} u_1\left(\frac{l_{PZT}}{2}\right) + d_{31} E_3 \tag{1.4}$$

$$u_1'\left(-\frac{l_{PZT}}{2}\right) = s_{11}^E \frac{2K_{str}}{b_{PZT} h_{PZT}} u_1\left(-\frac{l_{PZT}}{2}\right) + d_{31} E_3 \tag{1.5}$$

where $'$ means first derivative with respect to x.

Before taking further steps, the quasi-static stiffness of the PZT active sensor is introduced as $K_{PZT} = \frac{A_{PZT}}{s_{11}^E l_{PZT}} = \frac{b_{PZT} h_{PZT}}{s_{11}^E l_{PZT}}$, and the stiffness ratio can be computed as $r = K_{str}/K_{PZT}$. Reorganizing Eqs. (1.4) and (1.5):

$$u_1'\left(\frac{l_{PZT}}{2}\right) + \frac{r}{\frac{l_{PZT}}{2}} u_1\left(\frac{l_{PZT}}{2}\right) = d_{31} E_3 \tag{1.6}$$

$$u_1'\left(-\frac{l_{PZT}}{2}\right) - \frac{r}{l_{PZT}/2} u_1\left(-\frac{l_{PZT}}{2}\right) = d_{31} E_3 \tag{1.7}$$

From Newton's law of motion, $T_1' = \rho \ddot{u}_1$, and knowing $S_1 = u_1'$. Apply this to Eq. (1.1), $S_1 = s_{11}^E T_1 + d_{31} E_3$, and taking the first derivative with respect to x:

$$\ddot{u}_1 = \frac{1}{s_{11}^E \rho_{PZT}} u_1'' \tag{1.8}$$

where $c^2 = \frac{1}{s_{11}^E \rho_{PZT}}$.

The general solution of Eq. (1.8) is: $u_1(x,t) = [C_1 \sin(\gamma x) + C_2 \cos(\gamma x)] e^{i\omega t}$, where $\gamma = \frac{\omega}{c}$. Substituting this general solution into Eqs. (1.6) and (1.7), yields:

$$\gamma \left[C_1 \cos\left(\gamma \frac{l_{PZT}}{2}\right) - C_2 \sin\left(\gamma \frac{l_{PZT}}{2}\right) \right] + \frac{r}{l_{PZT}/2} \left[C_1 \sin\left(\gamma \frac{l_{PZT}}{2}\right) + C_2 \cos\left(\gamma \frac{l_{PZT}}{2}\right) \right] = d_{31} E_3$$

$$\gamma \left[C_1 \cos\left(\gamma \frac{l_{PZT}}{2}\right) + C_2 \sin\left(\gamma \frac{l_{PZT}}{2}\right) \right] - \frac{r}{l_{PZT}/2} \left[-C_1 \sin\left(\gamma \frac{l_{PZT}}{2}\right) + C_2 \cos\left(\gamma \frac{l_{PZT}}{2}\right) \right] = d_{31} E_3$$

Reorganizing the equation system to compute the coefficients C_1 and C_2.

$$C_1[\varphi \cos(\varphi) + r \sin(\varphi)] - C_2[\varphi \sin(\varphi) - r \cos(\varphi)] = d_{31} E_3 \frac{l_{PZT}}{2} \tag{1.9}$$

$$C_1[\varphi \cos(\varphi) + r \sin(\varphi)] + C_2[\varphi \sin(\varphi) - r \cos(\varphi)] = d_{31} E_3 \frac{l_{PZT}}{2} \tag{1.10}$$

where $\varphi = \frac{1}{2} \gamma l_{PZT}$.

Solving the above equations, the displacement along direction 1 (along the x axis) is:

$$u_1(x,t) = \hat{u}_1(x) e^{i\omega t} = \frac{1}{2} d_{31} E_3 l_{PZT} \frac{\sin(\gamma x)}{\varphi \cos(\varphi) + r \sin(\varphi)} e^{i\omega t}$$

Thus, based on Eq. (1.1), the electric displacement field of the PZT patch can be obtained as:

$$D_3 = \varepsilon_{33}^T E_3 \left[1 + \frac{d_{31}^2}{s_{11}^E \varepsilon_{33}^T} \left(\frac{u_1'}{d_{31} E_3} - 1 \right) \right] \tag{1.11}$$

The generated electric charge can be computed by integrating the electric displacement over the area of the PZT patch,

$$Q_3 = \int_{-l_{PZT}/2}^{l_{PZT}/2} \int_{-b_{PZT}/2}^{b_{PZT}/2} D_3 \, dx \, dy = CV \left[1 - \frac{d_{31}^2}{s_{11}^E \varepsilon_{33}^T} \left(1 - \frac{1}{\varphi \cot(\varphi) + r} \right) \right] e^{i\omega t} \quad (1.12)$$

where $C = \varepsilon_{33}^T \frac{b_{PZT} l_{PZT}}{h_{PZT}}$ is the capacitance of the PZT patch.

Given the generated electric charges, the electric current can be calculated by taking the first derivative of the electric charges with respect to time: $I = i\omega e^{i\omega t} \iint D_3 dx dy$. Since the electric field is $E = V/h_{PZT}$, the admittance (inverse of impedance), Y = I/V, is found as:

$$Y = i\omega C \left[1 - K_{31}^2 \left(1 - \frac{1}{\varphi \cot(\varphi) + r} \right) \right] \quad (1.13)$$

In summary, $C = \varepsilon_{33}^T \frac{b_{PZT} l_{PZT}}{h_{PZT}}, K_{31}^2 = \frac{d_{31}^2}{s_{11}^E \varepsilon_{33}^T}, \varphi = \frac{1}{2} \gamma l_{PZT}, r = \frac{K_{str}}{K_{PZT}}, \gamma = \frac{\omega}{c}, c^2 = \frac{1}{s_{11}^E \rho_{PZT}}$, ρ_{PZT} is the density of the PZT, $b_{PZT}, l_{PZT}, h_{PZT}$ are the geometry of the PZT actuator, ω is the excitation frequency, d_{31} is the PZT piezoelectric constant, ε_{33}^T is the PZT complex dielectric constant at zero stress, s_{11}^E is the PZT complex compliance modulus at zero electric field, K_{str} and K_{PZT} are the structural stiffness of PZT and structure, respectively. Eq. (1.13) clearly shows that the electrical admittance of the PZT is directly related to the structural stiffness of the host structure. Assuming that the mechanical properties of the PZT do not change during the measurement period, variations in the electrical impedance signatures are related to variations of the structural mechanical impedance. In turn, the structural mechanical impedance is a function of mass, stiffness, damping, boundary conditions and applied stress.

1.1.2 Introduction of the hole-drilling method

The hole-drilling method, a semi-destructive test procedure first introduced by Mathar in the 1930s [8], is one of the most widely used approaches to determine near-surface *in-situ* stresses (most typically residual stresses). This method features good accuracy and reliability [9], ASTM standardized test procedures [10, 11], and well-established practical implementations [12]. The small drilled holes are often tolerable and/or repairable [13].

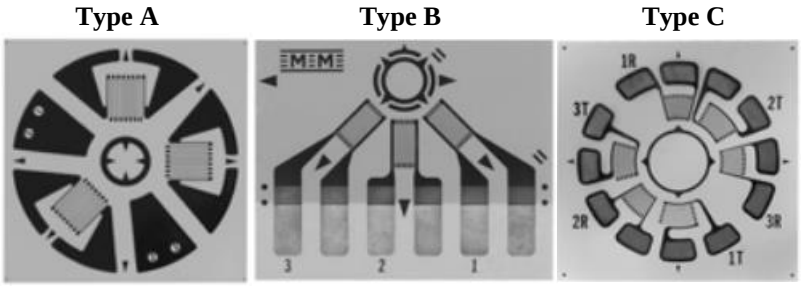

Figure 1.2 Type A, B and C Hole-Drilling Rosettes [12]

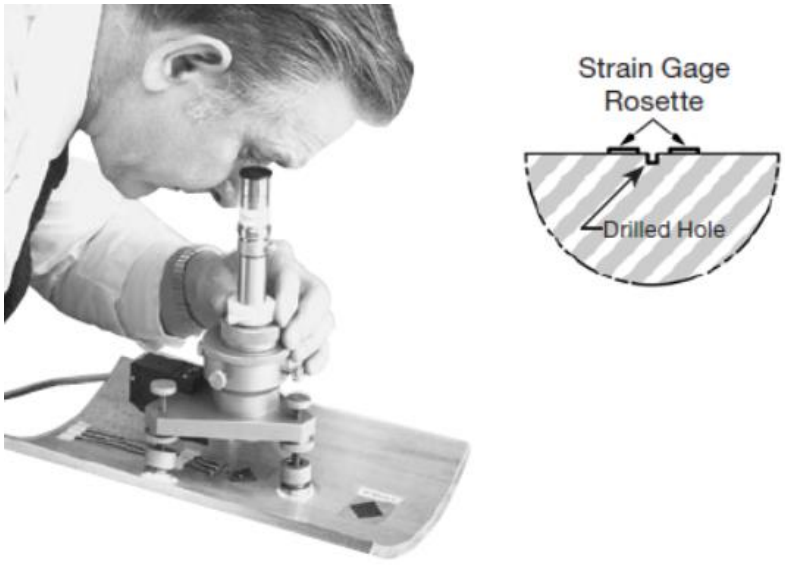

Figure 1.3 Implementation of the Hole-Drilling method [12]

Early works in the 1960s and 1970s demonstrated the method's effectiveness and accuracy (better than $\pm$8% for steel) for the measurement of near-surface residual stresses in elastic materials [9, 14]. At that time, the calibration coefficients were computed based on experimental results and empirical relationships for given hole diameters. In the 1980s, Schajer [15, 16] proposed a systematic framework to compute the calibration coefficients for the cases of uniformly and non-uniformly distributed residual stresses along the hole depth, based on the principle of superposition and axisymmetric finite element models. In these models, the non-axisymmetric loads necessary to compute some of the coefficients were handled by special 2D finite elements that used Fourier series expansion in the circumferential direction. Other researchers [17, 18] calculated the calibration coefficients by using a 3-D finite element model with an integral method and verified the coefficients with experimental results. From the perspective of implementation, it has been a convenient, economic, and less-invasive method for measuring the residual stresses near the surface of the specimen. For *in-situ* stress measurement applications, the hole-drilling method would be one of most favorable candidates among the stress relaxation methods, since it has the least influence on the mechanical performance of the specimen and would barely affect the in-service structural elements. In general, the hole-drilling test procedure for the specimens with uniform stress distribution along the hole depth is composed by four steps:

a. Applying a series of gentle mechanical and chemical treatments on the specimen

surface to ensure the effective load transfer and a clean environment for adhesive curing [12], where locations close to the edges or structural irregularities should be avoided in order to eliminate the boundary effects on the stress relaxation.

b. Attaching the special standardized strain gage rosettes with gage circle surrounded by 3 single or pairs of gage elements, as shown in Fig. 1.2, to the prepared surface. Based on the locations and applications with requirements on strain sensitivity and thermal stability, the choices of the gage patterns and sizes can be made.

c. Drilling a hole targeted at the center of the gage circle with finite depth steps, as shown in Fig. 1.3, and recording the strains at each incremental depth, depending on the gage size and the assumption of a uniform stress distribution along the drilling depth.

d. Computing the stress relaxation with the calibration coefficients by weighted averaging over the strain records along the depth for the case of uniform stress distribution [10,11].

For the case of uniform stress through the thickness, the stresses relaxed by drilling the hole are computed with weighted averages of strain recordings along the hole depth. The original ASTM standard [10] suggests to drill a blind hole with an 8-step procedure for a thick workpiece, defined as a test piece with a thickness larger than 1.2 times the rosette circle's diameter. A 10-step procedure is presented in the 2013 edition of the ASTM standard [11]. The recorded strains from three strain gage elements at the i^{th} depth increment, $(\varepsilon_{1i}, \varepsilon_{2i}, \varepsilon_{3i})$, are converted into combination strains as:

$$\mathrm{p}_i = \frac{\varepsilon_{3i} + \varepsilon_{1i}}{2};\ \mathrm{q}_i = \frac{\varepsilon_{3i} - \varepsilon_{1i}}{2};\mathrm{t}_i = \frac{\varepsilon_{3i} + \varepsilon_{1i} - 2\varepsilon_{2i}}{2} \tag{1.14}$$

The combination stresses *P*, *Q* and *T* are then computed through the weighted averages of the combination strains at all the depths as:

$$P = -\frac{E}{1+\nu}\frac{\sum_i \bar{a}_i p_i}{\sum_i \bar{a}_i^2}; \quad Q = -E\frac{\sum_i \bar{b}_i q_i}{\sum_i \bar{b}_i^2}; \quad T = -E\frac{\sum_i \bar{b}_i t_i}{\sum_i \bar{b}_i^2} \tag{1.15}$$

where $\bar{a}_i$ and $\bar{b}_i$ are the calibration coefficients for the i^{th} hole depth increment. Averaging the various depth increments allows minimizing the effects of random strain measurement errors [19]. Given the combination stresses *P*, Q and *T*, the in-plane pre-drilling stresses can be finally computed as:

$$\sigma_x = P - Q; \quad \sigma_y = P + Q; \quad \sigma_{xy} = T \tag{1.16}$$

1.2 Research motivation

The specific application of interest to the present study is the *in-situ* measurement of thermal stresses in CWR, which is still an unresolved problem in railroad maintenance practice. Most modern railways use CWR, since it supports higher transporting speed, provides less friction and requires less maintenance. However, the absence of expansion joint can lead to tensile stresses in cold weather (danger of "broken rail") in cold winter and compressive stresses in warm summer (danger of "sun kink" or thermal buckling), as shown in Fig. 1.4. Track buckling in extreme weather can happen suddenly and without warning, which makes it difficult to detect ahead of time. According to the Federal Railroad Administration

(FRA) Safety Statistics for the period 2010 –2015 [20], for example, as the cause of train accidents, track alignment (buckled/'sun kink') ranks fifth in terms of number of accidents (150 derailments out of 152 incidents), and it ranks second in terms of associated damage cost ($85M) within the category of "Track, Roadbed and Structures".

Figure 1.4 (a) Continuous welded rail; (b) the 'sun kink' failure mode due to thermal buckling.

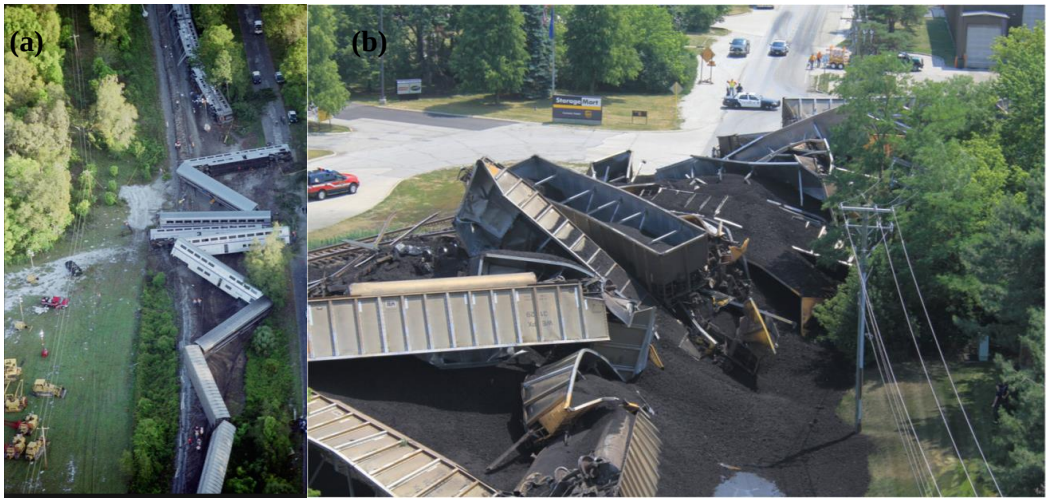

Figure 1.5 (a) 2002 Crescent City Amtrak derailment; (b) 2012 Northbrook UP derailment.

As shown in Fig. 1.5, the consequences can be catastrophic. On April 18, 2002, 21 cars of an Amtrak Auto-Train derailed near Crescent City, Florida. Four human deaths, 142 injured. The final report from National Transportation Safety Board determines that the accident was caused by a hot-weather "sun kink" misalignment of the track due to inadequate maintenance, and the estimated damages cost is about $8.3 million [21]. On July 4, 2012, at Pendleton, Texas, 43 loaded cars of the BNSF Railway coal train derailed [22]. The same day in Northbrook, Illinois, a sun kink caused 31 loaded coal cars on a Union Pacific (UP) Railroad train to derail, destroying the bridge and falling onto the roadway below, killing two people [23]. The high derailment rate and the destructive social and economic impact make this issue a high priority industrial goal to improve [24, 25].

The well-known formula that governs the development of thermal loads in CWR is [26]:

$$P(T, NT) = -\alpha\, E\, A\, (T - NT) \tag{1.17}$$

where P is the current (longitudinal) thermal load, α is the coefficient of thermal expansion of steel, E is the Young's Modulus of steel, A is the rail cross-sectional area, T is the current rail temperature, and NT is the so-called rail "Neutral Temperature". Knowledge of the rail Neutral Temperature (NT), which corresponds to the rail temperature when the rail has zero thermal stress, is of outmost importance to rail engineers because it allows to predict the thermal load, P, at any given rail temperature, T, from Eq. (1.17). Unfortunately, the rail NT changes during

the life of the track, due to a variety of reasons including track settlement, ballast settlement, and track repair/maintenance work. While a number of techniques have been proposed over the years for the *in-situ* measurement of the rail thermal stresses (or, equivalently, the rail NT), including rail uplifting or VERSE [27], magneto-elastic methods or MAPS [28], Rayleigh wave polarization measurements [29], nonlinear ultrasonic measurements [30] and neutron diffraction [31] among others, the railroad industry is still searching for an answer that can provide the necessary level of stress measurement accuracy, given the highly variable boundary conditions in the field and with minimum traffic disruption. This research need is clearly indicated by recent Broad Agency Announcements of the Federal Railroad Administration [24] and strategic industry initiatives [25].

1.3 Outline of the dissertation

The dissertation has been divided into 5 chapters, the contents of which are outlined below.

Chapter 1 is an overview of the concepts of the electro-mechanical impedance and the hole drilling method. It also outlines the main challenges posed by the thermal stress measurement in the Continuous Welded Rails. At the end, it defines the research motivation and industrial goal, which is to measure the rail Neutral Temperature for buckling and breakage prevention.

Chapter 2 presents a preliminary study of using the electro-mechanical impedance method for axial stress determination. An analytical model is first developed to explicitly account for the applied prestress in the EMI admittance signature of the PZT element bonded to the structure. The model is validated with the experimental results from the uniaxial loading test with an aluminum bar and a steel bar instrumented with PZT elements. The features including the structural resonances from the conductance spectra, the capacitance of the PZT, and the electric resonances of the measurement system are investigated with their stress sensitivity. It concludes that the EMI method can provide an estimation of the applied uniaxial stress.

Chapter 3 extends the modeling effort of Chapter 2 by considering the temperature variability. The model results provide accurate estimation of the temperature influences on the admittance signatures. It summarizes the experimental investigations performed at the UCSD/FRA rail neutral temperature testbed. Two extra features, the in-plane and out-of-plane PZT resonances are included in the feature analysis. Two temperature compensation algorithms are proposed to suppress the temperature effects and preserve the influences from the thermal stress.

Chapter 4 is dedicated to the application of the hole-drilling method on thermal stress determination for the Continuous Welded Rail. The feasibility study based on finite element analysis is first introduced. The updated calibration coefficients based on 3D model are

computed to accommodate the rail track implementation. A calibration procedure is proposed to compensate for the residual stress and its performance is validated with two AREMA rail sizes of UCSD's Powell lab large scale testbed.

Chapter 5, summarizes the research work performed, emphasizes the important original contributions and the findings of this dissertation, and discusses future research directions and recommendations.

2. Sensitivity to Axial Stress of Electro-Mechanical Impedance Measurements

2.1. Introduction

The Electro-Mechanical Impedance (EMI) method is an active sensing technique in the Non-Destructive Evaluation (NDE) and Structural Health Monitoring (SHM) fields to determine the local dynamic stiffness of the host structure by measuring the electrical impedance (or admittance) of a bonded lead zirconate titanate (PZT) element [1-6]. The electrical admittance of the bonded PZT patch is a function of the stiffness, mass, and damping of the host structure, the length, width, thickness, orientation, and mass of the PZT patch, as well as the adhesive utilized to bond the PZT to the structure.

In NDE/SHM, the EMI method has been most commonly applied to damage detection in structures. Giurgiutiu and Rogers [7], for example, showed the effectiveness of EMI to detect delimitations, cracks, and disbonds in composite plates. Park and Inman [5] applied EMI to monitoring the structural integrity of composite reinforced structures and bolted connections. Park et al. [32] applied the EMI method to sensor self-diagnostics with temperature compensation. Yang et al. [33] monitored damage progression in a plate using EMI. Kim et al. [34] applied EMI to pre-stress loss monitoring in tendon-anchorage connections. Their work was an effort to relate prestress loss to modal and EMI resonances,

with the EMI study consisting of an empirical effort that did not include a comprehensive theoretical model to consider PZT and host structure.

More recently, efforts were devoted to enable wireless communication, including work by Mascarenas et al. [35], who developed a low-cost EMI-based wireless sensor node based on an AD5933 microprocessor [36], and by Ho et al. [37] who developed an imote2-based multi-scale wireless system for tracking acceleration, strain and EMI admittance signatures with solar-power harvesting capabilities.

Some studies have been focused on the analytical modeling of the EMI method. Liang et al. [1, 2] developed the first coupled electro-mechanical analysis of PZT actuators integrated in a spring-mass-damper system to bridge the structural stiffness with the electrical admittance of the element. Zhou et al. [3] developed a dynamic model of distributed PZT actuators coupled with a two-dimensional structure. Yang et al. [38] proposed a novel simplified two-dimensional interactions of the PZT element with the host structure based on the concept of effective impedance. Giugiutiu and Zagrai [4, 39] developed the coupling model based on beam vibration combined with piezoelectricity to formulate the point-wise dynamic stiffness of the beam.

A much more limited literature exists on the application of the EMI method for *in-situ* measurement of applied stresses/loads in the host structure. Ong et al. [40] investigated the axial loading effect on the dynamic structural stiffness and impedance signature using an

Euler-Bernoulli beam model, relating axial loads to shifts in structural natural frequencies, and therefore PZT admittance signatures. Annamdas et al. [41] performed a comprehensive experimental study on the influence of load on the EMI method, confirming that the shifts in resonances of the PZT conductance (real part of the admittance) are proportional to the magnitude of applied uniaxial load and independent of the PZT excitation frequency. Furthermore, 'an anticlockwise rotation proportionally to the magnitude of the applied load' was observed in the PZT susceptance (imaginary part of the admittance). Similar findings were reported by Phillips et al. [42] and Lim et al. [43]. There is still a need to combine the effects of prestress on the structure, on the strain transfer to the PZT, and on the properties of the PZT element itself, in one explicit model that relates admittance signatures to stress levels.

This chapter derives an EMI formulation that explicitly accounts for the prestress level in the host structure by considering its effects on both the PZT element and the dynamics of the structure. The work investigates, both analytically and experimentally, the EMI conductance signature and susceptance signature (which is generally less understood) as potential metrics for *in-situ* axial load estimation in bar-like structures. This work is part of an effort to develop techniques able to estimate the level of longitudinal loads in CWR.

2.2 Influence of stress on the electro-mechanical impedance signatures

2.2.1 One-dimensional EMI model

This section briefly reviews the one-dimensional model for the EMI method [1-4], relating the local structural dynamic stiffness to the electrical admittance of the bonded PZT element, where the detailed derivation can be found in Section 1.1. The electrical admittance of a bonded PZT, as shown in Fig. 2.1, can be found as [4,39]:

$$Y = i\omega C\left[1 - K_{31}^2\left(1 - \frac{1}{\varphi\cot(\varphi) + r}\right)\right] \tag{2.1}$$

where $C = \varepsilon_{33}^T \frac{b_{PZT} l_{PZT}}{h_{PZT}}, K_{31}^2 = \frac{d_{31}^2 \mathrm{Y}_{PZT}^{\mathrm{E}}}{\varepsilon_{33}^T}, \varphi = \frac{1}{2}\gamma l_{PZT}, r = \frac{K_{str}}{K_{PZT}}, \gamma = \frac{\omega}{c}, c^2 = \frac{\mathrm{Y}_{PZT}^{\mathrm{E}}}{\rho_{PZT}}$, ρ_{PZT} is the density of the PZT, $b_{PZT}, l_{PZT}, h_{PZT}$ are the geometrical dimensions of the (rectangular) PZT, ω is the excitation frequency, $\mathrm{Y}_{PZT}^{\mathrm{E}} = \frac{1}{s_{11}^E}$ is the PZT elastic modulus at zero electric field, s_{11}^E is the PZT complex mechanical compliance at zero field, ε_{33}^T is the PZT dielectric constant at zero stress, d_{31} is the 3-1 PZT piezoelectric coefficient, K_{str} and K_{PZT} are the structural stiffness of the host structure and the PZT patch, respectively. Eq. (2.1) clearly shows that the admittance of the PZT is directly related to the stiffness of the host structure. When the structure (and therefore the PZT patch) is under quasi-static load, the load-sensitive parameters in Eq. (2.1) will induce a change in the PZT electrical signatures.

2.2.2 Influence of uniaxial stress on the piezoelectric elements

Considering a structure subjected to a uniaxial load, the stress developed in the bonded PZT patch depends on the PZT strain, the stiffness ratio between the structure and PZT, and

the shear modulus of the bonding layer. The shear-lag model by Crawley and de Luis [44] formulated the shear transfer mechanism using an Euler-Bernoulli beam and piezoelectricity, Fig. 2.1.

Considering a uniaxial quasi-static load applied to the structure, the strain at the surface of the structure, $S_{1,s}$, and the strain in a PZT element, $S_{1,PZT}$, can be computed as [44]:

$$\begin{cases} S_{1,s} = B_1 + B_2\dfrac{2x}{l_{PZT}} + B_3\sinh\left(\Gamma\dfrac{2}{l_{PZT}}x\right) + B_4\cosh\left(\Gamma\dfrac{2}{l_{PZT}}x\right) \\ S_{1,PZT} = B_1 + B_2\dfrac{2x}{l_{PZT}} + \dfrac{\Psi}{\alpha}B_3\sinh\left(\Gamma\dfrac{2}{l_{PZT}}x\right) - \dfrac{\Psi}{\alpha}B_4\cosh\left(\Gamma\dfrac{2}{l_{PZT}}x\right) \end{cases} \tag{2.2}$$

where Γ is the shear-lag parameter defined as $\Gamma^2 = \frac{G_b * l_{PZT}^2}{h_b}\left(\frac{1}{Y_{PZT}^E h_{PZT}} + \frac{\alpha}{E_s h_s}\right)$, $\Psi = \frac{E_s h_s}{\mathrm{Y}_{PZT}^{\mathrm{E}}\mathrm{h}_{PZT}}$, E_s and h_s are the Young's modulus and the thickness of the structure, G_b and h_b are the shear modulus and thickness of adhesive layer and the factor α is 1 or 3 for extensional or bending deformation. The constants B_1, B_2, B_3 and B_4 can be found by applying the boundary conditions at both ends of the PZT patch [45]: $S_{1,s} = \varepsilon$ and $S_{1,PZT} = 0$ at $x = \pm\frac{l_{PZT}}{2}$, which accounts for the static strain in the structure and for sensor ends free from normal stresses: $B_1 = \varepsilon\frac{\Psi}{\Psi+\alpha}, B_2 = B_3 = 0, B_4 = \varepsilon\frac{\alpha}{\Psi+\alpha}\mathrm{sech}(\Gamma)$. The PZT-structure strain ratio can be therefore expressed as:

$$\frac{S_{1,PZT}}{S_{1,s}} = \frac{\Psi}{\Psi+\alpha}\left[1 - \frac{\cosh\left(\Gamma\dfrac{2}{l_{PZT}}x\right)}{\cosh(\Gamma)}\right] \tag{2.3}$$

Given this study's interest in axial load, the relevant shear-lag parameter α is 1. The axial normal stress transferred from the structure to the PZT element can be calculated according to Hooke's law from the known normal strain transfer. Such transfer depends, among other factors, on the relative stiffness between the structure and the PZT. Representative values of normal strain transfer are shown in Fig. 2.2 for an aluminum and a steel structure that are the materials used in the experimental study discussed later in the paper. These results were computed from Eq. (2.3) using the values listed in Table 2.1 for the properties of the PZT element and the adhesive. The strain distribution of the type shown in this figure can then be used to modify accordingly the stress-sensitive properties of the PZT element.

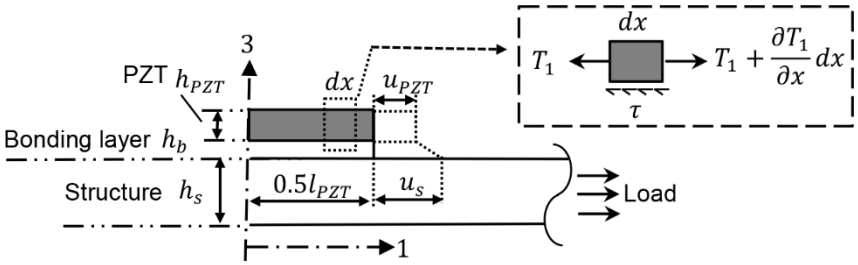

Figure 2.1 Stress transfer between an axially-preloaded structure and a bonded PZT rectangular patch.

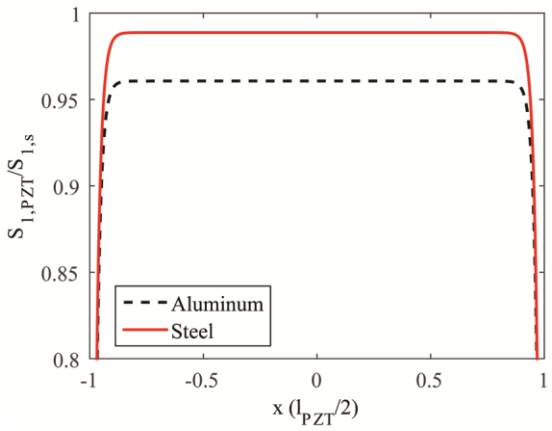

Figure 2.2 Ratio between strain in the PZT and in the host structure using the shear-lag model.

Considering the PZT material itself, it is known that high mechanical pre-stress or electric field can affect the piezoelectric behavior [46-60]. One way to account for these effects is to assume nonlinear piezoelectric constitutive equations. Thermodynamic considerations provide one approach to describe nonlinear piezoelectric constitutive relations [57, 58]. Another approach is to include the nonlinearity in the piezoelectric coupling constants [46-56, 59-60]. This behavior can be adequately represented by using effective elastic, dielectric and piezoelectric properties.

The following expressions are nonlinear constitutive relations that can be used to model the PZT element subjected to uniaxial stress along direction 1 with poling along direction 3 [53, 55]:

$$\begin{cases} S_1 = s_{11}^E T_1 + d_{31} E_3 + s_{111}^E T_1^2 + d_{311} T_1 E_3 + R_{331} E_3^2 \\ D_3 = d_{31} T_1 + \varepsilon_{33}^T E_3 + d_{311} T_1^2 + R_{331} T_1 E_3 + \varepsilon_{333}^T E_3^2 \end{cases} \tag{2.4}$$

where $s_{111}^{E}, d_{311}, R_{331}$ and ε_{333}^{T} are the nonlinear elastic, piezoelectric, electrostrictive and dielectric coefficients and the other terms were defined in previous equations. With both the pre-stress $\bar{T}_1$ and the (small) stress pertubation $\tilde{T}_1$ induced by the applied electric field, the overall stress field can be expressed as $T_1 = \bar{T}_1 + \tilde{T}_1$. The strain and electric displacement also consist of static and dynamic components: $S_1 = \bar{S}_1 + \tilde{S}_1$ and $D_3 = \bar{D}_3 + \tilde{D}_3$, respectively. The applied electric field E_3 will be $\tilde{E}_3$. Neglecting high order perturbation terms, the dynamic components of variables can be isolated to obtain the constitutive equations for the pre-stressed PZT element:

$$\begin{cases} \tilde{S}_1 = s_{11}^{eff}\tilde{T}_1 + d_{31}^{eff}\tilde{E}_3 \\ \tilde{D}_3 = d_{31}^{eff}\tilde{T}_1 + \varepsilon_{33}^{eff}\tilde{E}_3 \end{cases} \tag{2.5}$$

where $s_{11}^{eff} = s_{11}^{E}\left(1 + \frac{s_{111}^{E}}{s_{11}^{E}}\bar{T}_1\right), d_{31}^{eff} = d_{31}\left(1 + \frac{d_{311}}{d_{31}}\bar{T}_1\right)$ and $\varepsilon_{33}^{eff} = \varepsilon_{33}^{T}\left(1 + \frac{R_{331}}{\varepsilon_{33}^{T}}\bar{T}_1\right)$ are the effective elastic compliance, piezoelectric coefficient and dielectric permittivity. These effective properties are directly related to the applied stress, and are here formulated assuming a linear dependence on it. This assumption, therefore, is a first-order approximation of the PZT behavior. Some previous experimental studies [47, 48] confirmed a linear dependence of piezoelectric constants and dielectric permittivity of PZT materials with static applied stress, for certain load ranges. Specifically, for PZT-5A, ref. [48] found the normal in–plane stress sensitivity of ε_{33}^{T} as 97.4 $pF \cdot m^{-1}/ksi$ and that of d_{31} at 8.46e-12 $V \cdot m^{-1}/ksi$.

2.2.3 Modeling the point-wise dynamic stiffness

Given the electromechanical admittance model in Eq. (2.1) with effective stress-sensitive properties of Eq. (2.5), this section derives the structural stiffness K_{str} of an Euler-Bernoulli beam via eigenfunction expansion.

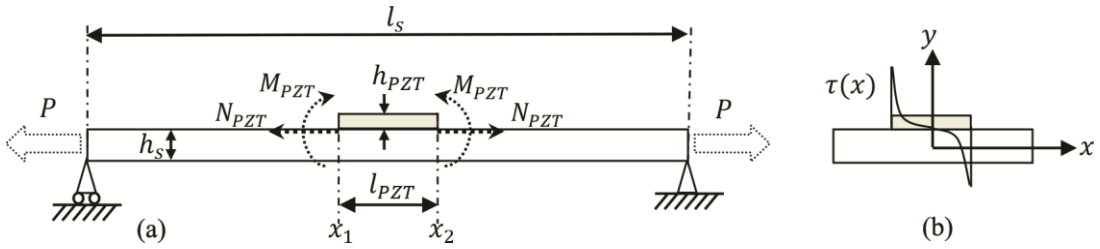

Figure 2.3 A simply supported beam subjected to axial preload and the hyperbolic stress applied by the PZT patch.

The problem addressed in this formulation is that of a simply supported beam, subjected to an axial preload, with a bonded PZT patch, Fig. 2.3(a). The origin of the coordinate system is located in the middle of the PZT, and the stress input distribution function from the actuator is represented by hyperbolic function according to shear-lag considerations [44, 45] and shown in Fig. 2.3(b). The axial force can be expressed as

$$N_{PZT}(x,t) = F_{PZT} N \sinh\left[\Gamma \frac{2}{l_{PZT}} x\right]\left[H\left(x + \frac{l_{PZT}}{2}\right) - H\left(x - \frac{l_{PZT}}{2}\right)\right] \mathrm{e}^{\mathrm{i}\omega \mathrm{t}} \qquad (2.6)$$

, and the bending moment can be expressed as

$$M_{PZT}(x,t) = \frac{F_{PZT}(h_s + h_{PZT})}{2} * N \sinh\left[\Gamma \frac{2}{l_{PZT}} x\right]\left[-H\left(x + \frac{l_{PZT}}{2}\right) + H\left(x - \frac{l_{PZT}}{2}\right)\right] \mathrm{e}^{\mathrm{i}\omega \mathrm{t}} \quad (2.7)$$

where F_{PZT} is the force exerted by the PZT patch, H is the Heaviside step function, $\frac{F_{PZT}(h_s+h_{PZT})}{2}$ is the magnitude of bending moment provided by PZT, $N = \frac{2\Gamma}{l_{PZT}}\frac{1}{\cosh[\Gamma]-1}$ is an energy normalization coefficient for the hyperbolic function, and the other terms were defined previously. The thickness of the bonding layer was considered negligible in this load calculation.

The longitudinal vibration of the beam under distributed force from the PZT loading at its surface can be computed first. The beam dynamic governing equation for the longitudinal vibration can be written as [61]:

$$\mathrm{E_s A}\frac{\partial^2 \mathrm{u(x,t)}}{\partial \mathrm{x}^2} + N_{PZT}(x,t) = \rho \mathrm{A}\frac{\partial^2 \mathrm{u(x,t)}}{\partial \mathrm{t}^2} \tag{2.8}$$

where $\mathrm{E_s}$ is the Young's modulus of the beam, *A* is its cross sectional area, *u* is the longitudinal displacement (along *x*), N_{PZT} is the external distributed force, and ρ is the material density.

For the case of the transverse vibrations of the preloaded beam, the governing equation becomes [61]:

$$\mathrm{E_s I}\frac{\partial^4 \mathrm{w(x,t)}}{\partial \mathrm{x}^4} + \rho \mathrm{A}\frac{\partial^2 \mathrm{w(x,t)}}{\partial \mathrm{t}^2} - \mathrm{P}\frac{\partial^2 \mathrm{w(x,t)}}{\partial \mathrm{x}^2} = -\frac{\partial M_{PZT}(x)}{\partial \mathrm{x}} \tag{2.9}$$

where *w* is the transverse deflection (along *y*), *I* is the moment of inertia of the beam, M_{PZT} is the external distributed moment, *P* is the applied axial load and the other terms were defined previously.

In order to obtain the steady-state solution under harmonic excitation, separation of variables can be applied to Eqs. (2.8) and (2.9) above. Integrating the eigenfunction and the

hyperbolic external excitation, model expansion can be applied to determine orthonormal mode shapes and their participation coefficients. The deformation of the PZT patch can be computed as [4]:

$$u_{PZT}(x,t) = \mathrm{u}(x,t)|x_1 - \mathrm{u}(x,t)|x_2 - \left(\frac{h_s}{2}\right)[w'(x,t)|x_1 - w'(x,t)|x_2] \qquad (2.10)$$

where *u* is the longitudinal displacement (along *x*), *w* is the transverse deflection (along *y*), and $x_{1,2}$ are the positions of the two ends of the PZT patch.

To simplify the complex terms, the following property of the Heaviside function and Euler's formulae can be applied:

$$\int_{\mathrm{l_s}} \sinh\left[\Gamma\frac{2}{l_{PZT}}x\right]\sin\left[\frac{n\pi}{l_s}(x+d)\right][\mathrm{H}\left(\mathrm{x}+\frac{\mathrm{l}_{PZT}}{2}\right)-\mathrm{H}(\mathrm{x}-\frac{\mathrm{l}_{PZT}}{2})]\,d$$

$$= \mathrm{Im}\left\{\mathrm{e}^{\mathrm{i}\frac{\mathrm{n}\pi}{\mathrm{l_s}}\mathrm{d}}\int_{-\frac{\mathrm{l}_{PZT}}{2}}^{\frac{\mathrm{l}_{PZT}}{2}}\sinh\left[\Gamma\frac{2}{\mathrm{l}_{PZT}}\mathrm{x}\right]\mathrm{e}^{\mathrm{i}\frac{\mathrm{n}\pi}{\mathrm{l_s}}\mathrm{x}}\,\mathrm{dx}\right\}$$

Manipulating the terms in the right-hand side and using the properties of the hyperbolic functions ($\cosh(\mathrm{i}x) = \cos(x)$, $\sinh(\mathrm{i}x) = i\sin(x)$), these terms can be further simplified.

The effective point-wise structural dynamic stiffness of the beam can be finally computed as:

$$\mathrm{K}_{str} = \left(\frac{2}{\mathrm{l_s}}\mathrm{N}\sum_{n=0}^{\infty}\mathrm{X_n} + \frac{2\pi}{\mathrm{l_s^2}}(\mathrm{h_s}+\mathrm{h_{PZT}})\mathrm{N}\sum_{n=0}^{\infty}\frac{n\left[\cos\left[\frac{n\pi}{l_s}x_1\right]-\cos\left[\frac{n\pi}{l_s}x_2\right]\right]}{\mathrm{E_s I}\left(\frac{\mathrm{n}\pi}{\mathrm{l_s}}\right)^4 - \rho\mathrm{A}\omega^2 + \mathrm{P}\left(\frac{\mathrm{n}\pi}{\mathrm{l_s}}\right)^2}\mathrm{Y_n}\right)^{-1} \qquad (2.11)$$

where $X_n = \frac{-\sin\left[\frac{n\pi}{l_s}x_1\right]+\sin\left[\frac{n\pi}{l_s}x_2\right]}{E_s A\left(\frac{n\pi}{l_s}\right)^2-\rho A\omega^2}\frac{\cosh(\Gamma)\Gamma\frac{4}{l_{PZT}}\sin\left(\frac{n\pi}{l_s}\frac{l_{PZT}}{2}\right)-\frac{2n\pi}{l_s}\sinh(\Gamma)\cos\left(\frac{n\pi l_{PZT}}{l_s\ 2}\right)}{\left(\Gamma\frac{2}{l_{PZT}}\right)^2+\left(\frac{n\pi}{l_s}\right)^2}\sin\left(\frac{n\pi}{l_s}d+\frac{\pi}{2}\right)$,

$Y_n = \frac{\sin\left(\frac{n\pi}{l_s}d\right)}{l_{PZT}}\frac{\sinh(\Gamma)\Gamma^2\frac{8}{l_{PZT}}\cos\left(\frac{n\pi l_{PZT}}{l_s\ 2}\right)+\frac{4n\pi}{l_s}\cosh(\Gamma)\Gamma\sin\left(\frac{n\pi l_{PZT}}{l_s\ 2}\right)}{\left(\Gamma\frac{2}{l_{PZT}}\right)^2+\left(\frac{n\pi}{l_s}\right)^2}-\sinh[\Gamma]\left(\sin\left[\frac{n\pi}{l_s}x_1\right]+\right.$

$\left.\sin\left[\frac{n\pi}{l_s}x_2\right]\right)$, l_s is the length of the beam, d is the distance from left end of the beam to the middle point of the PZT patch, and the other terms were defined previously. The first summation term in Eq. (2.11) represents the contributions from the extensional vibrational modes, while the second summation term represents the contributions from the flexural vibrational modes. In the case of perfect bonding (no shear lag), Eq. (2.11) provides results equivalent to the solutions from ref. [4]. Two hundred terms in the summation were used for the results from this model shown in the paper.

In summary, a comprehensive model of EMI measurements on an axially preloaded beam can be obtained by using the structural stiffness of the preloaded beam from Eq. (2.11) into the EMI model of Eq. (2.1) and considering the effective electromechanical properties of Eq. (2.5). While this model can, in principle, relate PZT admittance to levels of axial stress, the determination of absolute stress levels requires the knowledge of all constants involved, and particularly the higher-order elastic, piezoelectric and dielectric properties of the PZT, which is a not a trivial requirement. Mechanical damping effects and dielectric dissipation can be also considered in the model by using complex moduli $\tilde{E}_s = E_s(1+\mu i)$ and $\tilde{Y}_a^E = Y_a^E(1+\mu i)$, and complex dielectric permittivity constant $\tilde{\varepsilon}_{33}^T = \varepsilon_{33}^T(1-\delta i)$, where μ is the mechanical

loss factor and δ is the dielectric loss factor, that are here assumed to be frequency-independent and only associated to first-order properties.

2.3. Experimental setup and procedure

Experiments were conducted on an aluminum bar and a steel bar to validate the analytical model and relate EMI signatures to applied axial loads. The steel beam was machined from the web section of an AREMA 136RE rail. The dimensions of the two bars (rectangular cross-sections) were 610 mm in length, 88.4 mm in width and 12.7 mm in thickness (aluminum) and 520 mm in length, 105.7 mm in width and 15.4 mm in thickness (steel). Densities were assumed as 2700 kg/m^3 for aluminum and 7850 kg/m^3 for steel. Young's moduli were assumed as 72.1 GPa (aluminum) and 213 GPa (steel). The Young's moduli of the specimens were determined from tensile tests. The densities were nominal values for aluminum and steel. The mechanical loss factors were assumed as 0.002 for both materials [40].

The axial load was applied by an MTS 110 tensile-compression machine (Fig. 2.4). The aluminum bar was stressed from 34.47 MPa (5 ksi) in tension to 34.47 MPa (5 ksi) in compression with a 6.89 MPa (1 ksi) step increment; the steel bar was stressed from 137.90 MPa (20 ksi) in tension to 137.90 MPa (20 ksi) in compression with a 34.47 MPa (5 ksi) step increment. This stress increment is consistent with a 10℃ temperature variation on a fully

constrained 136RE rail. The applied stress levels were designed to meet the following criteria: (a) stress levels less than one third of the yield strength to stay in the linear elastic range; (b) strain levels less than 600 microstrain to prevent mechanical depolarization of the PZT patches; (c) maximum compressive load less than half of the critical buckling loads to avoid global structural instability.

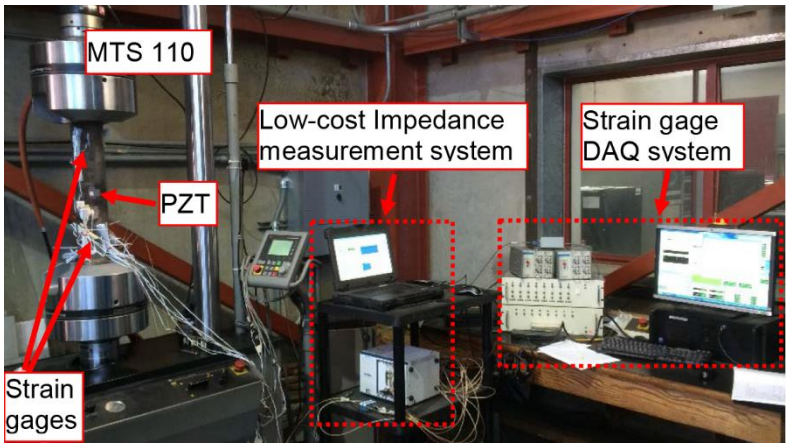

Figure 2.4 Experimental setup for the uniaxial load tests of the aluminum bar and the steel bar instrumented with the bonded PZT patch and the strain gages.

Each of the specimens was instrumented with a PZT patch (850 Navy II, APC International, Ltd.) (at the neutral axis at mid span. The PZTs were bonded with TML NP-50 adhesive, after hand grinding the specimen's surface and using acetone as a cleaner. A 10-lb weight was placed on the PZTs during curing to minimize the adhesive thickness. Electrical resistance strain gages were also installed for an independent measurement of axial stresses. At each load step, a specially designed low-cost impedance measurement system [62, 63]

recorded the PZT electrical admittance signatures. The applied electric field onto the PZT patch is along direction 3 as shown in Fig. 2.1. Two frequency bands were investigated: a "low frequency" band of 10 kHz-800 kHz, and a "high frequency" band of 1 MHz-10 MHz. The in-plane vibrational modes of the specimen were expected to dominate in the lower frequency range, while the PZT thickness vibrational modes and electrical resonance were expected to reside in the higher frequency band.

2.4. Results of model and experiments

Results from the model and experiments were obtained in terms of conductance spectra (real part of the admittance) and susceptance spectra (imaginary part of the admittance) from both the aluminum and the steel bars. The properties of the PZT, adhesive and specimens used in the model are listed in Table 2.1.

2.4.1 Conductance results

The conductance spectra obtained from the experiments and from the analytical model for the aluminum bar and the steel bar at various axial stress levels are shown in Fig. 2.5. Based on the findings of Ref. [41], indicating that stress-induced conductance resonance shifts associated to flexural vibrational modes are independent of the excitation frequency, one representative resonance for each structure was chosen for this portion of the study, namely ~160 kHz for the aluminum specimen and ~200 kHz for the steel specimen. Both experiments

and model indicate that the resonance peak shifts towards lower frequencies as the applied stress varies from tension to compression, which is an expected result from structural dynamics of prestressed beams. The differences of less than 5 kHz that are seen in the values of the resonant frequencies between the experiments and the model can be due to a variety of reasons, including mismatches of material properties and of boundary conditions (for example, the simply supported assumption in the model versus the experimental clamped-clamped condition). A further comparative result is shown in Fig. 2.6, that plots the resonance shifts from Fig. 2.5 relative to the zero stress levels. For both specimens, the results show that these resonance shifts are proportional to the applied uniaxial stress levels, and are consistent between experiment and the model. The sensitivity of the PZT conductance peak frequency shifts to the applied stress was further analyzed through linear regression models based on 50 experimental measurements as dashed lines shown in Fig. 2.6. Considering the zero-stress resonance peak as the reference, the regression analysis indicated a frequency shift sensitivity of 11Hz/ksi at the ~160 kHz resonance for the aluminum bar, and of 2.6 Hz/ksi at the ~ 200 kHz resonance for the steel bar. These sensitivities would lead to measurable shifts in conductance peaks for critical stress values associated, for example, to buckling of rails in warm weather (compressive stresses) and pull-out breakage of rails in cold weather (tensile stresses).

Table 2.1 Properties of PZT [64], adhesive and specimens used in the model results.

	Property	Value	Unit		Property	Value	Unit
PZT-5A	l_{PZT}	12.7	mm	**Al Bar**	l_s	610	mm
	b_{PZT}	12.7	mm		b_s	88.4	mm
	h_{PZT}	0.635	mm		h_s	12.7	mm
	Y^E_{PZT}	59	GPa		μ	0.002	
	ρ_{PZT}	7700	kg/m^3		E	72.1	GPa
	d_{31}	-1.68E-08	m/V		ρ	2700	kg/m^3
	ε_{33}^T	1.59E-08	F/m	**Steel Bar**	l_s	520	mm
	μ	0.005			b_s	105.7	mm
	δ	0.02			h_s	15.4	mm
	$\partial\varepsilon_{33}^T / \partial\bar{T}_1$	97.4	$pF \cdot m^{-1}/ksi$		μ	0.002	
Adhesive	G_b	3.2	GPa		E	213	GPa
	h_b	0.01	mm		ρ	7850	kg/m^3

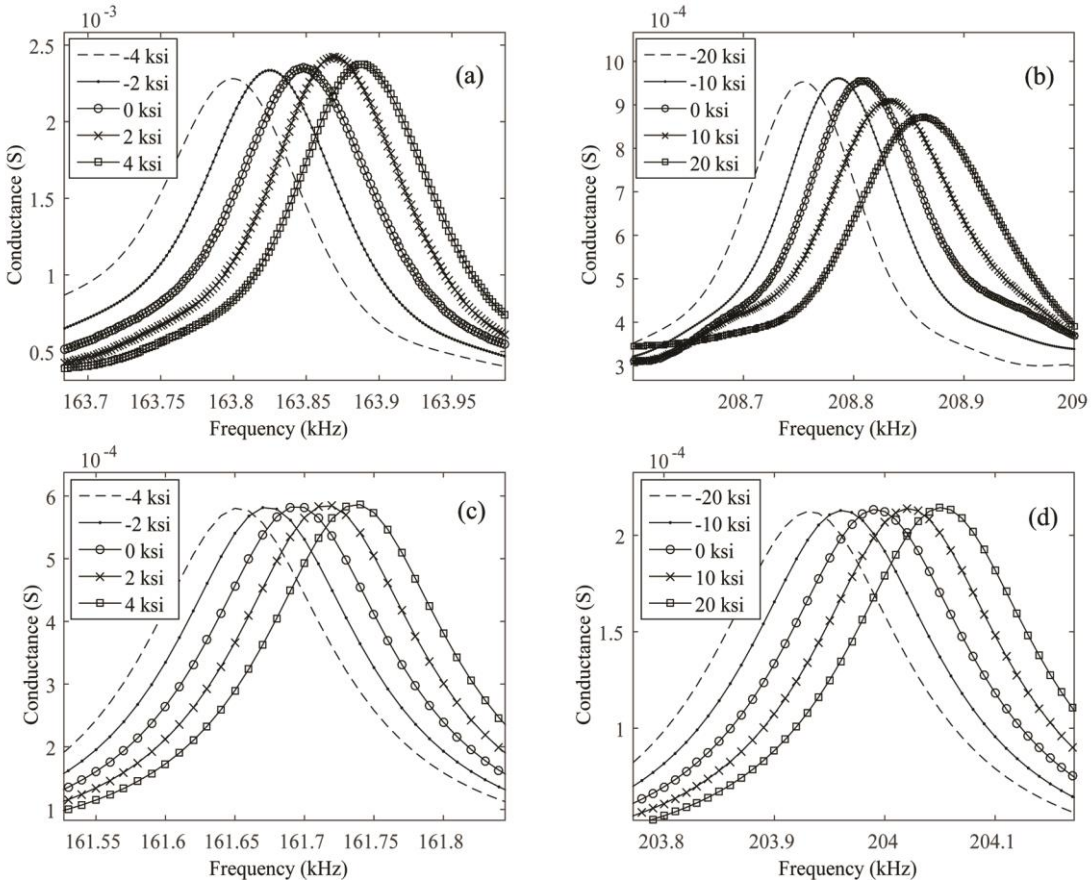

Figure 2.5 Shifts in conductance resonance peak for varying axial stress levels from (a) the aluminum bar experiment, (b) the steel bar experiment, (c) the aluminum bar model, and (d) the steel bar model.

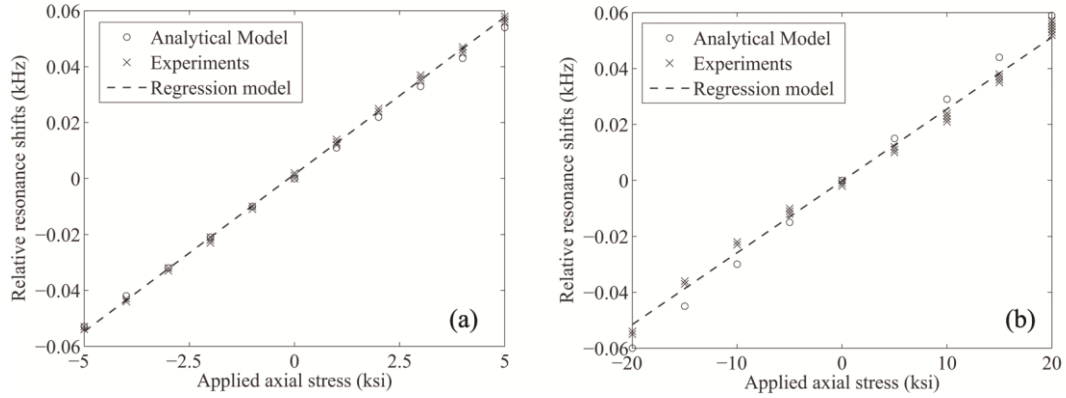

Figure 2.6 The relative shift in resonance peak from Fig. 5 vs. stress levels from the analytical model and the experimental tests of (a) the aluminum bar and (b) the steel bar.

2.4.2 Susceptance results

The results of the susceptance metric from these tests are shown in Fig. 2.7 (experiment) and Fig. 2.8 (model) for the two specimens. The low frequency band of 50 kHz – 150 kHz was selected in these figures because it resides before the first PZT resonance to provide accurate estimation of the PZT capacitance, directly related to susceptance. The slope of the susceptance spectra against angular frequency directly corresponds to the PZT capacitance, which, in turns, depends on the effective piezoelectric and dielectric constants, and therefore the applied stress, in the manner described in Section 2.2. The experimental results of Fig.2.7 (a) and (b) show a decrease in the susceptance slope as the applied stress varies from tension to compression, for both specimens. Close-up views of selected resonances are shown in Fig. 2.7(c) and (d). Qualitatively similar trends of the susceptance slopes are seen in the model results of Fig. 8. Again, differences in the susceptance resonance peaks between the experiments and the model can be caused by mismatch in material properties and in boundary conditions.

Fig. 2.9 shows a further comparative study in terms of capacitance in the 50 kHz - 100 kHz band. The plots in Fig. 2.9 confirm an approximately linear increase of PZT capacitance with increasing applied stress with stress sensitivities consistent between experiment and model. The linear regression analysis based on 50 experimental measurements, shown by the dashed lines in Fig. 2.9(a) and (b), indicates a capacitance sensitivity of 15.43 pF/ksi for the

aluminum bar and of 6.63 pF/ksi for the steel bar. Again, these results suggest that a capacitance slope measurement could also be used to estimate for example, critical axial stress levels in rails associated with buckling or breakage failures.

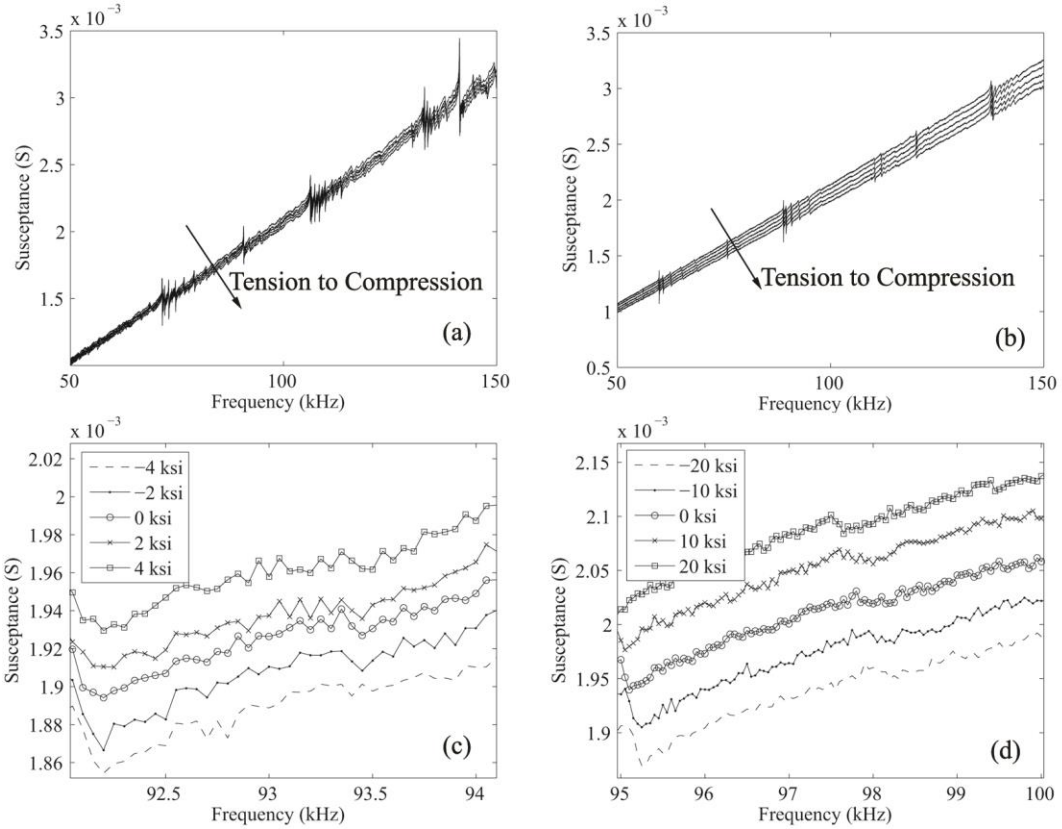

Figure 2.7 The susceptance signatures for varying axial stress levels from the experimental tests of (a) the aluminum bar, (b) the steel bar, (c) the aluminum bar with zoomed-in frequency band, and (d) the steel bar with zoomed-in frequency band.

2.4.3 Use of the PZT electrical resonances

Given the results from Section 2.4.2, in an effort to further investigate the stress-dependence of the capacitance of the bonded PZT patch, the electrical resonances of the measurement circuit and the PZT patch were investigated.

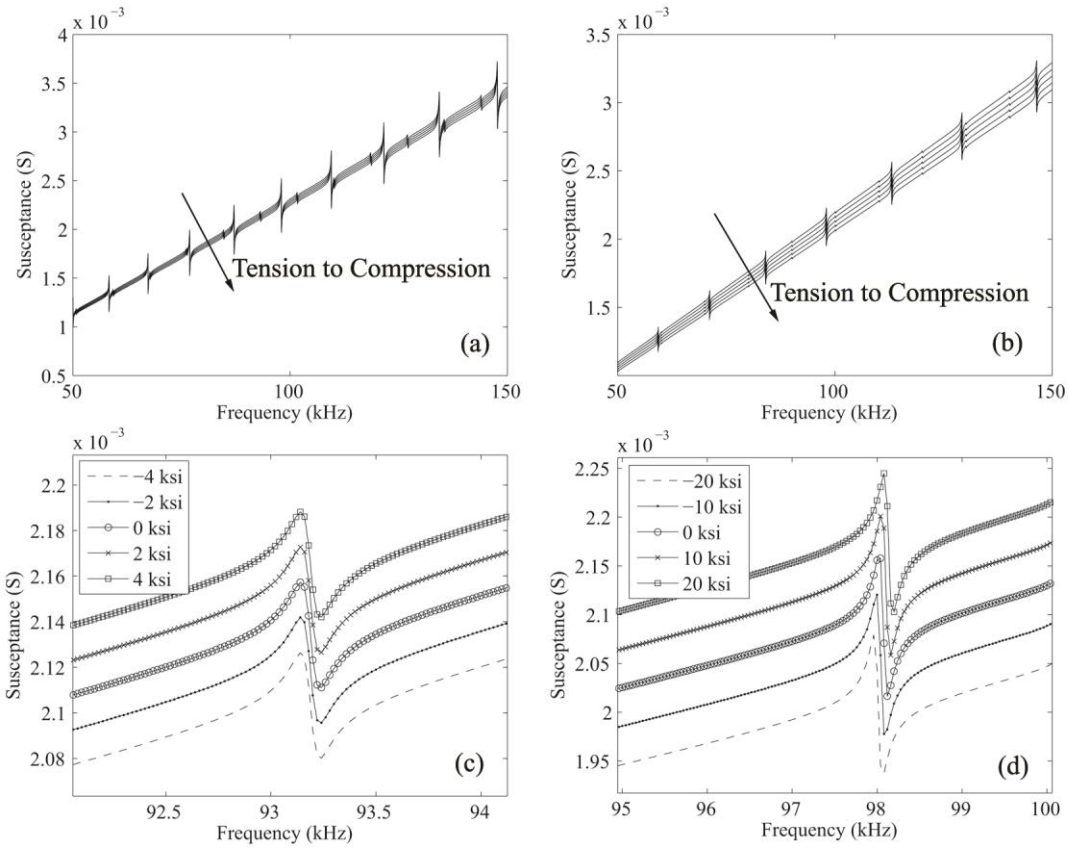

Figure 2.8 The susceptance signatures for varying axial stress levels from the analytical model of (a) the aluminum bar, (b) the steel bar, (c) the aluminum bar with zoomed-in frequency band, and (d) the steel bar with zoomed-in frequency band.

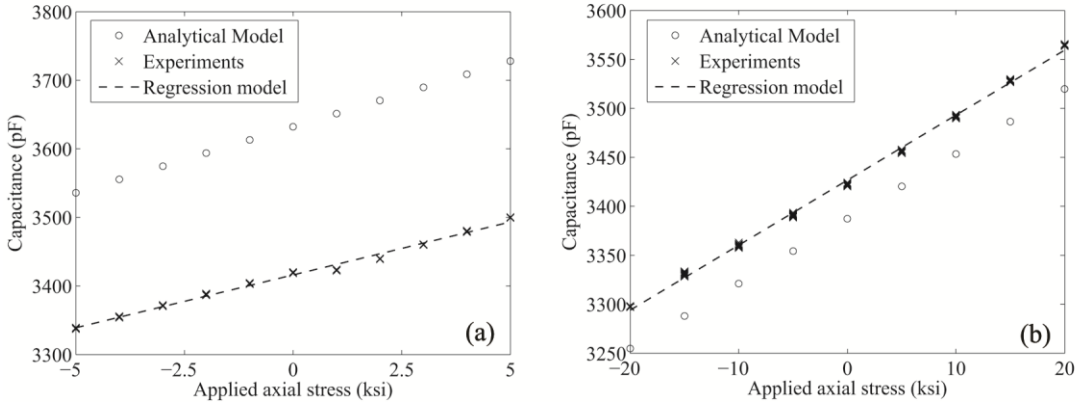

Figure 2.9 The capacitance changes vs stress levels from the analytical model and the experimental results of (a) the aluminum bar and (b) the steel bar.

The equivalent circuit of the EMI measurement setup is shown in Fig. 2.10: the resistance R_1 of 100 Ω was used as potential divider to measure the current with the leadwires of the inductance L_1 of 0.857 μH; the PZT patch was idealized as a capacitance with the inductance L_2 of 0.372 μH from the lead wires. The electrical resonance of this equivalent circuit can be estimated by computing the frequency corresponding to zero complex impedance:

$$freq_{res} = \left(2\pi \sqrt{\frac{L_1 L_2 C_1}{(L_1 + L_2)}} \right)^{-1} \tag{2.12}$$

where C_1 is the capacitance of the PZT patch, and L_1 and L_2 are the parasitic inductance of the lead wires. By substituting the appropriate values, Eq. (2.12) yields an electrical resonance value of 5.3 MHz. The conductance signatures of the 1 MHz-10 MHz frequency band contain both the thickness mode and the electrical resonance of the bonded PZT element, as shown from the experimental result of Fig. 2.11 for the instrumented steel bar. The experimental electrical resonance is found at 5.1 MHz, where the difference from the estimated 5.3 MHz value can be attributed to ignoring the capacitances of the coaxial cables connecting PZT to the DAQ system in the model.

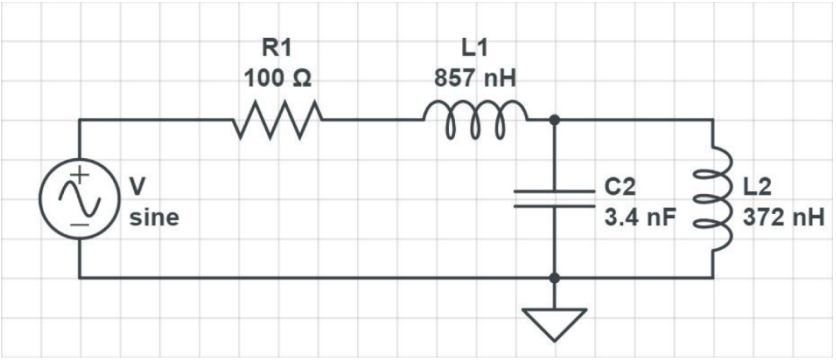

Figure 2.10 The equivalent circuit for the data acquisition system and the PZT element (values measured by impedance analyzer).

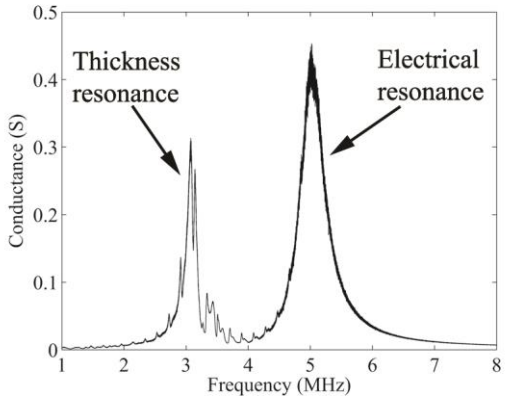

Figure 2.11 Experimental conductance spectrum above 1MHz with thickness mode and electrical resonance of the PZT patch bonded to the steel bar at zero applied stress.

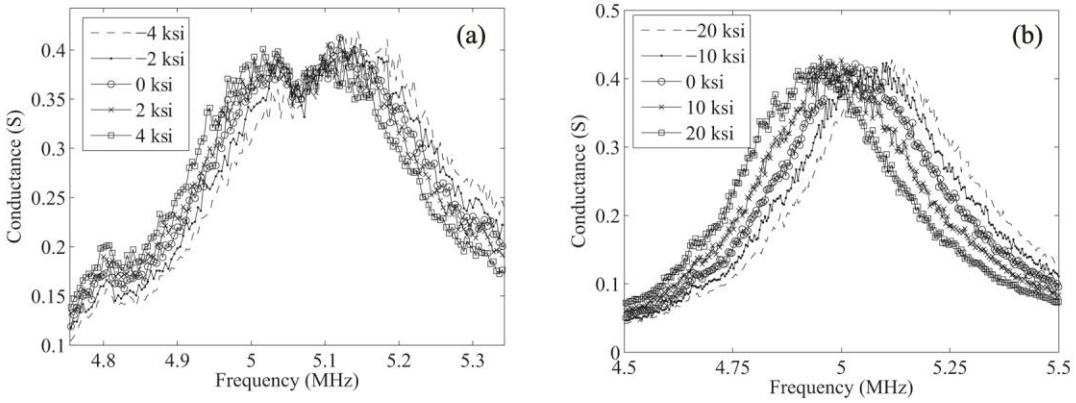

Figure 2.12 Experimental conductance spectra for varying axial stress levels from (a) the aluminum bar and (b) the steel bar.

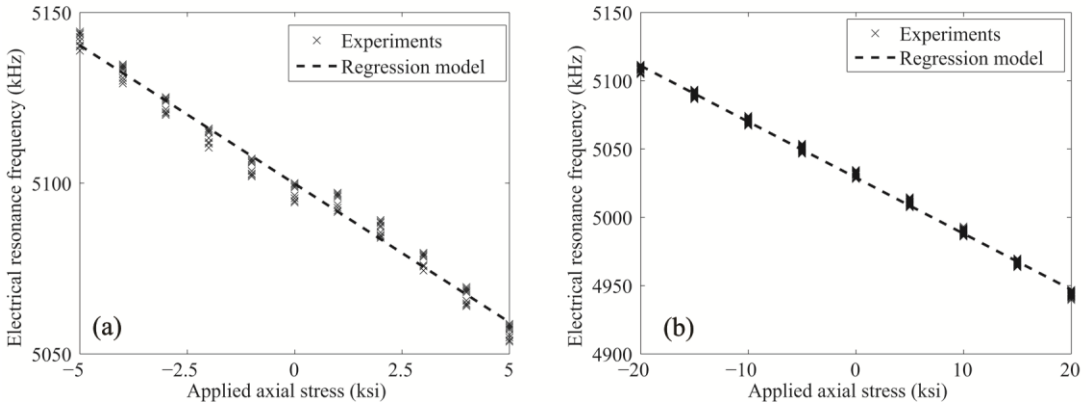

Figure 2.13 Experimental shift of the electric resonance peak from Fig. 12 for varying stress levels based on 50 experimental measurements.

Assuming that the electrical components (resistance and parasitic inductances) do not change during the measurement period, the frequency shifts of the electrical resonance are caused by the varying capacitance, which is a function of the effective piezoelectric and dielectric constants of the bonded PZT patch, and therefore the load applied to the host structure. The previous results of Fig. 2.9 clearly show that the PZT capacitance increases with increasing stress level, which would result – according to Eq. (2.12) – into a decrease in electrical resonance frequency peak. This behavior is confirmed by the results of Fig. 2.12, that plot the experimental electrical resonance peaks as a function of uniaxial stress applied to the aluminum bar and the steel bar. The linear regression analysis, shown in Fig. 2.13, indicates a downward shift of the resonance peak with increasing stress level, with frequency sensitivity of - 8.1 kHz/ksi (corresponding to a capacitance sensitivity of 11.94 pF/ksi) for the aluminum bar, and of -4.1 kHz/ksi (corresponding to a capacitance sensitivity of 6.3 pF/ksi) for the steel

bar. These values of capacitance sensitivities to stress are slightly different from the values obtained in Section 2.4.2 in a different frequency band, likely due to the frequency dependence of the dielectric permittivity. In general, these results show that tracking the electric resonance of the PZT may provide a suitable means to estimate the applied stress, once the appropriate sensitivities are applied to the given frequency band.

2.5. Discussion and conclusions

In this chapter, an investigation was conducted to explore the applicability of the EMI method to estimate the *in-situ* uniaxial stresses in structures. This study is one part of a broader research effort to develop techniques for identifying critical axial load levels in rails associated with buckling (compression) failures or breakage (tension) failures.

An analytical model was first developed to explicitly account for an applied prestress in the EMI admittance signature of the PZT element bonded to the structure. This model incorporates shear-lag behavior for the PZT-structure strain transfer, nonlinear piezoelectric constitutive relations through effective dielectric and piezoelectric constants to account for the prestress in the PZT element, and the point-wise dynamic stiffness of the prestressed host structure subjected to the PZT spatially hyperbolic excitation. This model was not existent before. Theoretically, the model would allow to relate the admittance signatures to absolute levels of applied (axial) stress. However, such absolute stress determination would require

knowledge of all of the constants involved, including the higher-order elastic, piezoelectric and dielectric properties of the PZT element, which is not a trivial requirement. For this reason, as in the majority of measurement techniques, determining changes in stress levels, rather than absolute levels, remains a much easier task.

Experiments were conducted on an aluminum bar and a steel bar instrumented with PZT elements and subjected to tension and compression axial loads. For the EMI conductance spectra, peaks mainly associated to structural resonances were found to linearly shift towards lower frequencies when subjected to decreasing loads from tension to compression. The model is capable to capture the experimental trend, with minor differences likely associated to mismatched boundary conditions for the bars and/or assumed properties for bars, PZT and adhesive materials. The stress sensitivity of the conductance resonance shifts was found at 11 Hz/ksi for the aluminum bar at the ~160 kHz resonance and at 2.6 Hz/ksi for the steel bar at the ~205 kHz resonance. These sensitivities which are significant enough to be captured by a low-cost EMI measurement circuit.

In terms of the EMI susceptance spectra, whose slope corresponds to the capacitance of the bonded PZT element, the slopes were also found to vary linearly with the applied uniaxial load, and decreasing with decreasing loads going from tension to compression. The sensitivities of the capacitance were found to be 15 pF/ksi for the aluminum bar and 6.6 pF/ksi for the steel bar in the 50-100 kHz range, and were consistent between the model and the

experiment. These sensitivities are significant enough to be measured by LCR meters or impedance analyzers, whose capacitance measurement precision is typically 1e-3 pF. In cases when the frequency resolution of the EMI measurement is limited, the capacitance measurement (slope of susceptance) can therefore provide a good option for stress estimation. In general, the resonance frequencies will depend on the particular PZT-structure assembly under test, so that it is difficult to predict specific values without performing, for example, an initial frequency sweep.

Additional observations for the two specimens were made at the much higher electrical resonance of the EMI circuit, which was found at ~ 5 MHz. This resonance was never explored for stress measurement in prior EMI studies. The experiments indicated electrical resonance shifts of -8.1 kHz/ksi for the aluminum bar and -4.1 kHz for the steel bar. These sensitivities are orders of magnitude larger than those observed at the lower frequencies of structural resonances, and could therefore provide an enhanced tool for prestress estimation. In order to eliminate the limitation on the DAQ hardware (clock, power consumption and stability), the electrical resonance frequency could be shifted to a lower frequency band by adding capacitance components without changing the stress sensitivity of the EMI measurement.

The dependence on frequency of the mechanical and electrical loss factor for the PZT [65, 66] could be added to the model to improve its accuracy. Another issue that was not

addressed in the present study is the effect of hysteresis potentially occurring under cyclic loading [47, 48, 67]. This behavior, which may affect the reversibility of the admittance signatures, should be considered in future studies on this topic.

Specific ranges of operational parameters (stresses, electric field, temperature) within which the nonlinear piezoelectric equations can be considered valid are difficult to indicate. The formulation proposed here assumes that a nonlinearity arises from the application of a stress, akin to, for example, the acoustoelastic theory of wave speed dependence on applied stress. Finding these ranges of validity, including temperature effects on the nonlinear constants, could be the subject of future studies. Clearly, this chapter did not consider the effects of varying temperature on the estimation of axial loads by the EMI signatures. The temperature effect will be covered in the following Chapter 3.

2.6 Acknowledgements

This chapter, in part, has been accepted for publication by Experimental Mechanics, Zhu, Xuan; Lanza di Scalea Francesco. The title of this paper is **Sensitivity to Axial Stress of Electro-Mechanical Impedance Measurements**. The dissertation author was the primary investigator and primary author of this paper.

3. Thermal Stress Characterization Using the Electro-Mechanical Impedance Method and its Application to Continuous Welded Rails

3.1 Introduction: environmental and operational variability on SHM systems

Environmental and operational variability has traditionally been among the main obstacles for the implementation of structural health monitoring systems [68]. There include changes in boundary conditions, temperature, and humidity. Changes due to these factors often mask more subtle structural changes that are the targets of the SHM systems [69]. Various strategies for data normalization have been proposed by previous studies to separate the signal changes caused by operational and environmental variations from the ones caused by the structural changes of the interest, such as structural deterioration or degradation [68-75].

When direct measurements of the environmental or operational parameters are available, various kinds of regression and interpolation analysis can be performed to relate the measurements relevant to structural damage and those associated with environmental and operation variation of the system [69- 71].

Sohn [69] proposed a multivariate linear model to accommodate the changes due to temperature variations for the damage detection system on the Alamosa Canyon Bridge in New Mexico. This allowed the system to discriminate the changes of modal parameters (natural frequencies) due to temperature changes from those caused by structural damages.

Peeters [70, 71] fitted the data from the healthy bridge structures into ARX models, which were used to simulate the dynamic eigenfrequencies. Structural damage was identified when the eigenfrequency of the new measurement lies outside of the estimated confidence intervals.

When measurements of the environmental parameters are not available, it is recommended to model the underlying relationship between the environmental variables and the SHM features [68]. Manson [74] performed a Principle Component Analysis (PCA) on the training data from varying temperature conditions. Assuming the variance in the data was primarily produced by temperature variation, the features were projected onto a reduced feature space with only the minor principal components. Oh et al. [75] used the AR-ARX model to extract the damage-sensitive features and applied the kernel PCA to characterize the hidden relationship between unmeasured environmental parameters and the features. A hypothesis test was performed on the extracted features to evaluate the damage state of the structure.

Prior studies on the EMI-based SHM systems demonstrated the effective damage detection frameworks under varying environmental and operational conditions. Hong et al [76] found a linear relationship between the correlation coefficients of the impedance signatures (with respect to baseline measurement) and the temperature, such that the damage can be detected using the control chart analysis. Sepehry et al. [77] introduced artificial neural networks using radial basis function for temperature compensation of the impedance-based

SHM. The features of frequency ranges, mean of real part of the impedance, and temperature were considered. Lim et al. [78] developed the data normalization technique for EMI-based damage detection, using the Kernel PCA to minimize the false-alarms due to variations of surrounding environments. The training impedance signatures were collected from various loading and temperature conditions with the intact structure. The features of the Root Mean Square (RMS), the x coordinate centroid, maximum and minimum response values, and the coefficients of a polynomial function fitted to the signatures were considered in their study. By projecting the training and test data onto the principal axes, the distances between the projection of the test data and the ones of the optimal baseline were used as damage indexes and fed into a statistical outlier analysis for defect detection.

In this chapter, the temperature influences on the EMI measurements is investigated by analytical and experimental studies. The effectiveness of the potential features across the admittance spectrum was experimentally demonstrated. Based on the feature analysis, two temperature compensation strategies are proposed to eliminate the temperature influences on the EMI estimation of the axial stress levels in the CWR structure.

3.2 Temperature effects on EMI measurements

It is well established that the raw EMI signatures are sensitive to temperature fluctuations. For example, the changing temperatures will result in significant variations in

resonance frequencies and magnitudes, even if there is no actual damage to the structure, thereby leading to false alarm [79-82]. Temperature compensation strategies based on cross correlation and the minimum summation of squared errors were proposed to identify the resonance shifts led from temperature variations, and extract the damage indexes from the 'corrected' resonances in order to lower the false alarm rate [81,83]. However, the study in section 3.4.1 shows that the aforementioned strategies will not be effective in the scenarios where there is minor change of the structural stiffness associated to thermal stress (compared to local structural damage. In this chapter, the temperature effects on the EMI admittance signatures were investigated in the analytical model proposed in Chapter 2, and by experimental studies. The model accounts for all relevant temperature-dependent parameters of a PZT-structure system on an Euler beam, including the PZT-structural interaction, and the piezoelectric and dielectric permittivity properties of the transducer itself. For each of the features, the temperature sensitivity was compared with the stress sensitivity. By exploring multiple features in addition to the conventional structural resonances, the EMI measurements seem to be able to isolate the effects of stresses under temperature variations.

In order to investigate the effects of the changing temperature, a linear dependence of each temperature-dependent property was assumed as: $X(T) = X(T_0) + \frac{\partial X(T)}{\partial T}\Delta T$, where T is the current temperature, T_0 is the ambient temperature (assumed 20℃), and $\frac{\partial X(T)}{\partial T}$ is the sensitivity of the property to temperature [45]. The piezoelectric coefficient was modeled

assuming the sensitivity of $\partial d_{31}/\partial T = -0.5 \times 10^{-12}\ m/V$ ℃ [84]. The dielectric permittivity term was considered to with sensitivity of $\partial \varepsilon_{33}^{T}/\partial T = 0.14 \times 10^{-9}\ F/m$ ℃. Patch length and thickness changes were modeled assuming a thermal expansion coefficient for PZT 5A of $3 \times 10^{-6}\ m/m$ ℃. For the substructure properties, the temperature sensitivities of $\partial E_s\ /\partial T = -0.04\ GPa/$ ℃, and the nominal coefficient of thermal expansion for steel of $1.152 \times 10^{-5}\ m/m$ ℃ was assumed, with temperature sensitivity of $\partial G_b\ /\partial T = -0.013\ GPa/$ ℃ for the bonding layer. The temperature influences were studied on a PZT ceramic patch bonded on a rectangular steel bar. Mechanical damping effects and dielectric dissipation were assumed to be temperature-independent in the model by using complex moduli $\tilde{E}_s = \mathrm{E_s}(1 + \mu i)$ and $\tilde{Y}_a^{E} = \mathrm{Y_a^E}(1 + \mu i)$, and complex dielectric permittivity constant $\tilde{\varepsilon}_{33}^{T} = \varepsilon_{33}^{T}(1 - \delta i)$, where μ is the mechanical loss factor and δ is the dielectric loss factor, here assumed to be frequency-independent and only associated to first-order properties.

3.3 Experimental setup

Two sets of experiments were conducted for analytical model validation and thermal stress characterization: the environmental chamber (EC) test and the CWR test. The EC test was conducted to validate the analytical model involving the varying temperatures with a rectangular steel bar machined from the web section of an AREMA 136RE rail. The specimen was instrumented with PZT patch at the middle point and placed in a free-free boundary

condition. While the specimen experienced step-size temperature increments, the low-cost impedance measurement system recorded multiple admittance signatures. The experimental setup is shown in Fig. 3.1 (a). The chamber temperature raised from 20 ˚C to 90 ˚C with approximately 2.5 ˚C increments. At each step, the chamber temperature was hold at the target temperature within ± 0.5℃. This range was chosen to include temperatures potentially seen in rail tracks in the field under common warm weather conditions. Since the steel bar was free to expand, the influence on the changes to the admittance signatures were expected to only result from temperature effects on the test specimen, bonding layer and PZT itself (no thermal stress).

The CWR test was conducted at UCSD's Large-Scale Rail NT Test-bed shown in Fig. 3.1 (b). This facility is a unique 70-ft long CWR track, that allows to impose thermal loads in a highly controlled laboratory environment. The tracks (a 136RE rail and a 141RE rail) can be pre-stressed at varying rail installation stresses. The existing track was installed with about 60 ℃ as the zero stress state value. Customized rail switch heater wires were implemented to heat up the rail tracks. The test-bed is instrumented with eight full-bridge temperature-compensated strain gage locations (four on each rail) and eight temperature sensing locations (four on each rail). The Wheatstone bridge strain gages were zeroed during the rail installation under zero stress state, and can provide the measurement of the true thermal stress in the rail. The large-scale test-bed was designed and constructed with the financial support of the FRA and in-kind

support of the Burlington Northern Santa Fe (BNSF) railway. *Instrumentation Services* of Pueblo, CO provided the strain gage and temperature instrumentation and measurements according to railroad standards.

To implement the impedance-based SHM system, the square PZT patch was bonded at the neutral axis of the 136RE rail and the temperature measurements were recorded by the thermocouple closest to the PZT element. The test procedure included by temperature increments of 20 ˚C to 90 ˚C with approximately 2.5 ˚C increments. At each step, a feedback temperature control system kept the rail temperature at the targets approximately to within ± 1℃. Starting from the initial tensile stress state at ambient temperature, the stress level decreases to zero stress state at Neutral Temperature, and then moved to the compressive load range.

For both tests, two frequency bands were investigated for the EMI measurement, namely 10 kHz-800 kHz and 1 MHz-10 MHz. The in-plane vibration modes dominate in the lower frequency range, while the later frequency band covers the thickness vibration modes and electric resonances.

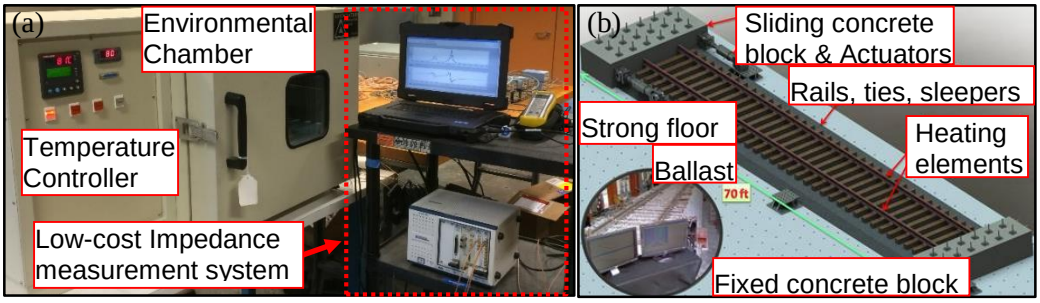

Figure 3.1 Experimental setups for (a) the environmental chamber test (temperature only), and (b) the Continuous Welded Rail test (thermal stress)

3.4 Model and experimental results

To illustrate the temperature influences on the EMI measurements, the conductance and the sucseptance were investigated with modeling and experimental results. Based on the findings on the sucseptance, a strategy to magnify the index sensitivity was proposed and validated with experimental results.

3.4.1 Conductance analysis

The analysis of the conductance at varying temperatures of selected resonance peak is shown in Fig. 3.2. In Fig. 3.2 (a) and (c), the experimental results indicate that the selected resonances of the conductance shift towards lower frequency as the temperature raised from 20℃ to 60℃, which is mainly due to the softening of structure, PZT patch and the bonding layer. In Fig. 3.2 (b) and (d), similar behaviors were observed from the analytical model, where the differences of the resonance frequencies are potentially caused by the mismatch in boundary conditions. In both the experimental and analytical results, the resonance shifts were observed to be proportional to temperature. A further comparative study, based on the relative frequency shift of the selected resonances, confirmed this conclusion as shown in Fig. 3.2(e). In this investigation, the reference signature was selected as the signature corresponding to the measurement at ambient temperature (20℃). With the selected resonances, the relative resonance frequency shifts with respect to the ambient temperature were computed and plotted against the varying temperatures. The experimental and analytical results show excellent

agreements on the monotonic trend. The difference in the slopes can result from the uncertainties of the temperature-sensitive Young's modulus of the PZT ceramic and the steel substructure.

The analytical model provides satisfactory predictions of the structural resonance behaviors under temperature variation. Furthermore, linear regression models were used to quantify the temperature sensitivity of the relative frequency shifts from the selected resonance based on experimental measurements: a frequency shift rate of 160 Hz/10℃ at resonance of 134 kHz and 220 Hz/10℃ at 184 kHz were observed in response to the varying temperature, while the frequency shift rate of 2.6 Hz/ksi at 207kHz was observed in response to the applied uniaxial stress in section 2.4.1. Based on the strain readings from the CWR136RE rail, a temperature increment of 10℃ would approximately induce thermal stress at a level of -19.6 MPa (-2.84 ksi). The result shows that the feature based on structural resonance shifts in the conductance spectrum is sensitive to uniaxial stress. However, the temperature effect would dominate the variations of this feature.

3.4.2 Susceptance analysis

The analysis on the EMI susceptance under varying temperatures of selected frequency band is shown in Fig. 3.3. In Fig. 3.3 (a), the experimental results indicate the slope of the susceptance increasing as the raising temperatures. The same behavior were observed in the model results as shown in Fig. 3.3(b): the slopes of the susceptance signatures demonstrate

a positive correlation with increasing temperature. The slope of the susceptance against angular frequency corresponds to the capacitance of the piezoelectric element, which strongly depends on the effective piezoelectric and dielectric constants in the manner as described in section 2.4.2. A further comparative study based on the capacitances (in pF) from the susceptances between 50 kHz and 150 kHz confirmed this conclusion as shown in Fig. 3.3 (e). With the selected frequency ranges, the capacitances increase approximately linearly with respect to the varying temperatures. The experimental and analytical results have an excellent agreement in terms of the monotonic trend and sensitivities. The slight differences on absolute values and stress-sensitivities of the capacitances between the experiments and models are expected, mainly resulted from the measurement circuit components, along with the uncertainties of the effective material properties and the shear stress transfer from the bonding layer.

The analytical model provides satisfactory predictions on the behavior of the susceptance under temperature influences. Furthermore, linear regression models were used to quantify the temperature sensitivities of the capacitances based on experiments: a capacitance change rate of 157 pF/10℃ was observed in response to the varying temperatures, while a rate of 6.63 pF/ksi was observed in response to the applied uniaxial stress as shown in section 2.4.2. Considering the dominant temperature influence, the ratio between the stress and

temperature sensitivities has been improved compared to that based on the structural resonance shift.

3.4.3 Use of electrical resonances

Given the results from section 3.4.2, the temperature influence on the electrical resonances of the measurement circuit and the PZT patch was investigated. The equivalent circuit was shown in Fig. 2.10 in section 2.4.3. Again, the electrical resonance of the equivalent circuit in Fig. 2.10 can be estimated by computing its electric impedance and searching for the frequency corresponding to zero complex impedance, as in Eq. (2.12). Assuming the electrical components (resistance and parasitic inductances) do not change during the measurement period, the peak frequency shift of the electrical resonance are induced by the varying capacitance, which is a function of the effective piezoelectric and dielectric constants of the bonded PZT patch. Revisiting the previous results in Fig. 3.3 (e), when the structure was subjected to varying temperature as in the EC test, the capacitance of the PZT patch increased, such that a decrease of the resonance frequency was predicted according to Eq. (2.12).

The electrical resonances at various temperatures are shown in Fig. 3.4 (a). The experimental results indicate the electrical resonances shift towards lower frequency with raising temperature, which is expected form Fig. 3.3(e) and Eq. (2.12). Furthermore, to quantify the electric resonance shift, a cross-correlation method was applied to determine the

frequency peaks and the linear regression models were proposed to compute the temperature sensitivities of the shifts of the electric resonances: a capacitance change rate of 73.5 kHz/10℃ was observed in response to the varying temperatures, while a resonance shift rate of 4.1 kHz/ksi was observed in response to the applied uniaxial stress in section 2.4.3. The ratio between the stress and temperature sensitivities has been further improved compared to that based on capacitance.

3.5 The in-plane and out-of-plane PZT resonances

Before moving to the thermal stress analysis, two additional potential features for thermal stress characterization were investigated, namely the PZT resonances below 1 MHz and the thickness modes above 1 MHz, corresponding to the in-plane and the out-of-plane vibration modes of the PZT patch [85,86], respectively. Under the uniaxial loading test, the stress sensitivity of the piezoelectric constants (d_{31}) parameters were assumed to be 8.46e-12 $V \cdot m^{-1}/ksi$ for PZT-5A. The dielectric permittivity term was considered to be linear with sensitivity of $\partial \varepsilon_{33}^{T}/\partial \bar{T}_1 = 97.4\, pF \cdot m^{-1}/ksi$ [48]. Under varying temperatures, the temperature sensitivity of the piezoelectric constants (d_{31} and d_{33}) were assumed to be $\partial d_{31}/\partial T = -0.5 \times 10^{-12}\, m/V$ ℃ and $\partial d_{33}/\partial T = -0.8 \times 10^{-12}\, m/V$ ℃ , respectively [84]. The dielectric permittivity term was considered to be linear with sensitivity of

$\partial \varepsilon_{33}^{T}/\partial T = 0.14 \times 10^{-9}\ F/m$ ℃. The temperature sensitivity of $\partial G_b\ /\partial T = -0.013\ GPa/$ ℃ was used for the bonding layer.

As the properties of the PZT patch changed due to applied uniaxial loads and temperatures, the in-plane and out-of-plane vibration modes would be affected, as shown in Fig. 3.5 and 3.6. Under the varying applied uniaxial load levels (the MTS test in Chapter 2), as shown in Fig. 3.5 (a) and (c), the magnitudes of in-plane resonances in the conductance spectra decreased as the applied load went from compression to tension, which matches the prediction that the increasing d_{31} would lead to decreasing resonance magnitudes. Under the varying temperature (EC test), as shown in Fig. 3.5 (b) and (d), the magnitudes of in-plane resonances in the conductance spectra increased with the raising temperature, while the softening of the bonding layer and the PZT patch result in the resonance shifting towards lower frequency.

For the thickness mode, the EM signatures under the varying applied uniaxial load levels (MTS test) are shown in Fig. 3.6 (a), where both the magnitude variation and horizontal shifts were observed. A similar behavior was also observed under the varying temperature (EC test), as shown in Fig. 3.6 (b).

To quantify the temperature/stress influence on the EM signatures, the features including similarity, the Root Mean Square Deviation (RMSD), and the Root Mean Square (RMS) were extracted from selected resonance modes in the conductance spectrum for further analysis. The similarity is the normalized cross-correlation coefficient with respect to the

reference signatures. The index of RMSD [5], as a measure of the residual difference from a

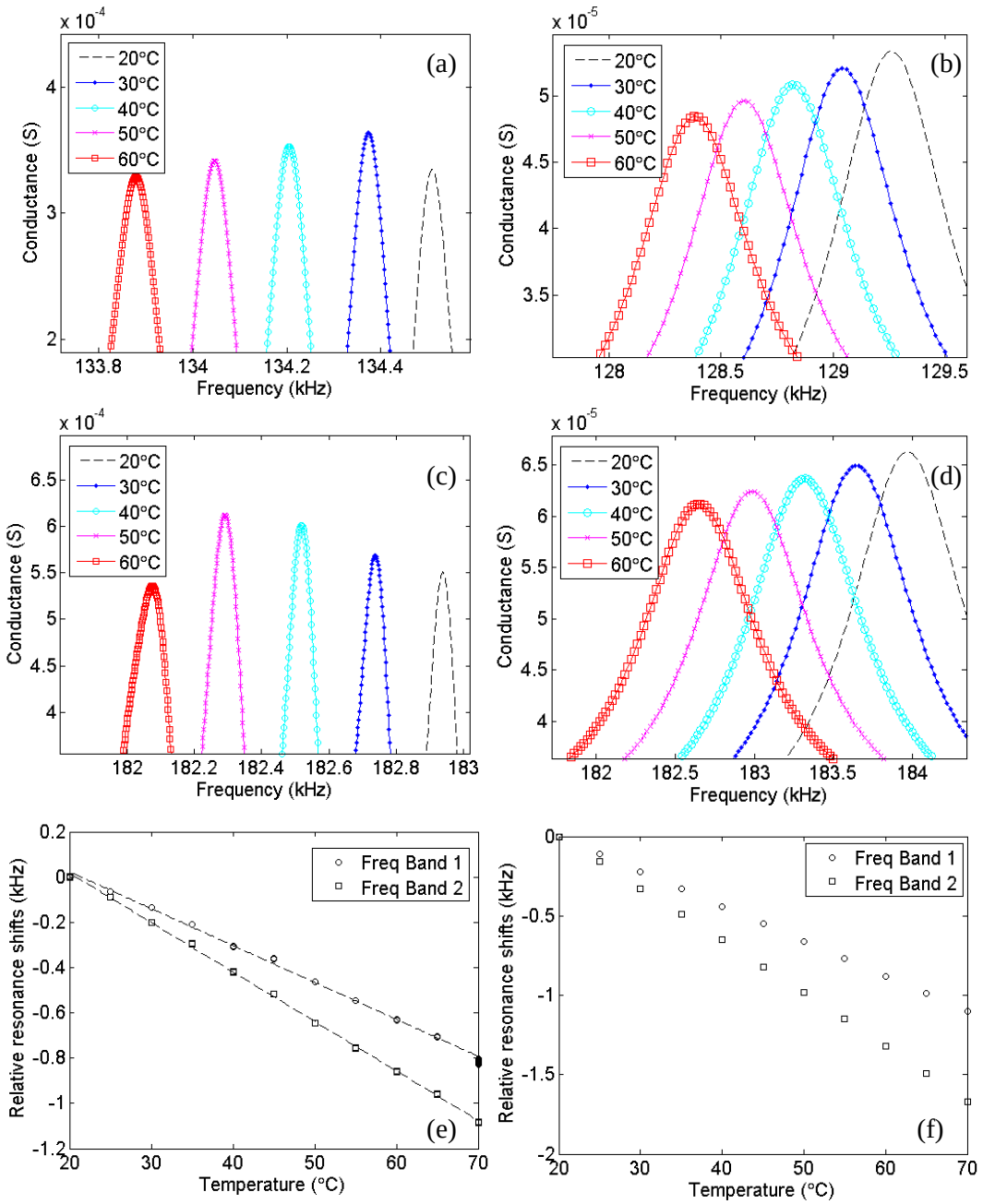

Figure 3.2 The structural resonance around 130 kHz from the conductance spectrum from (a) experiments and (b) analytical model; the structural resonance around 182 kHz from the conductance spectrum from (c) experiments and (d) analytical model; the relative resonance peak shifts based on two resonances (e) from experiments and (f) from model results

baseline measurement, was investigated:

$$\mathbf{RMSD} = \sqrt{\frac{\sum_{i=1}^{N}(y_i - x_i)^2}{\sum_{i=1}^{N} x_i^2}} \qquad (\mathbf{3.1})$$

where $\boldsymbol{y_i}$ is the baseline admittance value and $\boldsymbol{x_i}$ is the measurement admittance.

3.6 Thermal stress characterization

The features discussed in the previous section were extracted from the data of the EC test and the CWR test. The ideal feature(s) for thermal stress characterization would be sensitive to the thermal stress with little effect from temperature variations. The previous model and experimental studies explained that all the features considered in this study are sensitive to temperature variations. Therefore, a univariate analysis was first conducted to understand the individual tendencies of each feature. The features were selected based on the criteria of good separation between two cases. Two temperature compensation strategies were proposed: providing the information of measurement temperatures, a regression model was proposed to eliminate the temperature effects; without the temperature measurements, a Principle Component Analysis (PCA) was conducted and the feature vectors were reconstructed without the component(s) corresponding to large variations, which was presumably caused by the changing temperatures.

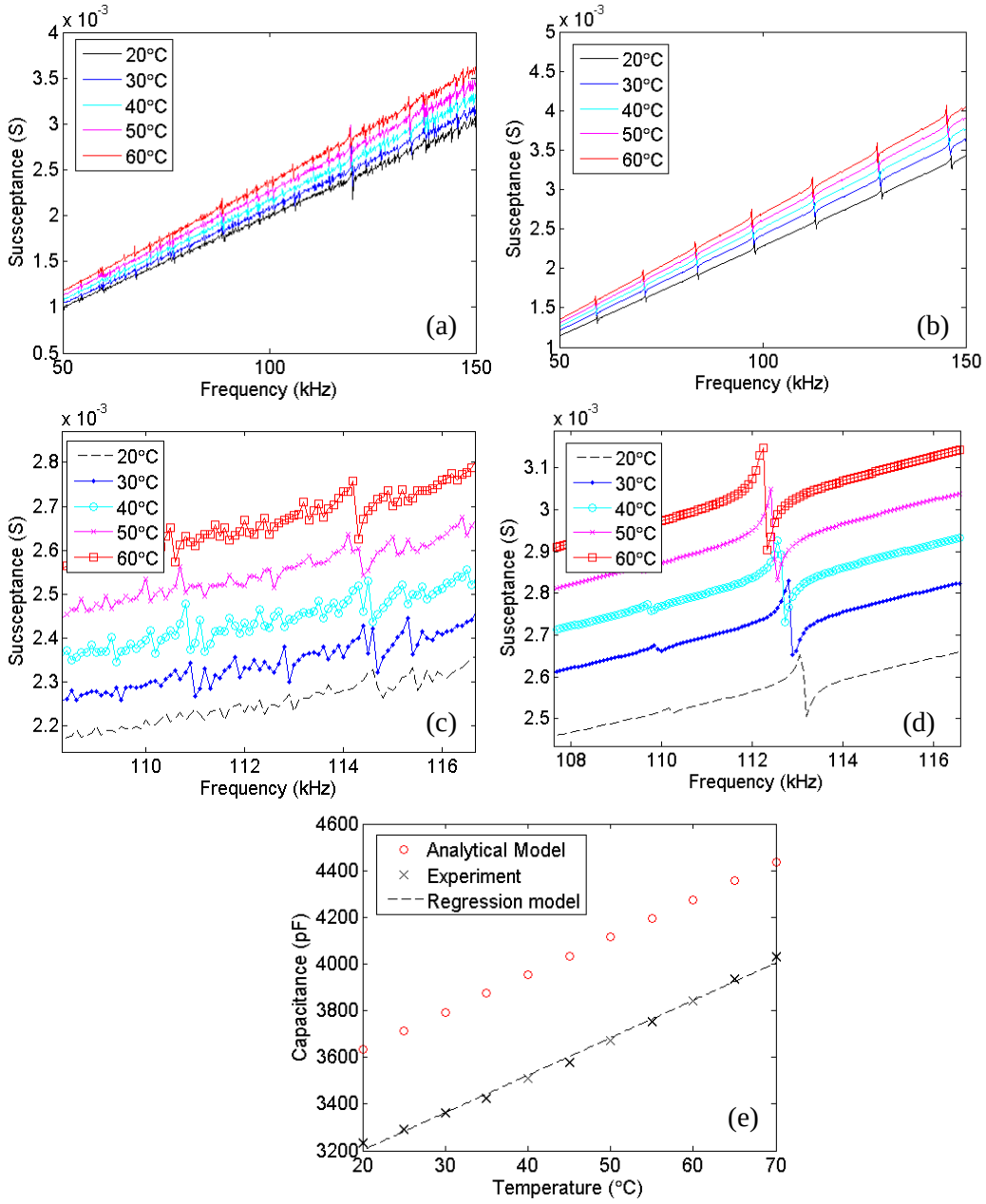

Figure 3.3 The susceptance signatures for varying temperatures from (a) the experiments and (b) from analytical model; the zoomed-in frequency band from (c) the experiments and (d) from analytical model; the capacitance changes vs temperatures from the analytical model and experimental results

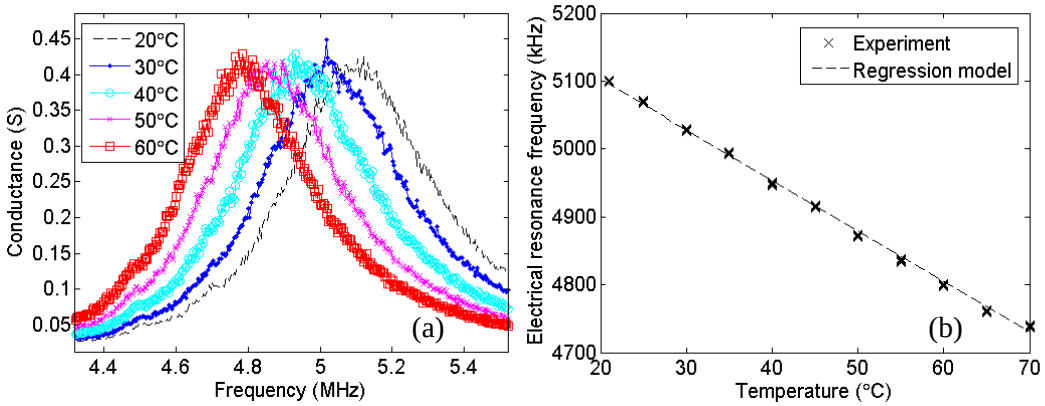

Figure 3.4 (a) experimental conductance spectra for varying temperatures from EC test; (b) the experimental shift of the electric resonance peak based on 50 experimental measurements

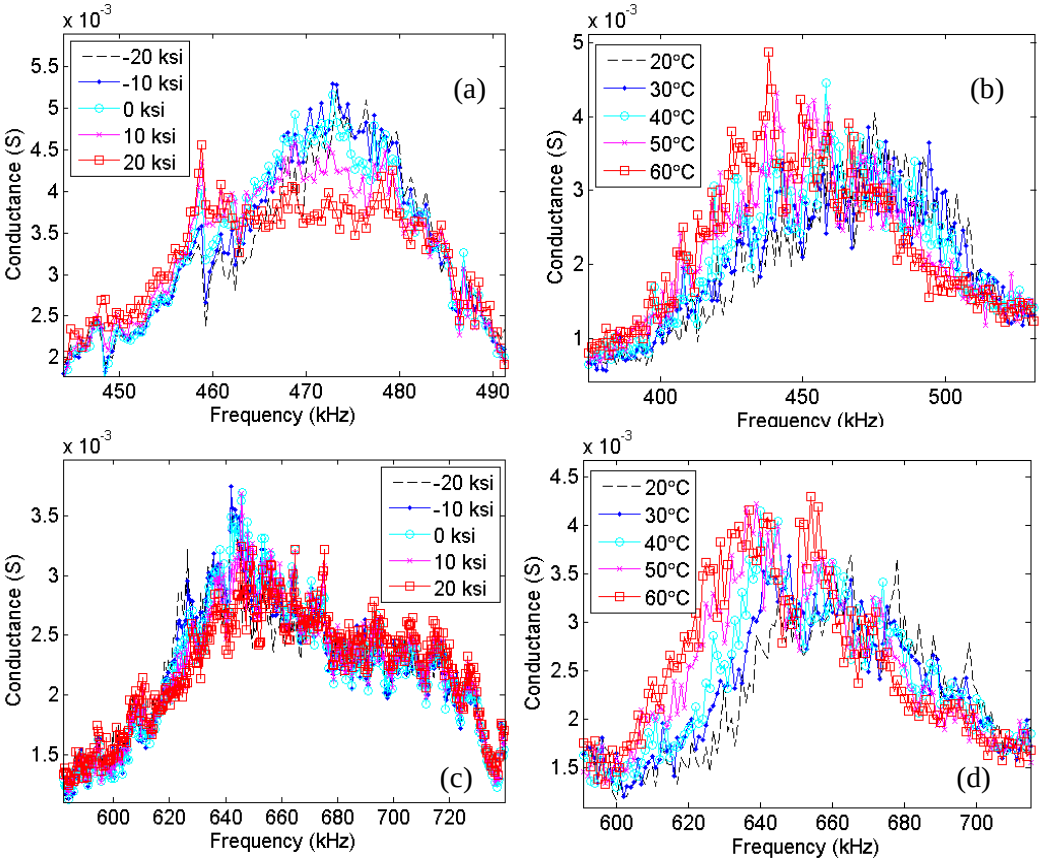

Figure 3.5 (a) experimental conductance spectra for varying temperatures from EC test; (b) the experimental shift of the electric resonance peak based on 50 experimental measurements

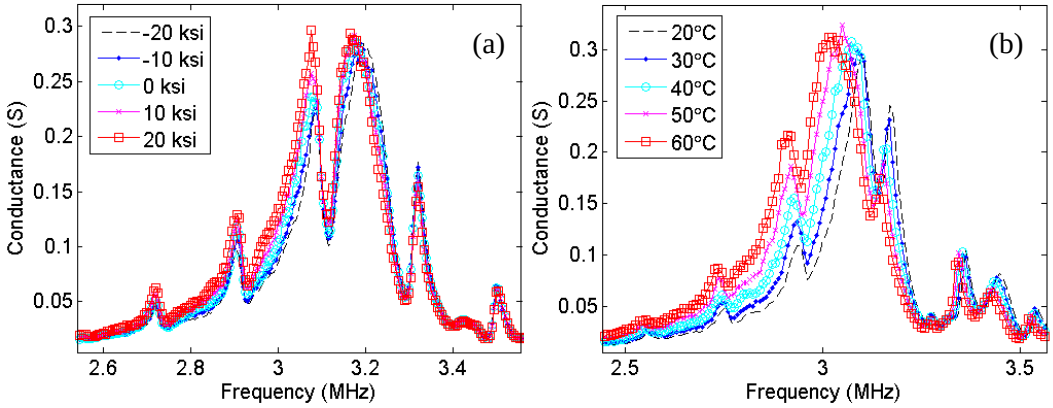

Figure 3.6 The experimental conductance spectra including the thickness modes for (a) varying uniaxial load test (MTS test), and (b) for varying temperatures from the EC test.

3.6.1 Univariate analysis

Previous studies reported the effectiveness of features including the RMSD and the similarity corresponding to the structural resonances in the EMI conductance spectrum for damage detection. Moreover, the influences of temperature variations on these features can be eliminated by the methods of effective frequency shift (EFS) and minimum RMSD [81, 83], by which the test admittance signatures can be horizontally and vertically shifted towards the baseline measurement in order to compensate for the natural frequency shifts in the spectrum due to varying temperatures. For defect detection purpose, with the aforementioned temperature compensation algorithms, the features of RMSD and similarity can preserve the changes in the structural dynamic characteristics resulting from structural damage by comparing the compensated signatures with the baseline measurement (pristine structure). Unfortunately, for the case at hand of thermal stress characterization, the temperature compensation algorithms of EFS or minimum RMSD would be ineffective, because they will

eliminate the influences of both the temperature and thermal stress. Essentially, the variations of these features due to thermal stress are not ‘orthogonal’ to the ones due to varying temperatures. Also, it is challenging to differentiate the influences from the temperature and the applied stress, given the high temperature sensitivities and low stress sensitivities of these conventional EMI features based on the structural resonances. Therefore, a new set of features was investigated for further analysis. Based on the previous model and experimental studies, the features include two structural resonances, two in-plane PZT resonances, two thickness resonances, as well as the electrical resonance and capacitance of the PZT, as shown in Table 3.1.

The features from the EC test and the CWR test are shown in Fig.3.7. All the features have been zeroed referring to their baseline measurements at 25 ℃ for comparison. Based on the previous discussion, the features from structural resonances are less favorable due to the high temperature sensitivity and comparable low stress sensitivity (Fig.3.7 Feature #1-6). Particularly, for the high frequency bands (180-185kHz), the temperature effects dominate the variations of the structural resonance and no discrimination can be identified between the two tests. To be specific, Feature #5 in Fig.3.7 shows larger relative structural resonance shift around 133-135 kHz in the CWR test (circles) compared to the ones in the EC test (squares). While the raising temperature softens the host structure, PZT, and the bonding layer, the thermal-induced load leads to a lower natural frequency due to structural dynamics. From

Fig.3.7, Feature#6 shows overlap of the relative structural resonance shift around 180-185 kHz from both tests, which mainly results from the larger resonance frequency shift at higher frequency band due to temperature variations. A similar phenomenon can be found in Fig.3.7, referring to feature #1 to 4: larger deviation (smaller similarity) from the baseline was observed in the CWR test; less difference between the EC test and CWR test was found in the features based on the resonance at higher frequency band. Since this issue cannot be solved by conventional EFS algorithms, this study explored the features based on the in-plane PZT resonances, the thickness modes, electric resonance and the capacitance.

The features based on the resonances around 400-520 kHz and 600-720 kHz are shown in Fig. 3.7 feature # 7 to 12. The temperature variation softens the host structure, bonding layer and the PZT patch, which leads to resonance shift towards lower frequency range. On the other hand, the PZT properties (d_{31} and ε_{33}) vary with the increasing thermally-induced stress, which will result in a variation of the resonance magnitude. It is noticeable the feature variations can result from both the in-plane PZT resonances and the structural resonances. The features of similarity and the RMS (features # 9, 11 and 12) provide good separation between the two tests and linearity with respect to the increasing temperatures.

Table 3.1 Feature list considered for thermal stress characterization

	Feature	Frequency		Feature	Frequency
	1. RMSD	133-135kHz		13. RMSD	2-4MHz
	2. RMSD	180-185kHz		14. RMSD	2.8-3.5MHz
Structural	3.Similarity	133-135kHz	**Thickness**	15. Similarity	2-4MHz
Resonance	4. Similarity	180-185kHz	**mode**	16. Similarity	2.8-3.5MHz
	5. Shifts	133-135kHz		17. RMS	2-4MHz
	6. Shifts	180-185kHz		18. RMS	2.8-3.5MHz
	7. RMSD	400-520kHz	**Electrical resonance**	19. Shifts	4-7 MHz
	8. RMSD	600-720kHz			
In-plane	9.Similarity	400-520kHz	**Susceptance**	20. Capacitance	50-100 kHz
modes	10.Similarity	600-720kHz			
	11. RMS	400-520kHz			
	12. RMS	600-720kHz			

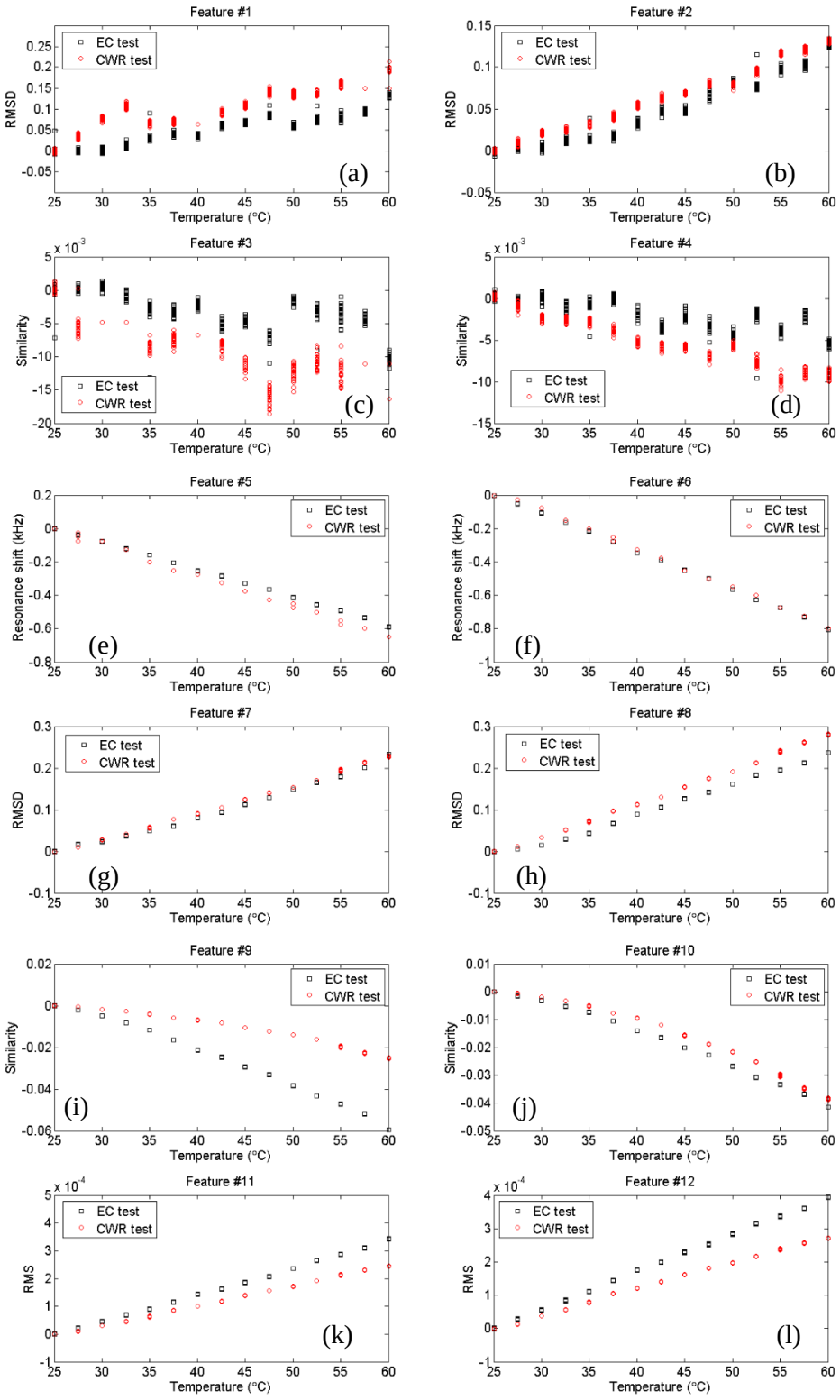

Figure 3.7 Feature 1-20 based on the structural resonances, PZT resonances, thickness resonances, the electrical resonance and capacitance from environmental chamber test and thermal stress test.

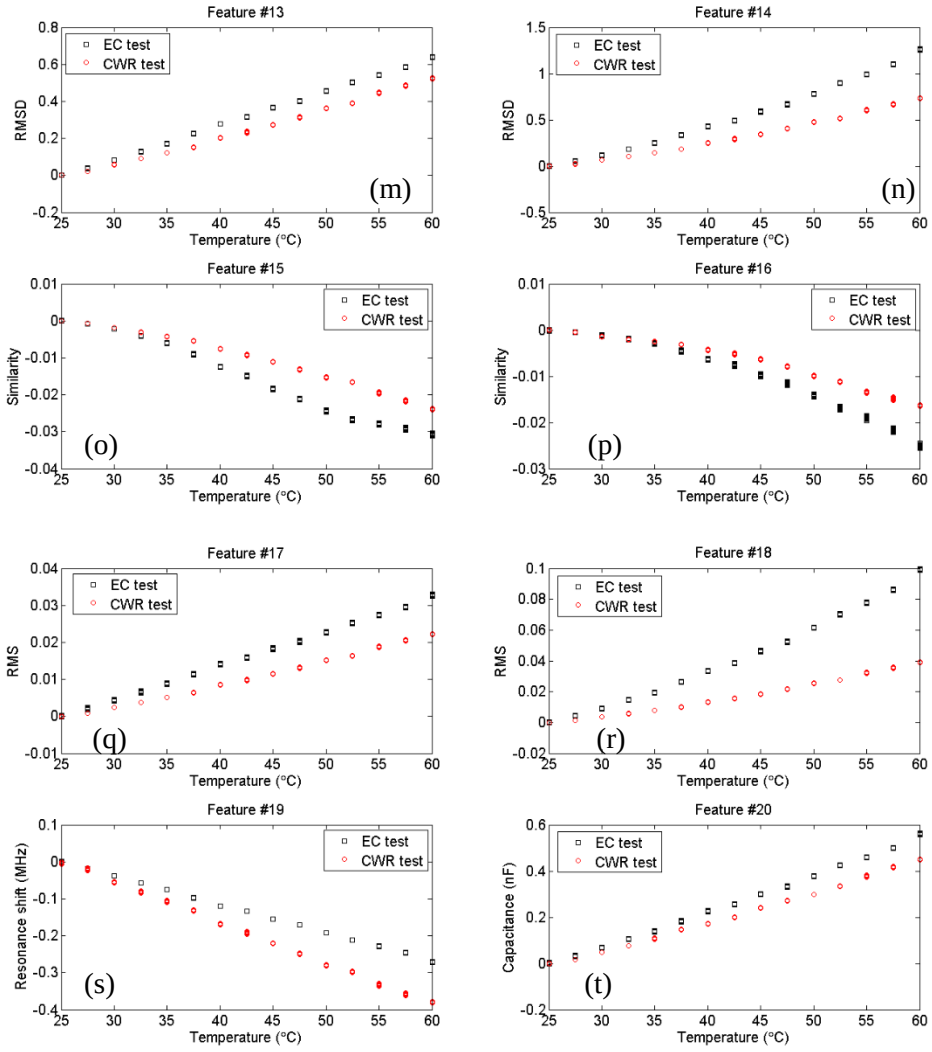

Figure 3.7 Feature 1-20 based on the structural resonances, PZT resonances, thickness resonances, the electrical resonance and capacitance from environmental chamber test and thermal stress test. Continued

The features based on the thickness resonances around 2-4 MHz and 2.8-3.5 MHz are shown in Fig. 3.7 (features # 13 to 18). The increasing temperature would soften the host structure, bonding layer and the PZT patch. On the other hand, the PZT properties of d_{33} would vary as the increasing thermally-induced stress, which will results in the variation of the thickness mode magnitude. It is noticeable the feature variations can result from both the PZT resonances and the structural resonances. The features of RMSD and the RMS (features # 14, 17 and 18) provide good separation between two tests and linearity along the increasing temperatures.

The features based on the capacitance and electrical resonance around 4-7 MHz are shown in Fig. 3.7 (features # 19 to 20). The temperature variation would modify the material properties (ε_{33}). On the other hand, the PZT properties would vary as the increasing thermally-induced stress (ε_{33}), which results in the variation of the capacitance and, therefore, the electric resonance. The features of the electric resonance shift and the capacitance (features # 19 and 20) provide good separation between the two tests and linearity with temperature.

A potential approach for thermal stress characterization using the EMI method would be a sophisticated and detailed model with inputs of temperatures and thermally-induced stresses that lead to features variation. However, it is challenging, if not impossible, to identify the geometric, mechanical, piezoelectric parameters and their temperature/stress sensitivities accurately enough to find a quantitative description of all involved physical phenomena.

Therefore, two data-driven temperature compensation methods based on regression analysis and eigenvector analysis were proposed for the thermal stress characterization using the EMI method.

3.6.2 Regression analysis

When the temperature measurements are available, a linear dependence of the selected features on temperature were assumed, considering the applied temperature and stress ranges [69,71]. The estimated feature vector under temperature variations can be approximated by the regression models based on the EC test data. Then, the observed temperatures in both tests and the regression models can be used to predict the feature vector under the test temperatures. While the models preserve the information on how the varying temperatures affect the selected features, the residuals (error between the measurement and the prediction) can be used to characterize the variations associated to the thermally-induced stresses.

Furthermore, to better evaluate the performance of the residuals from the CWR test based on individual features with respect to regression models, the Receiver Operating Characteristic (ROC) curves were computed. These curves represent the compromise achievable between true positives and false positives. For each feature, the true and false positive rates were determined by accepting or rejecting the hypothesis of the test data results from given thermal stress levels among all the measurements. The ROC curves of selected features for different thermal stress levels are shown in Fig. 3.8. In these features, the 45°

black dashed lines represent random guess. The ideal curves should be located at the upper left corner of the plot, implying high true positive rates with low false positive rates. For example, the ROC curves for different features at a thermal stress corresponding to 45℃ are shown in Fig. 3.9. The plot suggests that features based on structural resonances lay closer to the random guess, while features based on the in-plane PZT resonance, thickness mode and capacitance stay close to the upper left corner. Therefore, the latter features outperform the former features, in terms of successfully identifying the 45℃ thermal stress level. To quantify the overall performance of the features, the Area Under Curve (AUC) was computed for each feature and averaged across thermal stress levels: the larger the area under curve, the better the performance of the feature. The AUC results are shown in Fig. 3.10, where the in-plane PZT resonance, out-of-plane PZT resonance, electrical resonance and the capacitance provide the best clustering behavior among incrementally developed thermal stress levels. By ranking the averaged AUC, eight features were identified for best performance (feature#9, 11, 12, 14, 17, 18, 19 and 20).

For these eight features, the linear models were fitted to the data from the EC test. The residuals between the observed features and the estimated features were used for thermal stress characterization, as shown in Fig. 3.11. While the residuals from the selected features from EC test are approximately zero under varying temperatures, the residuals from the CWR test were linearly associated with the increased thermal stresses, represented as dashed line in Fig. 3.11.

Given the recorded temperatures, the induced thermal stress can then be estimated by interpolation based on the regression models and the differences between the measured feature vector and the estimated vector.

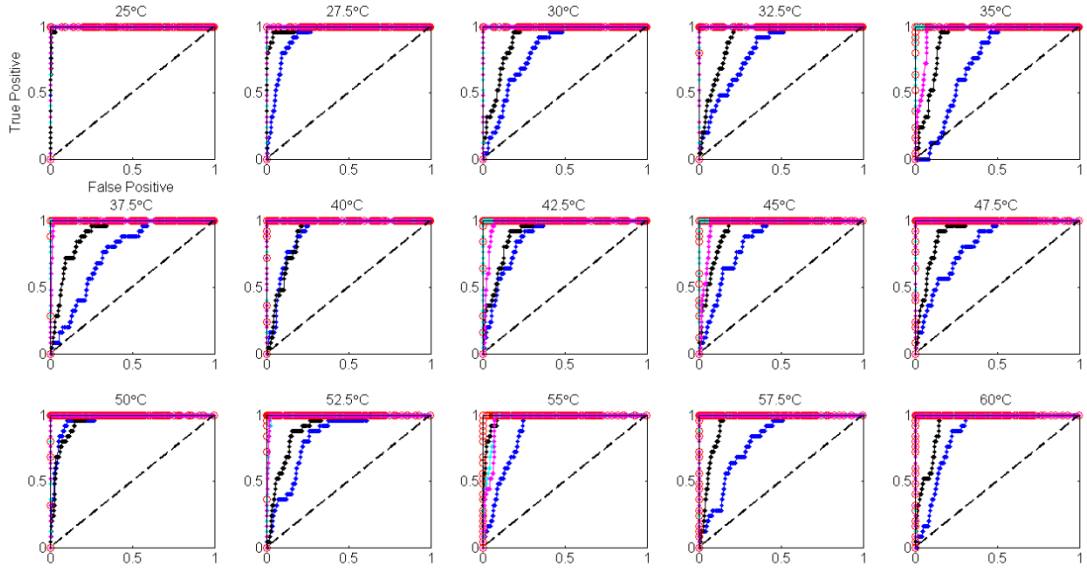

Figure 3.8 The ROC curves of selected features under thermal stress levels corresponding to temperature range from 25℃ to 60℃.

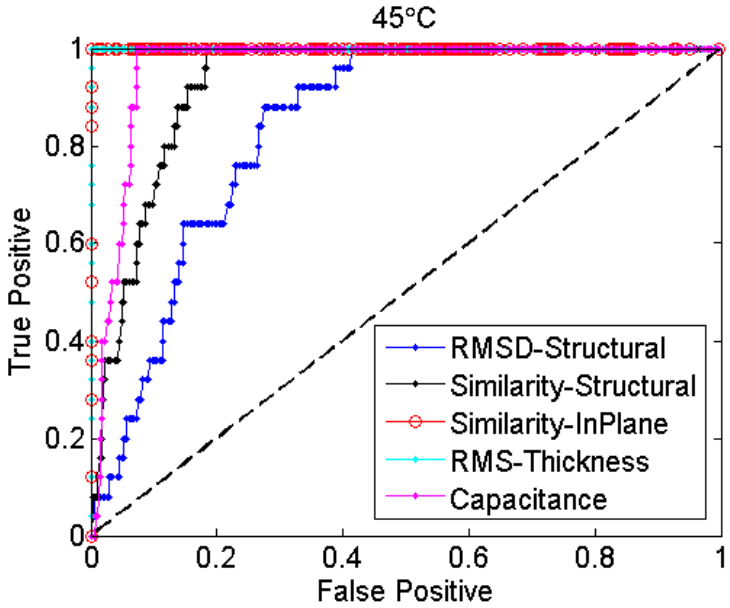

Figure 3.9 The ROC curves of selected features under thermal stress levels corresponding to 45℃.

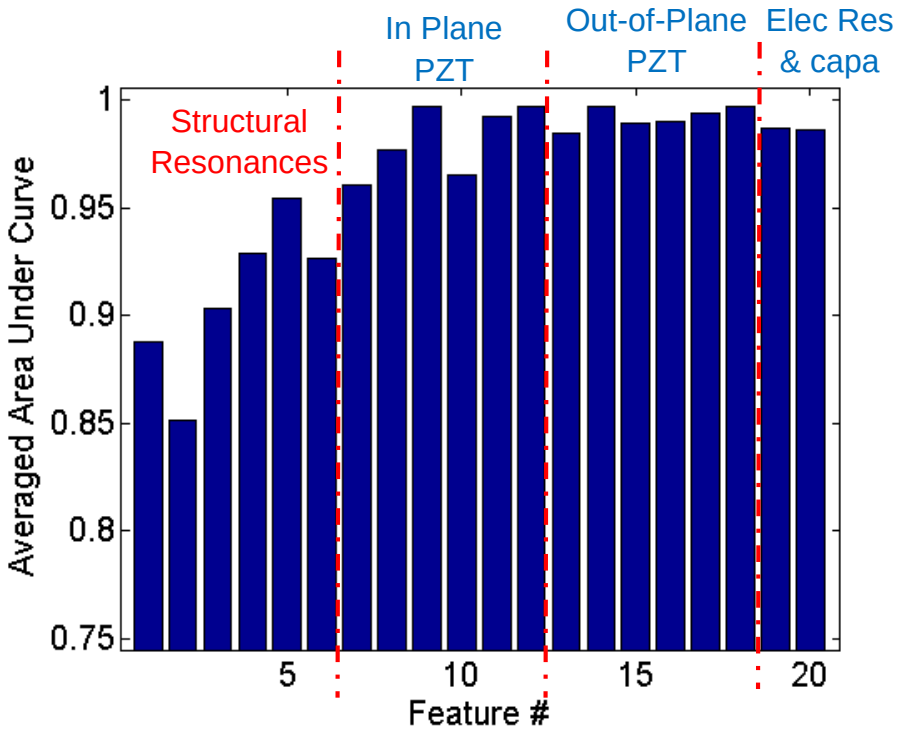

Figure 3.10 The ROC curves of selected features under thermal stress levels corresponding to 45℃.

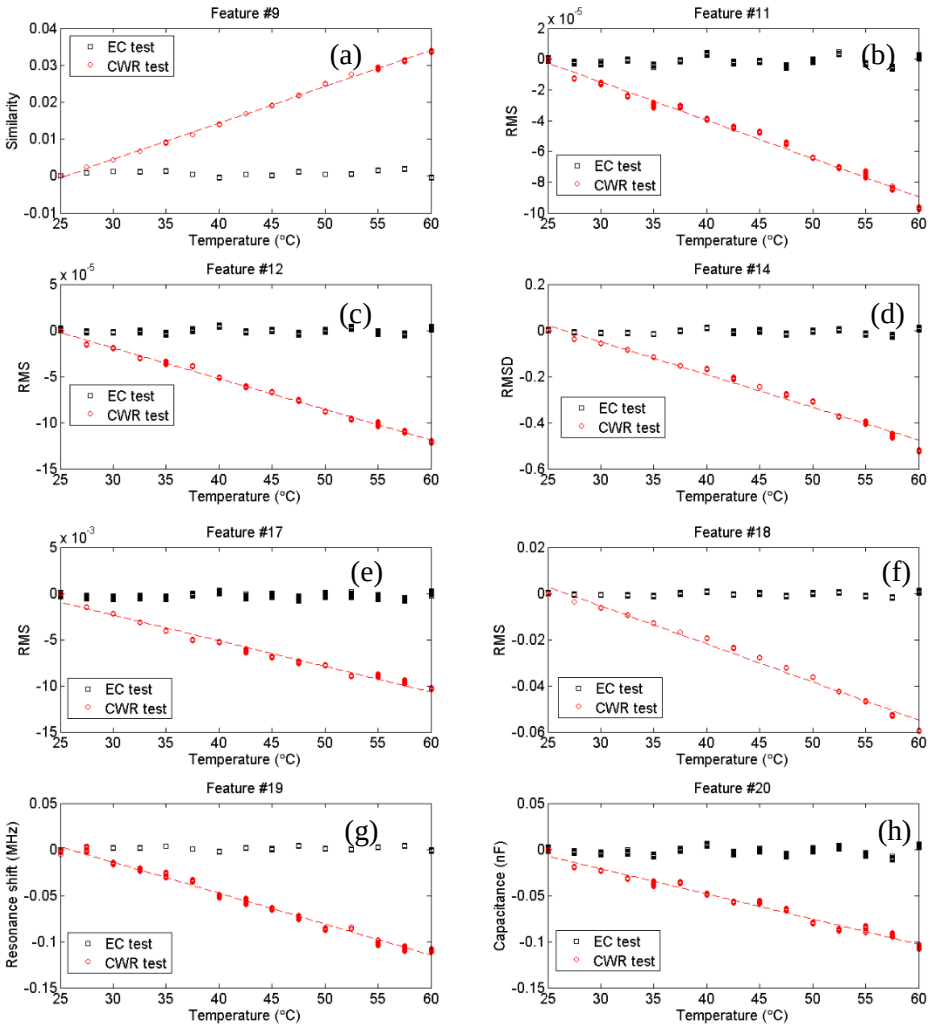

Figure 3.11 The residuals of selected features: the similarity and RMS values from PZT resonance (feature # 9, 11 and 12), the RMSD and RMS from the thickness mode (feature # 14, 17 and 18), the electric resonance shift (feature # 19) and the capacitance (feature # 20).

3.6.3 Principal components analysis

When the temperature measurements are not available, the Principal Component Analysis (PCA) can be applied to capture the underlying relationship between temperature variations and the features based on the EM admittance signatures. PCA is commonly used in machine learning for dimensionality reduction and visualization. In the field of SHM, previous researchers have applied PCA to various feature spaces in order to visualize the data of different structural states or de-couple the structural damage effects from environmental and operational variability [74,75,78].

PCA identifies a set of mutually orthogonal projection vectors that capture the largest scatter of the data set, and the resulting orthogonal basis are in descending order based on the variance they preserve. These orthogonal basis are known as principal components (PC), which can be computed as the eigenvectors of the covariance matrix Σ of the training data set.

$$\Sigma = E(x-\mu)(x-\mu)^T \tag{3.2}$$

where E is the expectation, x is the vector variable with dimension of k by 1, μ is the mean data vector with dimension of k by 1. By solving for the eigenvectors $\boldsymbol{v}_i$ of Σ, the individual data vector x with dimension of k by 1 can be represented using the orthogonal basis as:

$$x = \sum_{i=1}^{n} p_i \boldsymbol{v}_i = p_1 \begin{bmatrix} \vdots \\ \boldsymbol{v}_1 \\ \vdots \end{bmatrix} + p_2 \begin{bmatrix} \vdots \\ \boldsymbol{v}_2 \\ \vdots \end{bmatrix} + \cdots + p_n \begin{bmatrix} \vdots \\ \boldsymbol{v}_n \\ \vdots \end{bmatrix} \tag{3.3}$$

where the vector $\boldsymbol{v}_i$ (k by 1) is the i[th] PC, and the scalar p_i is a weight coefficient. The coefficients p_i can be easily found by projecting the individual data vector x onto the i[th] basis,

$$p_i = x^T \boldsymbol{v}_i \tag{3.4}$$

Based on previous model and experimental studies, temperature variations significantly affect the EMI measurements, while the developed thermal stresses in CWR test had less influences on the features from Table 3.1. Since the first few PCs account for the largest proportion of variance in the data, with the data set of the unconstraint structure subject to changing temperatures, the first PC or the first few PCs of the data set are presumed to correspond to the temperature variations, while the succeeding PCs should be less sensitive to the environmental variability. By discarding the PCs associated to the variations led by the changing temperatures, the reconstructed feature vectors can be used to isolate the variations associated with the thermally-induced stresses.

First, the covariance matrix and the orthogonal basis were generated from the training data, composed by the selected features from a subset of the EC test data. Secondly, the feature vectors based on the data set of EC test and CWR test were projected onto the orthogonal basis developed in the first step and the weight coefficients of each PC for all measurements were computed. Thirdly, in order to eliminate the temperature effects, the feature vectors were projected onto the orthogonal basis and reconstructed without the first two eigenvectors. Lastly, as a further step of feature fusion, the reconstructed feature vectors of CWR test were

fed into a clustering algorithm, the outlier analysis, with the measurement at 25℃ as the training data.

The covariance matrix of the features, including features # 9, 11, 12, 14, 17, 18, 19 and 20 using a subset of EC test data was first computed, where the subset is composed by the first 10 measurements at each temperature increment, ranging from 25℃ to 60℃. The features were selected based on criterion described in previous section, by the rank of averaged AUC of ROC curves and linearity with respect to incrementally developed thermal stresses. After the eigenvector analysis, the feature vectors of the EC test and CWR test were projected onto the eight principle components, as shown in Fig. 3.12. The dashed vertical lines separate 25 measurements at each temperature steps (2.5℃ increments from 25℃ to 60℃).

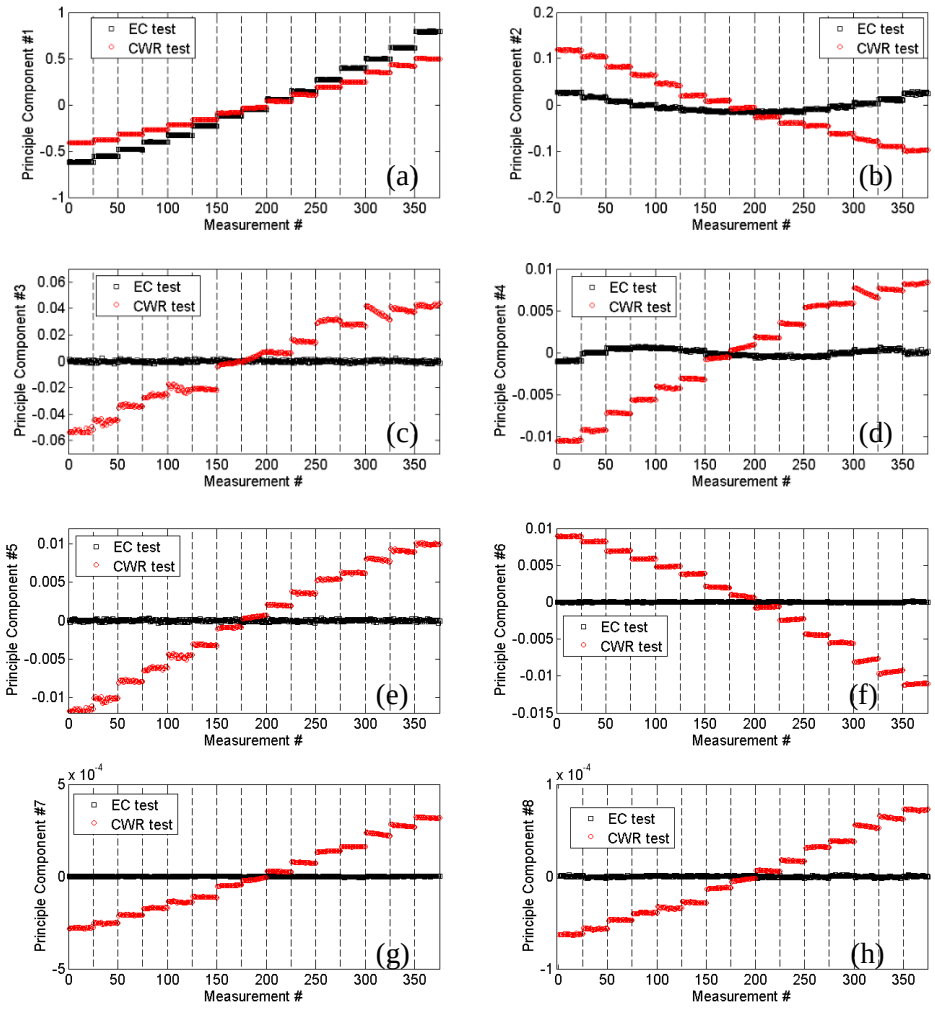

Figure 3.12 Eight principal components based on the training set from the EC test based on the selected features: the similarity and RMS values from PZT resonance (feature # 9, 11 and 12), the RMSD and RMS from the thickness mode (feature # 14, 17 and 18), the electric resonance shift (feature # 19) and the capacitance (feature # 20).

As expected, the eigenvalue analysis reports that over 99 percent of the full data variance has been encapsulated in the 1st principal component, led from the changing

temperatures for both the EC test and CWR test. It is also noticeable that there are substantial differences between the two tests with projection onto the 1st PC, resulting from the influences associated with the thermally-induced stresses. By discarding the 1st orthogonal basis during reconstruction, the influences of the thermal stresses are also partially suppressed. While the 2nd PC is less sensitive to temperature variation, the nonlinear trend in the EC test suggest the residuals of temperature influences and possibly the inaccuracy of the linear assumption. In Fig. 3.12, the 3rd to 8th PCs are shown insensitive to the changing temperatures. Therefore, the feature vectors were reconstructed without the first two PCs to minimize the environmental variability, as shown in Fig. 3.13. The reconstructed features from the EC test were close to constant through the wide temperature range, and different levels of the developed thermal stress can be clearly characterized by the reconstructed features from the CWR test, especially for features #9, 11, 12 and 18. The variation within the same temperature step, such as measurements from 301 to 325, can mainly result from the temperature variation at given test steps due to the implement feedback control of the heating element.

Furthermore, to quantify the performance of reconstructed features, the ROC curves were computed, in a similar manner described in the previous section. The ROC curves of selected reconstructed features among different thermal stress levels are shown in Fig. 3.14. For thermal stress corresponding to 45℃, all the reconstructed features provide ideal performance with similar AUC. For the case of 55℃ thermal stress (measurement#301 to

325), the reconstructed feature# 12 and feature# 18 showed the largest AUC performance. It is noticeable that the temperature variation within each step is not be compensated with this approach, since this eigenvector filtering process does not include the within-class variance. The averaged AUC were computed and the best performed reconstructed features were identified as feature#11, 12, 17 and 18.

These reconstructed features were then used to feed an unsupervised learning algorithm based on the outlier analysis. An outlier is a datum that appears inconsistent with the baseline, i.e. a set of data that describes the normal condition of the structure under investigation. Ideally, the baseline should include typical variations in environmental or operative conditions (e.g. temperature, humidity, and loads) of the structure. In this case, after temperature compensation based on PCA, the reconstructed feature vectors at 25℃ were used as baseline, such that the outlier analysis can further separate the measurements at different thermal stress levels, by combining all the selected reconstructed features. While the alternatives can be the K-means clustering method or Expectation Maximization algorithm, the outlier analysis can illustrate the basic idea of feature fusion. For the multivariate analysis, the discordancy test can be expressed by the Mahalanobis Squared Distance (MSD), D, which is a non-negative scalar defined as:

$$\mathrm{D} = (x-\mu)^T [K]^{-1} (x-\mu) \tag{3.5}$$

where x is the potential outlier vector, μ is the mean vector of the baseline, K is the covariance matrix of the baseline, and T symbolizes the transpose operation. Both vectors x and μ are p-dimensional, whereas K is a square matrix of the order p. As shown in Fig. 3.15, the measurements with different thermal stress levels are further separated, after the outlier analysis.

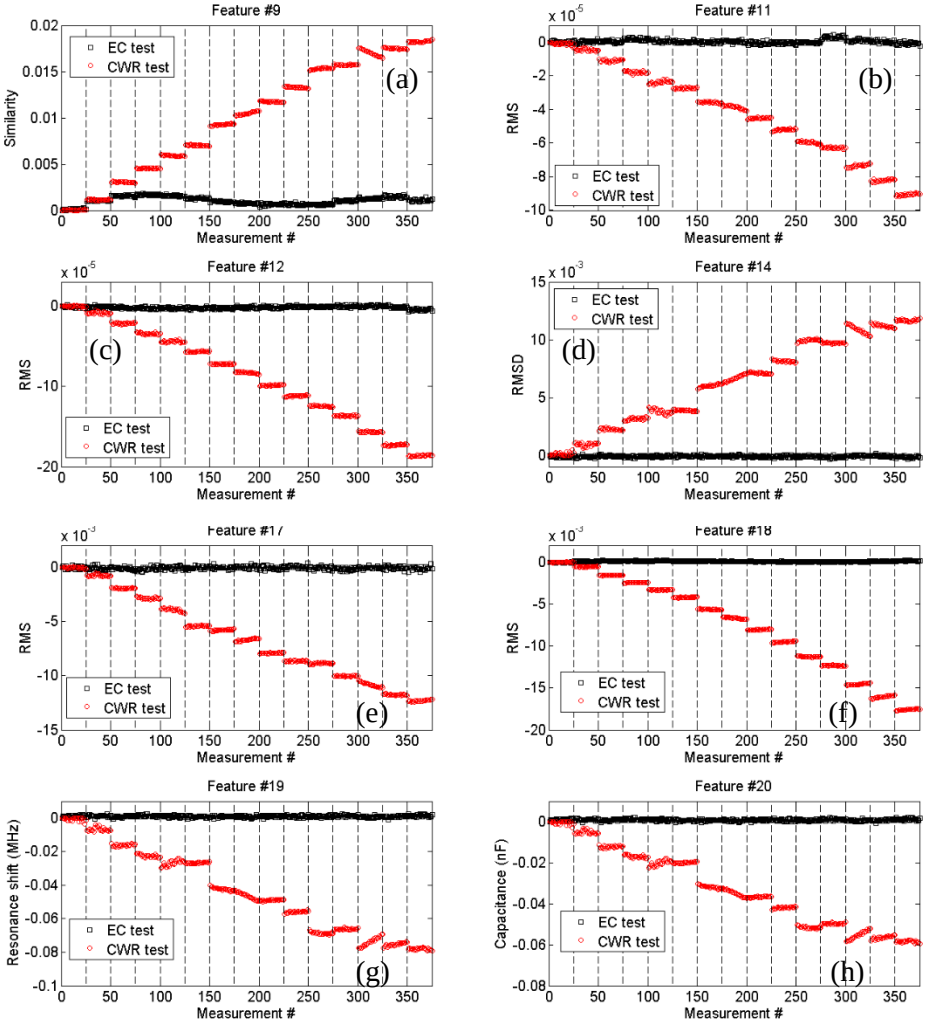

Figure 3.13 The selected features after principle components reconstruction without the first two components (feature # 9, 11, 12, 14, 17, 18, 19 and 20).

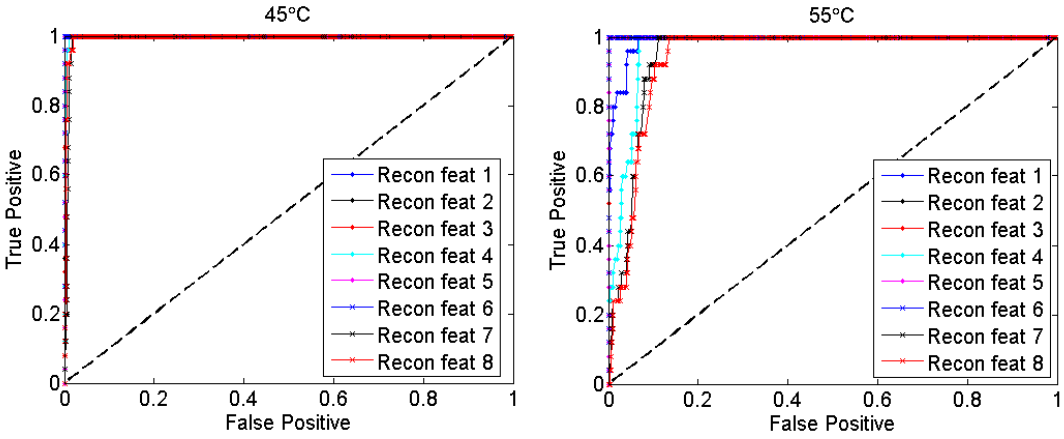

Figure 3.14 The selected features after principle components reconstruction without the first two components (feature # 9, 11, 12, 14, 17, 18, 19 and 20).

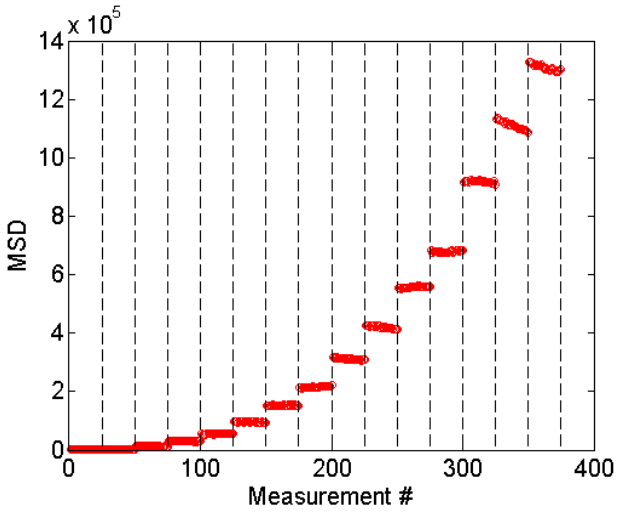

Figure 3.15 The Mahalanobis squared distance using four features after principal components reconstruction.

3.7 Discussion and conclusions

In this study, an investigation was conducted to explore the EMI method for thermal stress estimation. The temperature influences on the EMI measurements across the admittance spectrum were explicitly and comprehensively studied through analytical models and experimental tests. Two temperature compensation strategies were proposed to isolate the effects of thermal stress.

Analytical models based on one dimensional EMI model were proposed to simulate the influences of temperature on the admittance signatures. Given the one dimensional EMI model coupled with the structural dynamics, the temperature-sensitive parameters can be updated into the model by keeping the first order term in Taylor's expansion. This comprehensive model is able to not only take into account the influences of the temperature on structural dynamics, but also the key operating parameters of the PZT element itself.

The environmental chamber test and the Continuous Welded Rail test were conducted with a steel bar machined from the web section of a 136RE rail track. Two frequency bands were covered to explore various potential stress indicators. For the conductance signatures, the resonances were found to linearly shift towards lower frequency when subject to raising temperature, for both the model and experimental results, mainly resulting from the softening of the substructure. The temperature sensitivity of the resonance shifts in the conductance is 220 Hz/10℃ and it is frequency-dependent, while the stress sensitivity of the resonance shifts

in the conductance is 2.6 Hz/ksi. For practical use of this feature, the challenge would be the frequency resolution or the computation power of the DAQ system, since it requires at least 0.5 Hz resolution in order to capture the stress variability of 1 ksi for steel. Moreover, the structural resonances shift due to mechanical load can be easily masked by the temperature effect. Thus, temperature compensation would be challenging with such frequency-dependent temperature effects.

On the other hand, the slopes of susceptance, equivalent to the capacitance of the piezoelectric element, were demonstrated to vary linearly with increasing temperatures, in both the model and the experiments. The temperature sensitivity of the resonance shifts in the conductance is 157 pF/10℃, while the stress sensitivity of the capacitances from the susceptance signatures is 6.63 pF/ksi for steel specimen. The commercialized LCR meters or impedance analyzers are found to be provide measurement sensitivity of 1e-3 pF for capacitance measurement. The ratio between the stress and temperature sensitivities is higher than that based on structural resonance shift. Thus, the capacitance of the bonded PZT patch is a suitable stress indicator, with less hardware limitation, compared to the conductance resonance peaks.

Furthermore, the electric resonance frequency for the impedance measurement system was characterized, and the temperature sensitivity of 73.5 kHz/10℃ was observed, while the stress sensitivity of the electric resonance shift rate was found 4.1 kHz/ksi for the steel

specimen. The ratio between the stress and temperature sensitivities has been further improved by taking advantage of the electric resonance. Considering the high frequency range (~5 MHz) in this case, the resonance frequency can be lowered by introducing high capacitance component(s) into the circuit, to eliminate the limitation on the DAQ hardware (clock, power consumption and stability).

Based on the model and experimental results, a feature list composed of the structural resonances, the in-plane PZT resonances, the out-of-plane PZT resonances, the electrical resonances and the capacitance was proposed. The univariate analysis was first conducted to evaluate the performance of the individual features differentiate the EC test (temperature only) from the CWR test (temperature plus thermal stress). The features were fed into two temperature compensation strategies. When the temperature measurements are available, regression models were constructed between the features and temperature, and the error between the measured features and the estimated ones were computed as a practical indicator of thermal stress. Without using the temperature information, a PCA was conducted to eliminate the effects of temperature affecting the first few PCs. The reconstructed feature vectors without the first two PCs were shown to be suitable thermal stress indicator, while insensitive to temperature. In both methods, the ROC curves were computed to quantify the feature performance.

3.8 Acknowledgements

This chapter, in part, is currently in preparation for submission to the Journal of Intelligent Material Systems and Structures, Zhu, Xuan; Lanza di Scalea Francesco; (2016). The running title of this paper is *Thermal Stress Measurement Using the Electro-Mechanical Impedance Method and its application in Continuous Welded Rails*. The dissertation author will be the primary investigator and primary author of this paper.

4. Thermal Stress Measurement in Continuous Welded Rails Using the Hole-Drilling Method

4.1. Introduction

The hole-drilling method, a semi-destructive test procedure first introduced by Mathar in the 1930s [8], is one of the most widely used approaches to determine near-surface *in-situ* stresses (most typically residual stresses). The method features good accuracy and reliability [9], ASTM standardized test procedures [10, 11], and well-established practical implementations [12]. The small drilled holes are often tolerable and/or repairable [13].

Early works in the 1960s and 1970s demonstrated the method's effectiveness and accuracy (better than $\pm 8\%$ for steel) for the measurement of near-surface residual stresses in elastic materials [9, 14]. At that time, the calibration coefficients were computed based on experimental results and empirical relationships for given hole diameters. In the 1980s, Schajer [15, 16] proposed a systematic framework to compute the calibration coefficients for the cases of uniformly and non-uniformly distributed residual stresses along the hole depth, based on the principle of superposition and axisymmetric finite element models. In these models, the non-axisymmetric loads necessary to compute some of the coefficients were handled by special 2D finite elements that used Fourier series expansion in the circumferential direction. Other researchers [17, 18] calculated the calibration coefficients by using a 3-D finite element model with an integral method and verified the coefficients with experimental results.

The specific application of interest to the present study is the *in-situ* measurement of thermal stresses in CWR, which is still an unresolved problem in railroad maintenance practice.

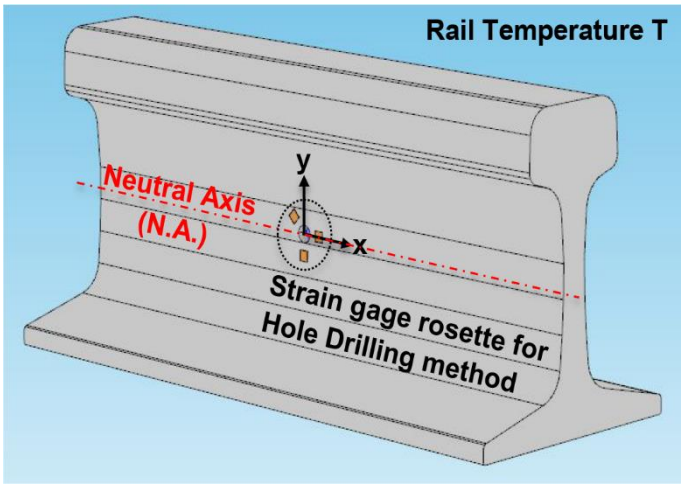

Figure 4.1 Envisioned application of the hole-drilling method to estimate in-situ thermal stresses (hence rail Neutral Temperature) in Continuous-Welded Rail (hole and gage sizes not to scale).

This chapter explores the hole-drilling strain-gage method as a possible solution to measure the *in-situ* thermal stresses in rails and therefore estimate the rail Neutral Temperature. The envisioned method uses a hole drilled in the rail web at the rail Neutral Axis (N.A.), Fig. 4.1, thereby minimizing any impact on the structural strength of the rail. The hole drilling releases both the thermal stresses and the residual stresses present in the rail. Particular care, therefore, needs to be taken to compensate for the residual stress component, that has no role in the determination of the rail NT. For this goal, the current paper experimentally

establishes a linear relationship between the longitudinal and the vertical residual stresses at the rail N.A., in analogy with what done by previous studies using magneto-elastic methods [15]. This linear relationship allows one to estimate the longitudinal thermal stress by subtracting, from the total longitudinal relieved stress, the longitudinal residual component that is, in turn, calculated from the vertical relieved stress (that only contains the residual component since the vertical direction undergoes free thermal expansion).

This chapter is organized as follows: Section 4.2 reviews the essentials of the hole-drilling strain-gage method and the basis for uncertainty analysis; Section 4.3 presents a finite element study of the application of the technique to thermal stress measurements and proposes new calibration coefficients for the especially-fine hole depth increments required by this application; Section 4.4 describes the experimental validation of the new calibration coefficients on a thick plate subjected to a known axial load; Section 4.5 presents the hole-drilling tests on 136RE and 141RE rail sections, including the characterization of the residual stress field used for compensation, and the estimation of the *in-situ* thermal stress levels (hence NT values) in constrained CWR at UCSD's Large-scale Rail CWR Ted-bed; Section 4.6 contains the discussion and conclusions.

4.2. Basics of the hole-drilling strain gage method

4.2.1 Essential theory

The most basic description consists of drilling a through-thickness hole in a thin linear elastic plate subjected to a uniform uniaxial stress along the *x* axis, $\sigma_x = \sigma$, as shown in Fig. 4.2. The stress distribution at point $P(R,\theta)$ around a circular hole in a prestressed plate was solved by Kirsch in the 1890s [26]:

$$\begin{cases} \sigma_r = \dfrac{\sigma}{2}\left(1-\dfrac{{R_0}^2}{R^2}\right)+\dfrac{\sigma}{2}\left(1+3\dfrac{{R_0}^4}{R^4}-4\dfrac{{R_0}^2}{R^2}\right)cos\,2\theta \\ \sigma_t = \dfrac{\sigma}{2}\left(1+\dfrac{{R_0}^2}{R^2}\right)-\dfrac{\sigma}{2}\left(1+3\dfrac{{R_0}^4}{R^4}\right)cos\,2\theta \\ \tau_{rt} = -\dfrac{\sigma}{2}\left(1-3\dfrac{{R_0}^4}{R^4}+2\dfrac{{R_0}^2}{R^2}\right)sin\,2\theta \end{cases} \tag{4.1}$$

where R_0 is the hole radius and *R* is the distance from the hole center.

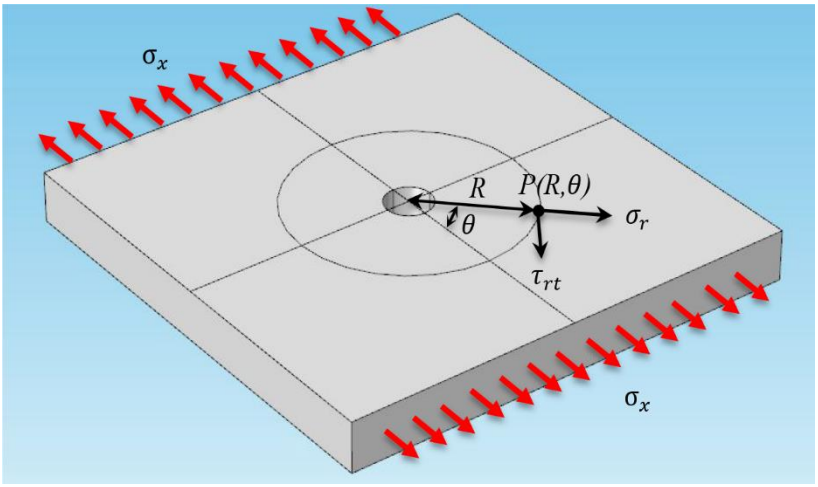

Figure 4.2 Thin plate under uniaxial uniform stress.

The stress relaxation caused by the material removal can be computed by subtracting the pre-drilled stress from the after-drilled stress. Since radially-oriented strain gages are typically used, of importance is the relieved radial strain [12]. Using Hooke's law with plane stress approximation, the relieved radial strains at point $P(R,\theta)$, can be computed as:

$$\varepsilon_r = \sigma(A + B\cos 2\theta) \tag{4.2}$$

where σ is the uniaxial stress, $A = \frac{1-\nu}{2E} + \frac{1+\nu}{2E}\frac{1}{r^2}$, $B = \frac{1+\nu}{2E}\left[1 + \frac{3}{r^4} - \frac{4}{r^2(1+\nu)}\right]$, $r = \frac{R}{R_0}$, and E and ν are the Young's modulus and Poisson's ratio of the plate material.

For the case of a biaxial stress state, the relieved radial strain can be computed as:

$$\varepsilon_r = A(\sigma_x + \sigma_y) + B(\sigma_x - \sigma_y)\cos 2\theta \tag{4.3}$$

where σ_x and σ_y are the stresses along the *x* and *y* directions.

For the more complex case of a blind-hole used in "thick" specimens (as it is the case for the rail application at hand), the relieved radial strain can be formally expressed by Eq. (4.3), with appropriate values for the calibration constants *A* and *B* (or $\bar{a}$ and $\bar{b}$ in most relevant literature) that are determined from experiments [14] and/or finite element models [15-18]. In typical finite element analysis, the constants $\bar{a}$ and $\bar{b}$ can be computed from a hydrostatic stress state ($\sigma_x = \sigma_y$) and a deviatoric stress state ($\sigma_x = -\sigma_y$), respectively. The superposition principle to simulate the strains relieved by the blind hole for a case of uniformly distributed stress along the thickness is schematized in Fig. 4.3 [15]: load case (a) represents the initial state, with corresponding stresses at the virtual hole boundary; load case (c) shows

the stress state after drilling, in which the normal and shear stresses along the hole boundaries vanish; load case (b) shows the stress redistribution due to drilling. By modeling load case (b), the deformation field captured by strain gage measurements can be obtained. Therefore, the relieved strains can be predicted by applying a virtual stress field at the hole boundaries that is opposite to the initial stress field, for both the hydrostatic and the deviatoric cases.

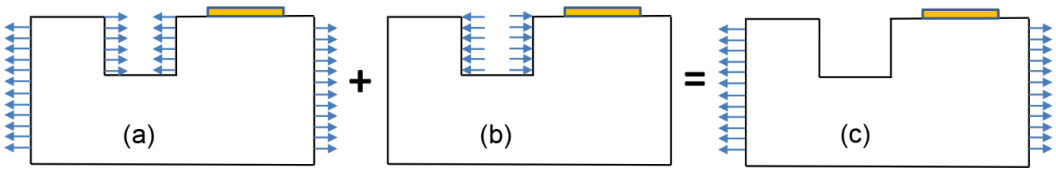

Figure 4.3 Superposition of stresses to find the strain relaxation due to blind hole drilling: (a) original stress state; (b) stress relaxation due to drilling; (c) final stress state [15].

4.2.2 Test implementation and uncertainty analysis

After appropriately cleaning the surface, standardized rosettes are applied with specific gage patterns and size depending on strain sensitivity and thermal stability requirements (e.g. Micro-Measurements type A, B or C [12]). For the case of uniform stress through the thickness, the stresses relaxed by drilling the hole are computed by weighted averages of strain recordings along the hole depth. The original ASTM standard [10] suggests to drill a blind hole with an 8-step procedure for a thick workpiece, defined as a test piece with a thickness larger than 1.2 times the rosette circle's diameter. A 10-step procedure is presented

in the 2013 edition of the ASTM standard [11]. The recorded strains from three strain gage elements at the i[th] depth increment, $(\varepsilon_{1i}, \varepsilon_{2i}, \varepsilon_{3i})$, are converted into combination strains as:

$$\mathrm{p}_i = \frac{\varepsilon_{3i} + \varepsilon_{1i}}{2};\ \mathrm{q}_i = \frac{\varepsilon_{3i} - \varepsilon_{1i}}{2};\ \mathrm{t}_i = \frac{\varepsilon_{3i} + \varepsilon_{1i} - 2\varepsilon_{2i}}{2} \tag{4.4}$$

The combination stresses *P*, *Q* and *T* are then computed through the weighted averages of the combination strains at all the depths as:

$$P = -\frac{E}{1+\nu}\frac{\sum_i \bar{a}_i p_i}{\sum_i \bar{a}_i^2}; \quad Q = -E\frac{\sum_i \bar{b}_i q_i}{\sum_i \bar{b}_i^2}; \quad T = -E\frac{\sum_i \bar{b}_i t_i}{\sum_i \bar{b}_i^2} \tag{4.5}$$

where $\bar{a}_i$ and $\bar{b}_i$ are the calibration coefficients for the *i*[th] hole depth increment. Averaging the various depth increments allows minimizing the effects of random strain measurement errors [19]. Given the combination stresses *P*, Q and *T*, the in-plane pre-drilling stresses are finally computed as:

$$\sigma_x = P - Q; \quad \sigma_y = P + Q; \quad \sigma_{xy} = T \tag{4.6}$$

An uncertainty analysis can be quite appropriate for this method. Errors in the estimation of the unknown stress field can arise from strain measurement errors, hole depth measurement errors, hole diameter measurement errors, material constant estimation errors and hole eccentricity errors, among others [87-89]. Considering a well-designed apparatus with an objective tracking function for drill positioning/diameter measurement and a precise control of drilling depth, the major source of uncertainty is the strain measurement error. This error can be induced by instrumentation inaccuracies, gage thermal outputs and possible plastic

deformation induced by the drilling process. The error of parameter $y = f(x_1, x_2 \ldots x_N)$ can be computed in terms of its variance, $u_c^2(y)$:

$$u_c^2(y) = \sum_{s=1}^{N} c_s^2 u^2\,(x_s) \tag{4.7}$$

where $u^2\,(x_s)$ is the variance of parameter x_s (the subscript "c" stands for "computed"), and c_s is the sensitivity of x_s correlating to y. Using Eqs. (4.5)-(4.8), the uncertainty of the uniformly distributed stresses resulting from strain measurement errors can be computed as:

$$u_c^2(\sigma_x) = u_c^2(\sigma_y) = u_c^2(P) + u_c^2(Q) = \left(\frac{E}{1+\nu}\right)^2 \left[\frac{1}{\sum_i \bar{a}_i^2} + \frac{(1+\nu)^2}{\sum_i \bar{b}_i^2}\right] \frac{u^2\,(\varepsilon)}{2} \tag{4.8}$$

where $u^2\,(\varepsilon)$ is the variance of the strain gage readings, that is assumed uniform for the various hole depths.

Other specific aspects of the hole-drilling method apply to the rail thermal stress application. First, it was found that the hardness of typical rail steel after the hot rolling treatment (over 260 HB for high carbon rail steel compared to 120 HB for mild steel [90]) requires finer drilling steps than what typically recommended to avoid over-abrasion of the drill bit and ensure a consistent hole diameter. The finer drilling steps required the computation of updated calibration coefficients using a 3-D finite element model (presented in Section 4.3), followed by an experimental validation (Section 4.4). Second, a stable platform was designed and manufactured to accommodate the specific requirements of mounting the drill on a rail track geometry (Section 4.4). In addition, special care had to be taken to

eliminate the residual stress component from the longitudinal relieved stress, to enable the estimation of the rail Neutral Temperature that is only determined by the thermal stress component (Section 4.5).

4.3. Finite element analysis

This section presents the Finite Element Analysis (FEA) carried out to simulate the hole-drilling procedure for the measurement of thermal stresses, including the computation of new calibration coefficients for the required finer hole depth increments.

4.3.1 Convergence study and feasibility investigation for in-situ thermal stress estimation

The mesh convergence study was conducted in 2D on a thin square plate with a though-thickness hole, modeled as a quarter owing to symmetry. The plate was subjected to a uniform uniaxial stress of -86.1 MPa (-12.49 ksi) along the *x* axis, which is a reasonable value of thermal stress level in CWR. The theoretical solution by Kirsch from Eq. (4.1) was used as the expected stress distribution. Fig. 4.4(a) presents the contour plot of the radial stress σ_r, with the corresponding numerical contour shown in Fig. 4.4(b). A closer look was taken by comparing the analytical (Kirsch) and FEM results of σ_r and τ_{rt} along an arc with a radius of 1.77 mm in Fig. 4.4(c) and 4.4(d), respectively, where this radius corresponds to the boundary of an M-M 062UL strain gage rosette [12]. The agreement between analytical and

FEM results is excellent, with σ_r varying according to $\cos 2\theta$ and τ_{rt} varying according to $\sin 2\theta$, as expected from Eq. (4.1).

A parametric study of mesh refinement was performed from Mesh 1 to Mesh 4 (with Mesh 1 the finest and Mesh 4 the coarsest) and the analytical results set as the reference. Considering the *x* axis and *y* axis as the center lines of the 1st and 3rd strain gage elements, respectively, the radial stress σ_r and radial strain ε_r along the lines $y = 0$ and $x = 0$ are shown in Fig. 4.5 for the various mesh sizes. In Fig. 4.5(a) and 4.5(b), the stresses σ_r from the finer Mesh 1 and Mesh 2 are well aligned with the theoretical results, while large discrepancies were observed in the coarser Mesh 3 and Mesh 4. In Fig.4.5(c) and 4.5(d), similar results were observed for the strains ε_r. Mesh 1 was therefore used as the final mesh for the subsequent simulations.

A two-step analysis based on a 3-D finite element model of a plate was conducted to simulate the hole-drilling implementation on a uniaxial thermal stress case, as applicable to CWR (neglecting the residual stress component for this simulation). In the first step, a temperature variation was applied to the plate constrained along the *x* axis (zero displacement at the boundary) and, instead, free to expand along the *y* axis as shown in Fig. 4.6(a). A temperature increment of 35°C (63°F) was applied to the model, with a corresponding theoretical compressive thermal stress of -86.1 MPa (or -12.49 ksi) for typical steel. In the second step, the thermal stress field from step 1 was applied to a plate with the same geometry

and boundary conditions, but with a blind hole at a specific depth in the center. To satisfy the traction-free conditions along the hole boundary, the stress field redistributed and led to a final displacement field different from the one of step 1. The deformation field corresponding to the strain gage area of step 2 was extracted and averaged to compute the strain gage readings at the specific hole depth, as shown in Fig. 4.6(b). This two-step analysis was repeated for 8 incremental hole depths. The stress relaxation computed from the calibration coefficients of the ASTM standard [10] was -86.7 MPa (-12.57 ksi), with an error as small as 0.7% from the known thermal stress value. This simple analysis showed promise for the applicability of the hole-drilling technique to the measurement of thermal stresses in CWR, once an appropriate residual stress compensation strategy is applied.

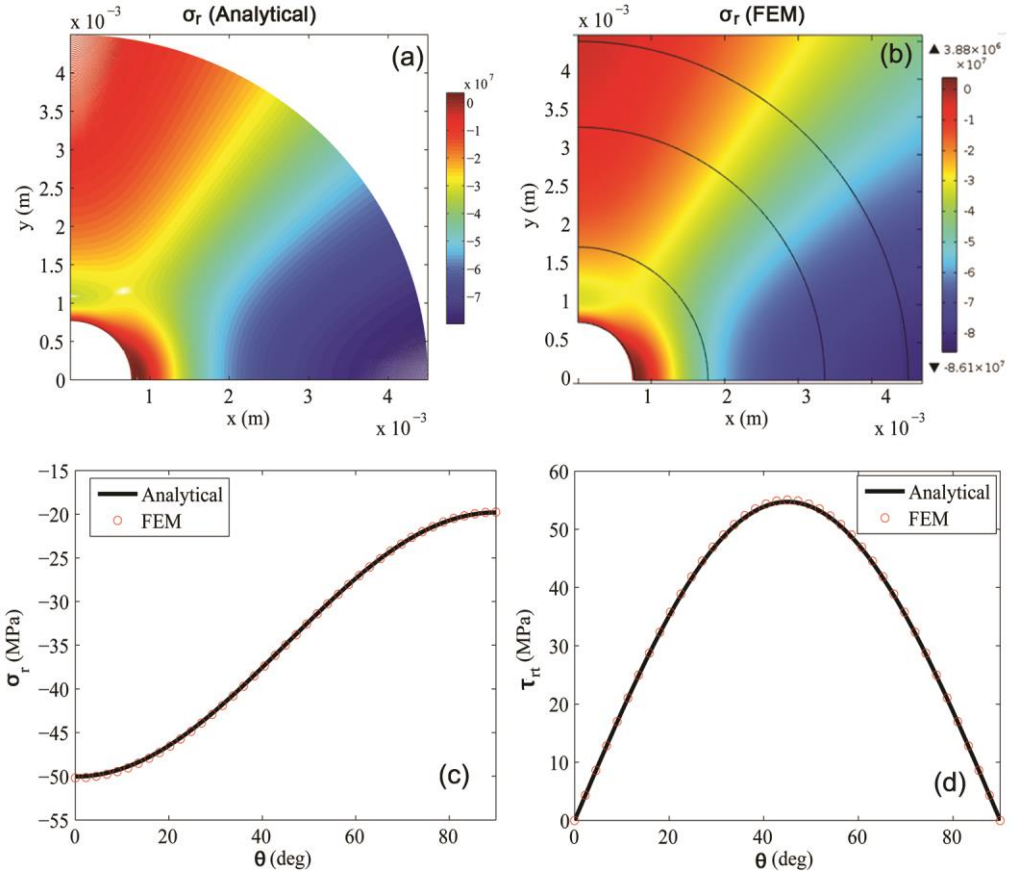

Figure 4.4 The stress field around a through hole in a plate: (a) analytical σ_r; (b) numerical σ_r. Stress distribution along the arc of the gage boundary: (c) analytical & numerical σ_r; (d) analytical & numerical τ_{rt}.

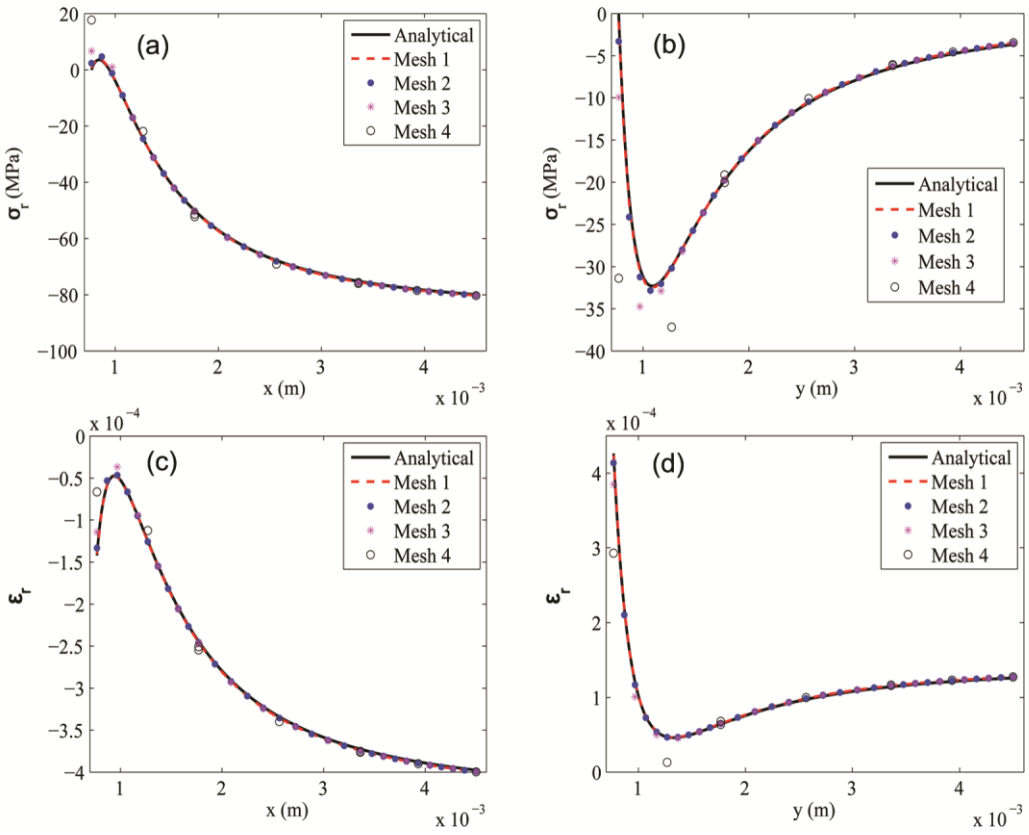

Figure 4.5 Mesh refinement results: (a) σ_r along the x axis; (b) σ_r along the y axis; (c) ε_r along the x axis; (d) ε_r along the y axis.

4.3.2 3D simulation to determine the calibration coefficients

Most commonly, the hole-drilling calibration coefficients are calculated from extracting relieved strains from 2D models that use the hypothesis of axisymmetric conditions, as shown in Fig. 4.3(b)) [15]. These 2D models, that form the basis of the ASTM standards [10, 11], utilize special elements that use Fourier series expansion in the circumferential direction. Previous computations based on 3D models [17, 18] mainly focused on non-uniform residual stress distributions that required the application of equivalent stresses solely to the

hole wall boundary, thereby neglecting the shear stresses at the hole bottom, that are expected to be small near a stress-free surface. In the present study, a differential analysis was conducted to compute the displacement field of the hole-drilling process in a rail application considering the full 3D case and the entirety of the hole boundary. Specifically, a plate with approximately the same thickness as the rail web under hydrostatic/deviatoric stress state was simulated at step 1; the plate with a blind hole at specific hole depth under the same load was modelled at step 2. By subtracting the strain field of step 1 from that of step 2, the relieved strains at the specific drilling step was computed. Considering the applied (known) stress state, the calibration coefficient $\bar{a}$ and $\bar{b}$ at the specific hole depth were finally determined. This procedure was repeated for 8 incremental hole depths and various ratios of hole diameter to gage circle diameter ($D0/D$). The new calibration coefficients calculated with this procedure are listed in Table 4.1. The percentage discrepancies compared to the ASTM standard are listed in Table 4.2. In general, for a fixed $D0/D$ ratio, the discrepancies decrease with increasing hole depths, with the most significant differences found at the first one or two drilling steps for all $D0/D$ ratios. That the discrepancies are more evident at shallow hole depths is expected, since the relieved surface strains are notoriously most sensitive to near-surface stresses, with the surface sensitivity rapidly decreasing with depth.

A further comparative study of the calibration coefficients was conducted between the proposed 3D model that considers the complete stress redistribution, ASTM standard E837-08,

and a more traditional 3D model that only considers the stress redistribution along the hole wall boundary. Fig. 4.7 shows the comparison for a $D0/D$ ratio of 0.3 for both coefficients $\bar{a}$ and $\bar{b}$. As seen in these plots, the coefficients from the new 3D model are generally found slightly larger than those from the other two sources.

The new FEA was then utilized to compute the coefficients with finer hole depth increments, as required by the application to the hard steel of CWR. A series of experimental drilling trials on the high hardness rail steel indicated that 20 steps with 0.05 mm increments (for the M-M 062UL rosette [12]) or 0.1 mm increments (for the M-M 125RE rosette [12]) provide satisfactory drilling smoothness and tolerable abrasion of the drill bit. Therefore, the 3-D FEA just described was utilized to determine the calibration coefficients for this test procedure. The model of the rail web, with the applicable boundary conditions, is shown in Fig. 4.8. A biaxial stress field was applied to simulate the residual stresses as shown in Fig. 4.8(a); the material removal process was simulated by eliminating layers of elements with thickness equal to the depth increment; the gage readings were computed as the difference between the averaged strains over the gage areas from the model with the hole and the strains from the pristine geometry, as shown in Fig. 4.8(b). Specifically, the Cartesian strain components along each of the gage lengthwise directions were averaged over the active area as specified by the ASTM standard. This process was repeated for the 20 successive increments and five $D0/D$ ratios. The computed calibration coefficients are listed in Table 4.3.

The uncertainties expected with different calibration coefficients were also investigated, assuming a strain gage reading error with a 3με standard deviation. Considering $D0/D$ ratios from 0.3 to 0.5, the stress prediction uncertainties due to strain reading errors were computed using Eq. (4.8), for (a) a through-hole analysis (computed as a 1-step procedure), (b) the 8-step ASTM procedure, and (c) the new 20-step procedure. The results are listed in Table 4. The results in this table indicate that a reasonable standard deviation of the measured stresses, based on a 3με strain measurement uncertainty, is 1.32 MPa (0.191 ksi). The results also indicate, as expected, that generally smaller uncertainties in the stress predictions can be achieved by increasing the hole diameter or the number of drilling steps. Therefore, besides addressing the hard rail steel condition, the finer depth increments help reducing stress prediction errors while removing less material compared to a traditional 8-step procedure (half the final hole depth compared with the ASTM 8-step procedure).

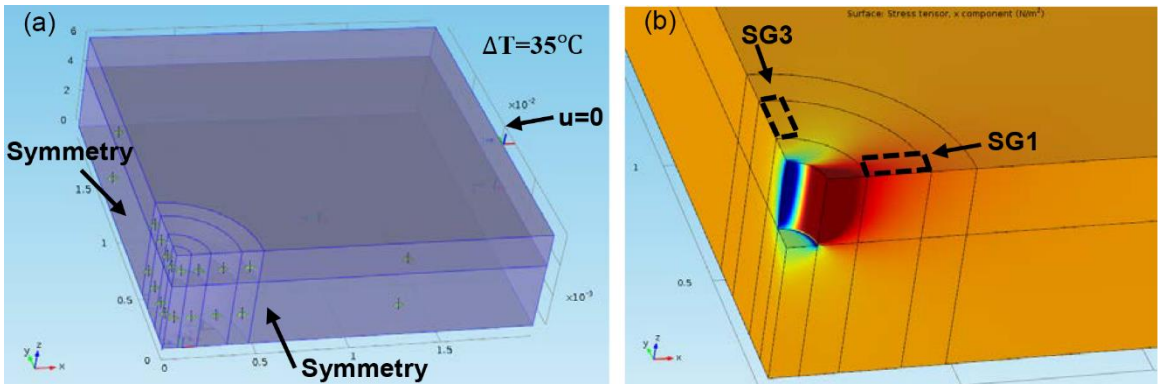

Figure 4.6 (a) The boundary condition setup in the analysis step 1. (b) σ_x at the 8th (final) hole depth increment in the analysis step 2.

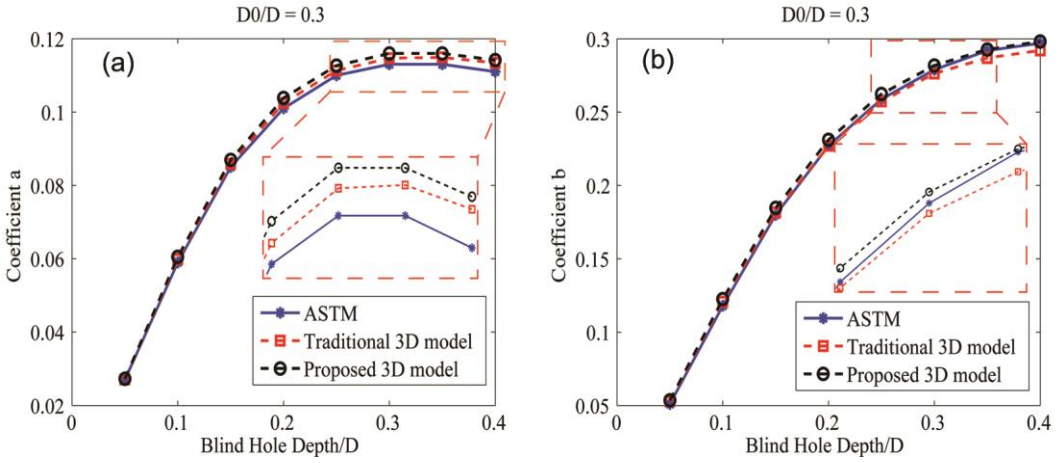

Figure 4.7 The calibration coefficients from the ASTM standard, the traditional FE 3D model and the proposed FE 3D model for the 8-step drilling procedure: (a) coefficient $\bar{a}$ and (b) coefficient $\bar{b}$ for a hole diameter/gage circle diameter ratio of 0.3.

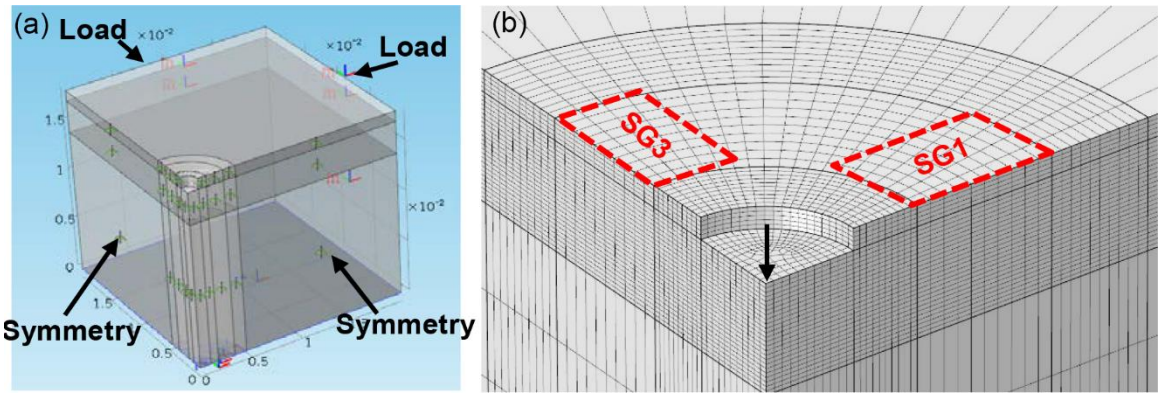

Figure 4.8 (a) Boundary conditions for the calibration coefficients of the 20-step procedure. (b) Mesh configuration at the 4th hole depth increment.

Table 4.1 The calibration coefficients computed from the proposed finite element models, where $D0$ is the hole diameter and D is the diameter of the gage circle.

Blind Hole	$\bar{a}$					$\bar{b}$				
	Hole Diameter D0/D					**Hole Diameter D0/D**				
Depth/D	**0.3**	**0.35**	**0.4**	**0.45**	**0.5**	**0.3**	**0.35**	**0.4**	**0.45**	**0.5**
0.05	0.0272	0.0375	0.0504	0.0668	0.0882	0.0535	0.0721	0.0944	0.1213	0.1545
0.1	0.0605	0.0829	0.1102	0.1434	0.1837	0.1226	0.164	0.2122	0.2679	0.3316
0.15	0.087	0.1183	0.1553	0.1981	0.2468	0.1846	0.2449	0.3126	0.3868	0.4659
0.2	0.1038	0.1403	0.1822	0.2291	0.2806	0.2312	0.3044	0.3841	0.4682	0.5536
0.25	0.1127	0.1515	0.1953	0.2437	0.2959	0.2625	0.3438	0.4304	0.5195	0.6073
0.3	0.116	0.1555	0.1999	0.2484	0.3005	0.2819	0.3679	0.4584	0.550	0.6387
0.35	0.116	0.1554	0.1995	0.2478	0.2995	0.2928	0.3815	0.4741	0.567	0.6559
0.4	0.1142	0.1531	0.1967	0.2445	0.2959	0.2982	0.3883	0.4821	0.5755	0.6644

Table 4.2 The relative percentage discrepancies between the calibration coefficients computed by the proposed finite element model ($\bar{a}_{FEA}$ and $\bar{b}_{FEA}$) and those in ASTM standard E837-08 ($\bar{a}_{ASTM}$ and $\bar{b}_{ASTM}$) [10].

Blind Hole	$\frac{\bar{a}_{FEA}-\bar{a}_{ASTM}}{\bar{a}_{ASTM}}\times 100\%$					$\frac{\bar{b}_{FEA}-\bar{b}_{ASTM}}{\bar{b}_{ASTM}}\times 100\%$				
	Hole Diameter D0/D					**Hole Diameter D0/D**				
Depth/D	**0.3**	**0.35**	**0.4**	**0.45**	**0.5**	**0.3**	**0.35**	**0.4**	**0.45**	**0.5**
0.05	4.11	4.54	6.02	9.30	13.64	8.27	7.83	8.21	10.75	13.81
0.1	5.22	5.02	4.64	6.45	6.70	6.86	6.06	5.85	7.83	7.20
0.15	4.25	4.81	4.64	4.83	5.17	4.93	4.77	4.67	5.19	4.69
0.2	4.05	3.59	4.00	3.70	3.63	3.59	3.48	3.46	3.45	2.86
0.25	3.04	3.63	3.32	2.82	3.10	2.56	2.55	2.34	2.24	1.57
0.3	2.78	3.13	2.59	2.29	2.60	1.81	1.81	1.65	1.35	0.65
0.35	2.42	2.73	2.13	2.19	2.40	0.73	1.10	0.86	0.54	0.15
0.4	2.41	2.34	2.06	1.92	2.05	0.61	0.56	0.21	0.09	-0.39

Table 4.3 The calibration coefficients for 20-step uniform stress determination where $D0$ is the hole diameter and D is the diameter of the gage circle.

Blind Hole Depth/ D	$\bar{a}$					$\bar{b}$				
	Hole Diameter D0/D					**Hole Diameter D0/D**				
	0.3	**0.35**	**0.4**	**0.45**	**0.5**	**0.3**	**0.35**	**0.4**	**0.45**	**0.5**
0.01	0.0036	0.0051	0.0068	0.0091	0.0121	0.0075	0.0102	0.0134	0.0173	0.0220
0.02	0.0084	0.0116	0.0156	0.0207	0.0275	0.0167	0.0227	0.0298	0.0384	0.0490
0.03	0.0139	0.0191	0.0257	0.0341	0.0451	0.0274	0.0370	0.0485	0.0624	0.0797
0.04	0.0199	0.0274	0.0368	0.0487	0.0642	0.0390	0.0526	0.0689	0.0886	0.1130
0.05	0.0263	0.0361	0.0484	0.0640	0.0841	0.0515	0.0693	0.0907	0.1164	0.1479
0.06	0.0329	0.0451	0.0604	0.0795	0.1041	0.0645	0.0867	0.1132	0.1450	0.1836
0.07	0.0395	0.0541	0.0723	0.0950	0.1238	0.0778	0.1045	0.1362	0.1739	0.2193
0.08	0.0460	0.0631	0.0841	0.1102	0.1427	0.0913	0.1225	0.1593	0.2028	0.2543
0.09	0.0524	0.0718	0.0955	0.1247	0.1605	0.1048	0.1404	0.1822	0.2311	0.2882
0.1	0.0585	0.0802	0.1064	0.1384	0.1772	0.1181	0.1580	0.2046	0.2585	0.3206
0.11	0.0644	0.0881	0.1168	0.1512	0.1925	0.1311	0.1752	0.2262	0.2848	0.3513
0.12	0.0700	0.0956	0.1264	0.1631	0.2064	0.1438	0.1918	0.2470	0.3098	0.3800
0.13	0.0752	0.1026	0.1353	0.1739	0.2190	0.1559	0.2077	0.2668	0.3334	0.4069

Table 4.3 The calibration coefficients for 20-step uniform stress determination where $D0$ is the hole diameter and D is the diameter of the gage circle, continued.

0.14	0.0800	0.1091	0.1435	0.1838	0.2303	0.1675	0.2228	0.2856	0.3555	0.4317
0.15	0.0845	0.1150	0.1509	0.1927	0.2403	0.1786	0.2372	0.3032	0.3761	0.4547
0.16	0.0886	0.1204	0.1577	0.2006	0.2492	0.1890	0.2507	0.3197	0.3952	0.4758
0.17	0.0923	0.1253	0.1637	0.2076	0.2570	0.1988	0.2633	0.3350	0.4129	0.4951
0.18	0.0957	0.1297	0.1690	0.2138	0.2638	0.2080	0.2751	0.3492	0.4292	0.5127
0.19	0.0987	0.1335	0.1738	0.2193	0.2697	0.2166	0.2860	0.3624	0.4441	0.5288
0.2	0.1013	0.1370	0.1779	0.2240	0.2747	0.2245	0.2961	0.3745	0.4578	0.5435

Table 4.4 Expected standard deviation of σ_{Rx} and σ_{Ry} measurements in MPa due to strain measurement errors.

Blind Hole Depth/D	**Hole Diameter D0/D**				
	0.3	**0.35**	**0.4**	**0.45**	**0.5**
Through Hole ASTM	3.95	2.93	2.25	1.79	1.48
8-Step ASTM	1.4	1.05	0.81	0.66	0.54
20-Step procedure	1.32	0.97	074	0.59	0.48

4.4. Experimental validation of strain relaxation coefficients in uniaxial load test

The updated calibration coefficients for the 20-step test procedure calculated from the FEA of Section 3 were experimentally validated in a simple test involving a uniaxial tensile load applied to a thick aluminum plate in an MTS machine and instrumented with M-M 125RE residual stress rosettes [12]. The hole-drilling assembly featured a Vishay Measurements drill with micro-meter controlled position. The experimental setup is shown in Fig. 4.9(a). The geometry of specimen was 610 mm (24 in) in length, 89 mm (3.5 in) in width, and 12.7 mm (0.5 in) in thickness, qualifying it as a "thick" specimen for the given hole-drilling gage circle. The Young's modulus was determined as $E = 70.3$ GPa (10.2e6 psi) from a tensile test, and the Poisson's ratio was assumed as $\nu = 0.32$. The small bending moment arising from the grip misalignments was isolated by four symmetrically installed strain gages, and the linearly varying stress distributions through the thickness was approximated as uniform by averaging the stresses along the drilling depths.

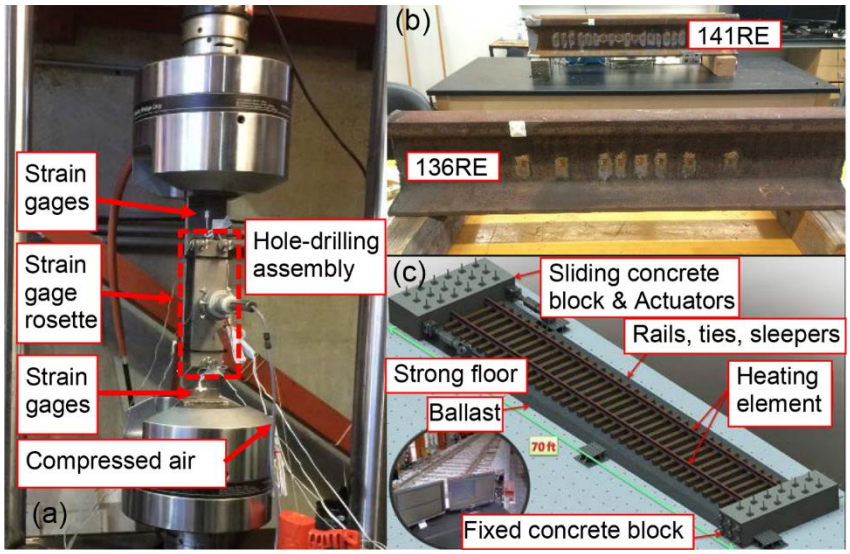

Figure 4.9 Experimental setups for: (a) uniaxial tensile load on the thick aluminum plate using the MTS machine; (b) test 1 on unconstrained 136RE rail section (residual stress characterization); (c) test 2 on constrained CWR under controlled thermal loads at UCSD's Large-scale CWR Test-bed.

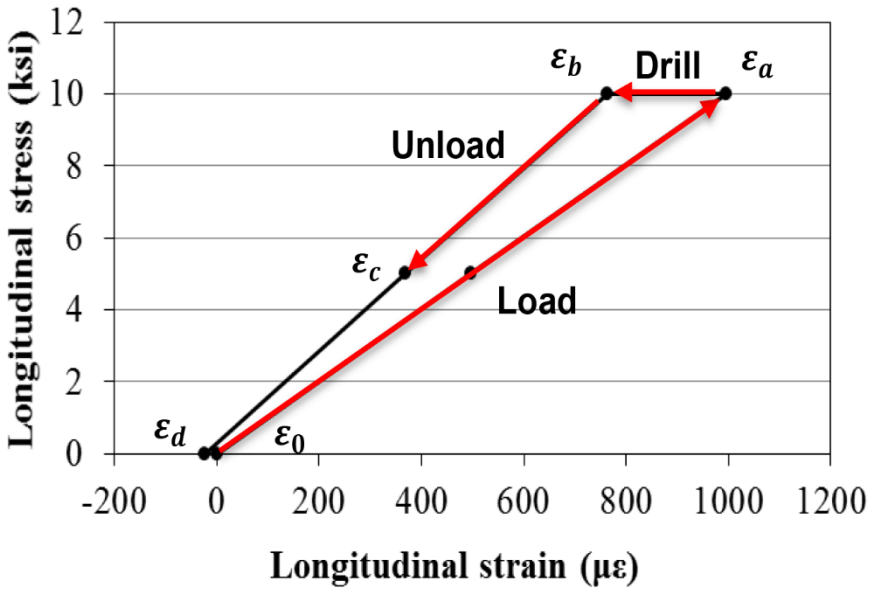

Figure 4.10 Experimental validation of the 20-step calibration coefficients in the thick aluminum plate subjected to known axial load: strain readings from the longitudinal strain gage element at the 10th hole drilling step.

In order to properly validate the hole-drilling measurements, it was important to take into account the presence of residual stresses in the specimen. To eliminate the existing residual stress, a compensation method developed by Rendler and Vigness [14] was applied. This compensation method requires knowledge of a state of zero applied stress, which was available in this proof-of-principle test. In the application to thermal stress measurements in CWR, instead, the zero thermal stress state (Neutral Temperature) is not known, and hence a compensation procedure for the residual stress component has to be devised, as discussed later in Section 4.5. The procedure to separate the effects of the residual stresses from those of the applied stresses is schematized in Fig. 4.10 using strain gage element 1 reading at the 10th hole drilling step as an example: the plate was first loaded to a stress level of 68.9 MPa (10 ksi); the hole was drilled at a depth increment, and a strain relief of $\Delta\epsilon_T = \epsilon_a - \epsilon_b$ was measured; the specimen was then unloaded to a stress level of 34.37 MPa (5 ksi), and the strain ϵ_c was measured; extrapolation of the new curve to zero stress state provided a value of strain ϵ_d, which was different from the original strain ϵ_0 at zero stress state before drilling. The difference $\Delta\epsilon_R = \epsilon_0 - \epsilon_d$ can be therefore attributed to the residual stress in the specimen at the given drilling depth. Finally, $\Delta\epsilon = \Delta\epsilon_T - \Delta\epsilon_R$ is the strain caused by the applied uniaxial load corrected for the residual component. This loading-unloading procedure was repeated for 20 hole depths until the final hole depth was attained. The stress computation was carried out using the updated 20-step calibration coefficients identified in the previous section. For the test

at 103.42 MPa (15 ksi) nominal tensile stress, with an estimated 5.24 MPa (0.76 ksi) compressive stress due to the spurious bending moment (i.e. expected net tensile stress of 98.18 MPa or 14.24 ksi), the measured tensile stress was 90.05 MPa (13.06 ksi). For an expected net tensile stress of 61.98 MPa (8.99 ksi) (68.9 MPa or 10 ksi nominal tension with 6.96 MPa or 1.01 ksi compression from spurious bending), the measured result was 56.88 MPa (8.25 ksi). These measurements therefore yielded stress values within 10% of the expected applied stress. In turn, this suggests that the 20-step hole-drilling method has the potential to provide *in-situ* thermal stress values in CWR with an accuracy that is acceptable considering the industry standard of ±2.78 °C (±5 °F) Neutral Temperature estimation.

4.5. Experimental tests of rails

This section discusses the hole-drilling tests conducted on rail sections, including a first set of tests aimed at characterizing the residual stress field in 136RE and 141RE rail sizes for compensation purposes, and a second set of tests aimed at estimating the *in-situ* thermal stresses -hence the rail Neutral Temperature from Eq. (4.1) in constrained 136RE and 141RE CWR subjected to controlled thermal loads at UCSD's Large-scale CWR Test-bed.

4.5.1 Experimental procedure

The next effort of this study consisted of the design and construction of a prototype to implement the hole-drilling test in the web of a rail section as shown in Fig. 4.11. The drilling

assembly sat on a fixed horizontal platform and was pressed by a customized fixture against the rail web, which stabilized the assembly and minimized vibrations induced during the drilling process. The hole is drilled at the rail Neutral Axis (N.A.). The standard hole-drilling technique for "thick" specimens is followed, only with a 20-step procedure and the updated calibration coefficients.

Tests were conducted using on 136RE and 141RE rail sizes, which are utilized in the UCSD's Large-scale CWR Test-bed, shown in Fig. 4.9(c), a unique facility that allows to impose controlled thermal loads on a full rail track. The temperature-compensated full-bridge strain gage nodes on the rail track provide the true current value of the longitudinal thermal stress (hence the rail NT). These values were used to compare the results from the hole-drilling technique.

Two sets of tests (Test 1 and Test 2) were conducted on rails following the customized 20-step drilling procedure discussed in Section 4.3 and utilizing both of the M-M 062UL and M-M 125RE hole-drilling rosettes [12]. The purpose of Test 1 was to establish a (linear) relationship between the longitudinal residual stress, σ_{Rx}, and the vertical residual stress, σ_{Ry}, at the N.A. of unconstrained 136RE and 141RE rail sections -Fig. 4.9(b). The linear relationship that was also utilized by previous studies on magneto-elastic methods for rail NT estimation [28] was indeed established for both rail sizes with statistical confidence. In Test 2, the hole-drilling procedure was applied at 10 locations of the CWR rails in the Large-scale

Testbed where residual and thermal stresses co-existed - Fig. 4.9(c). The longitudinal residual stress component (determined from the measured vertical stress component –containing the residual portion only - through the linear relationship determined in Test 1) was subtracted from the total longitudinal stress to isolate the longitudinal thermal stress. The thermal stress was then used to estimate the rail Neutral Temperature from Eq. (4.1). The NT values estimated from this hole-drilling procedure were compared to the "true" NT values indicated by the previously-zeroed temperature-compensated strain gages, considering the statistical confidence of the residual stress compensation.

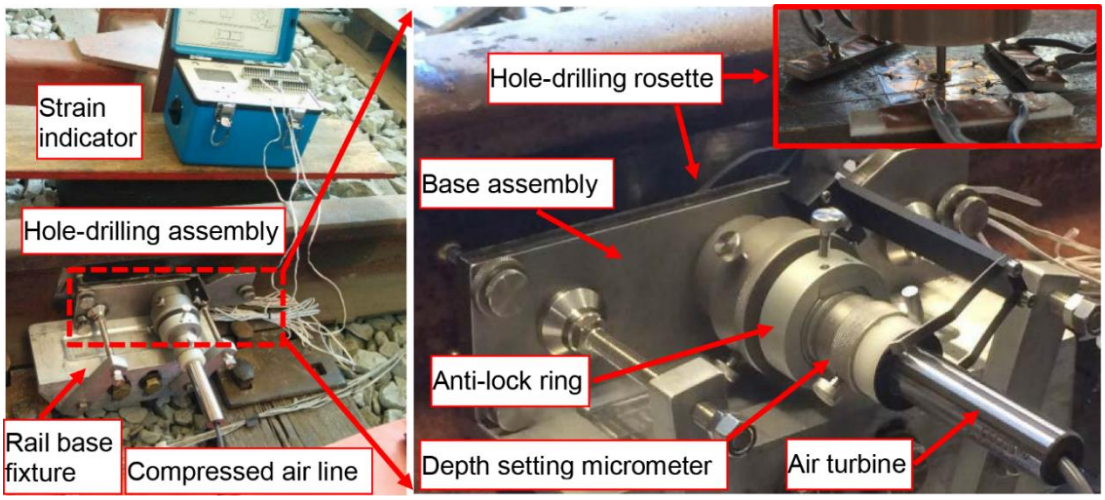

Figure 4.11 Experimental setup for the implementation of the hole-drilling method in the web of CWR.

4.5.2 Experimental results

4.5.2.1 Stress uniformity approximation validation

Considering the small final depth of the hole (2 mm or 0.08 in for the M-M 125RE rosette) and available information from prior studies of rail stresses [91], the residual stress distribution was assumed uniformly distributed along the hole depth. This assumption was validated for the Test 1 measurements of the 136RE rail section and the 141RE rail section, by comparing the measured combination strains to the "theoretical" relieved strains calculated using Hooke's law and the measured stresses. The "uniform" stress assumption through the thickness would be reasonable if the Root Mean Squared (RMS) error between the measured relieved strains and the theoretical relieved strains is comparable to the expected uncertainty of the strain gage outputs (set at 3με in this paper). This check is shown in Fig. 4.12(a) for the 136RE rail size, and in Fig. 4.12(b) for the 141RE rail size, where the measured combination strains p and q are plotted against the theoretical strains resulting from a uniform stress assumption [10]. The match is quite close, with relative deviations within 5%. Furthermore, RMS errors within the 3με range were observed for most measurements. Hence it was concluded that the assumption of uniform stress distribution along the hole depth was reasonable for the case at hand.

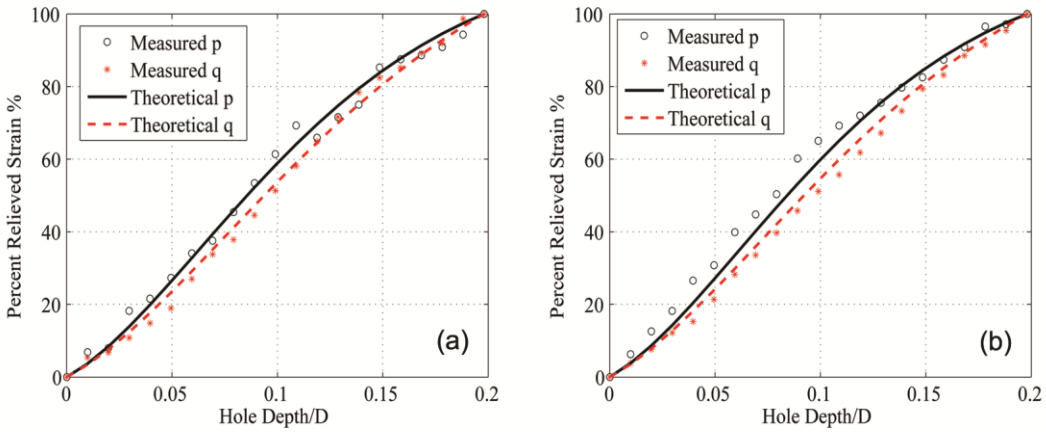

Figure 4.12 Stress uniformity check based on combination strains at the Neutral Axis of (a) the 136RE rail section, and (b) the 141RE rail section.

4.5.2.2 Data analysis for Test 1 – residual stress alone

The statistics of the residual stress distribution at the 136RE and 141RE rail N.A. were established in these tests. Plots of the longitudinal residual stress (σ_{Rx}) versus the vertical residual stress (σ_{Ry}) are shown in Fig. 4.13(a) and 4.13(b).

First, the following normal error regression model was applied to the data [92]:

$$\sigma_{Rx} = \beta_0 + \beta_1 \sigma_{Ry} + r \tag{4.9}$$

where the predictor variable was defined as the vertical stress, σ_{Ry}, the response variable was defined as the longitudinal stresses, σ_{Rx}, and r is the random error term with normal distribution. Given the constant levels of σ_{Ry}, the estimation of longitudinal residual stress can be expressed as $E\{\sigma_{Rx}\} = \hat{\beta}_0 + \hat{\beta}_1 \sigma_{Ry}$, where $\hat{\beta}_0 = -10.951$ and $\hat{\beta}_1 = 0.708$ for the 136RE rail section, and $\hat{\beta}_0 = -4.3353$ and $\hat{\beta}_1 = 2.1877$ for the 141RE rail section. The

estimated regression models relating σ_{Rx} to σ_{Ry} were plotted in Fig. 4.13(a) and 4.13(b) as solid lines for the two rail sizes.

The next step is to establish the statistical significance of this relationship. It can be proved that $\frac{\hat{\beta}_1-\beta_1}{s(\hat{\beta}_1)}$ is distributed as t_{n-2} (t distribution with n-2 degrees of freedom) for the regression model, where $s(\hat{\beta}_1) = \sqrt{\frac{MSE}{\sum_i (\sigma_{Ryi}-\bar{\sigma}_{Ry})^2}}$ and MSE is the Mean Square Error. Therefore, the test can be set up in an ordinary fashion using the t distribution. A two-sided test was conducted to check whether or not there is a linear relationship between σ_{Ry} and σ_{Rx}. The two alternatives are:

$$H_0: \beta_1 = 0; H_1: \beta_1 \neq 0 \tag{4.10}$$

To limit the risk of a Type I error with a 5% rate of false positives ($\alpha = 0.05$), an explicit test of the alternatives based on the test statistic of $t^* = \frac{\hat{\beta}_1}{s(\hat{\beta}_1)}$ was conducted. The null hypothesis was rejected since $|t^*| > t_{n-2}\left(1-\frac{\alpha}{2}\right)$. It can be concluded that there is a linear statistical relationship between σ_{Rx} and σ_{Ry}, with a 5% rate of false positives.

The final statistical analysis is to estimate the pointwise confidence intervals for the mean response. The dashed lines in Fig. 4.13 therefore indicate the 90% confidence range expected for the mean of the estimated σ_{Rx} for a given level of σ_{Ry}. In this respect, it can be proved that $\frac{\hat{\sigma}_{Rxi}-E\{\sigma_{Rxi}\}}{s(\hat{\sigma}_{Rxi})}$ is distributed as t_{n-2}, where $\hat{\sigma}_{Rxi}$ is the point estimator, $E\{\sigma_{Rxi}\}$ is the mean response corresponding to σ_{Ryi}, and $s(\hat{\sigma}_{Rxi}) = \sqrt{MSE\left(\frac{1}{n}+\frac{(\sigma_{Ryi}-\bar{\sigma}_{Ry})^2}{\sum_j (\sigma_{Ryj}-\bar{\sigma}_{Ry})^2}\right)}$. The (1- α)% confidence limits can be computed as $\hat{Y}_h \pm t_{n-2}\left(\frac{\alpha}{2}\right) * s(\hat{Y}_h)$, where the 90%

confidence pointwise confidence intervals are shown in Fig. 4.13(a) and 4.13(b) by the dashed lines. These figures show that, as expected, the confidence intervals are wider for σ_{Ry} measurements that are far from the mean $\overline{\sigma}_{\mathrm{Ry}}$ of the observations.

Based on this discussion, it is now of interest determining the confidence interval that can be expected in the estimation of the Neutral Temperature (*NT*) of a constrained rail subjected to thermal forces. In this case, the hole drilling method would directly measure the total longitudinal stress, σ_x, and the vertical residual stress, σ_{Ry}. From the latter, the longitudinal residual stress, σ_{Rx} , can be estimated, and then subtracted from σ_x to isolate the thermal component $\sigma_{\Delta T} = (\sigma_x\text{-}\sigma_{Rx})$. The current rail temperature, *T*, can of course be readily measured. The rail *NT* can be finally estimated from these parameters, after a simple manipulation of Eq. (1.17):

$$NT = T + \frac{\sigma_{\Delta T}}{E\alpha} = T + \frac{\sigma_x}{E\alpha} - \frac{b_1\sigma_{Ry} + b_0}{E\alpha} \tag{4.11}$$

Grouping the first two terms in the right-hand side of this equation in a constant $C = T + \frac{\sigma_x}{E\alpha}$, the uncertainty in rail *NT* estimation caused by the uncertainty in the residual stress compensation can be viewed by plotting the term (*NT* - *C*) versus the vertical residual stress σ_{Ry}. The results are shown in Fig. 4.14(a) and 4.14(b) for the 136RE constrained rail and the 141RE constrained rail, respectively, in terms of measurements from Test 1, regression model and 90% pointwise confidence interval. For a given vertical residual stress level, the corresponding widths of the 90% confidence interval are shown in Fig. 4.14(c) and 4.14(d) for

the 136RE and 141RE rails, respectively, along with the desired industry standard of 5.56℃ or ±2.78℃ (10 °F or ±5 °F) interval for *NT* determination. These figures indicate that the 90% pointwise confidence intervals will indeed satisfy the industry standards σ_{Ry} ranges from -84.8 MPa (-12.3 ksi) to 10.3 MPa (1.5 ksi) for the 136RE rail Test 1, and from -63.4 MPa (-9.2 ksi) to -28.9 MPa (-4.2 ksi) for the 141RE. These ranges correspond to σ_{Ry} values close to the mean of the measurements, where the regression model is more accurate.

4.5.2.3 Data analysis for Test 2 – residual stress plus thermal stress

The final set of experiments involved hole-drilling in the constrained rail sections to estimate current rail *NT* values by the procedure explained above. Tables 4.5 and 4.6 summarize the results obtained at five different locations of, respectively, the 136RE rail and the 141RE rail in the Large-scale CWR Test-bed. The five locations on each rail were spaced at least 8 cm (3.15 in) from one another. Specifically, the tables compare the estimated longitudinal thermal stress $\sigma_{\Delta T} = (\sigma_x\text{-}\sigma_{Rx})$ to the "ground truth" thermal stress indicated by the temperature-compensated full Wheatstone bridge strain gage installation closest to each drilling location. The tables also list the final estimated *NT* values, compared to the "ground truth" *NT* value from the Wheatstone bridges. The last column show the final error in *NT* estimation.

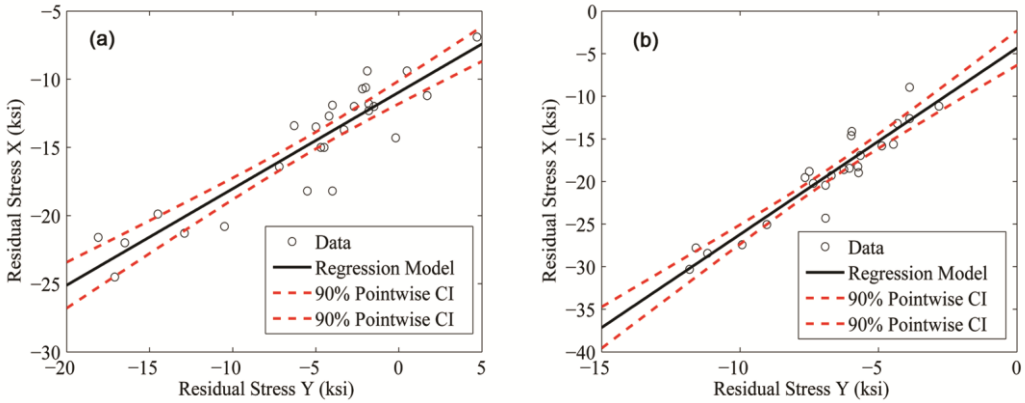

Figure 4.13 Regression model between the longitudinal and the vertical residual stress components at the Neutral Axis of (a) the 136RE rail section, and (b) the 141RE rail section.

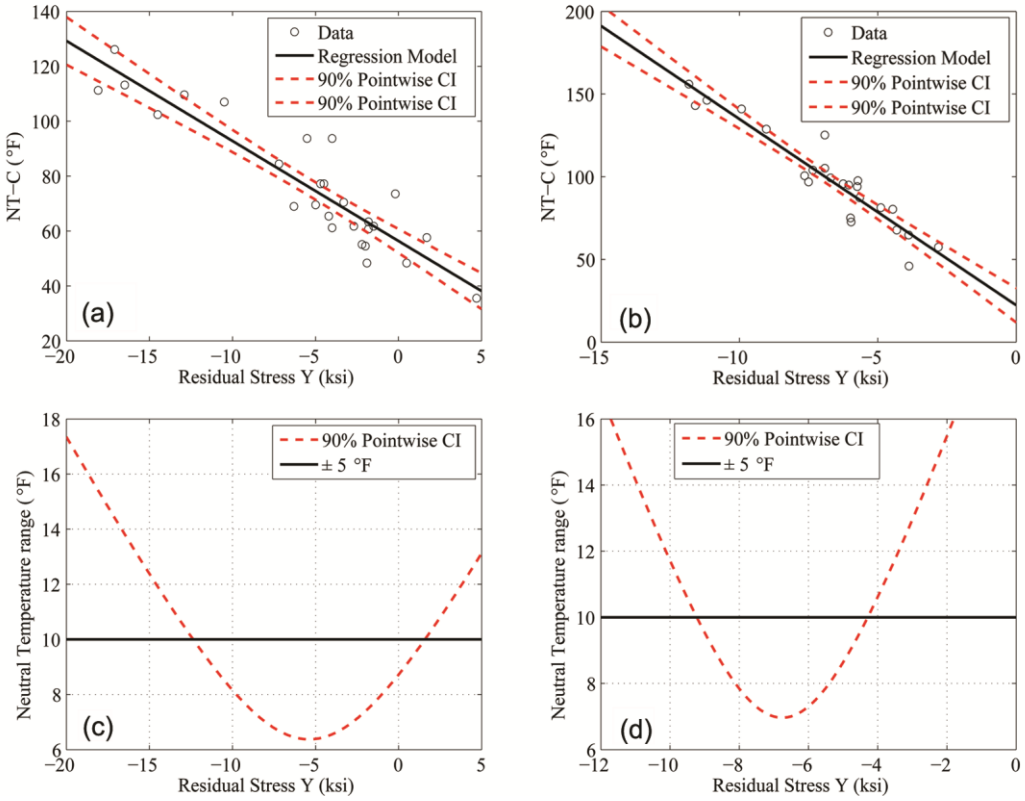

Figure 4.14 Expected uncertainty in NT estimation from the uncertainty in residual stress compensation. (NT-C) versus vertical residual stress for (a) the unconstrained 136RE rail section and (b) the unconstrained 141RE rail section. Width of the 90% pointwise confidence interval for NT estimation from (c) the 136RE rail section and (d) the 141RE rail section

Table 4.5 The hole-drilling test results from the constrained 136RE rail in the Large-scale CWR Test-bed. $\hat{\sigma}_{\Delta T}$ and $\widehat{NT}$ represent estimated values.

	Current rail temperature T	**Measured vertical stress (residual alone) σ_{Ry}**	**Estimated thermal stress $\sigma_{\Delta T}$**	**"Ground truth" thermal stress $\sigma_{\Delta T}$**	**Error thermal stress $\sigma_{\Delta T} - \hat{\sigma}_{\Delta T}$**	**Estimated Neutral Temperature**	**Error Neutral Temperature $NT - \widehat{NT}$**
	℃	MPa	MPa	MPa	MPa	℃	℃
pos1	25.4	-21.37	73.02	64.6	8.41	57.6	3.7
pos2	45	-24.13	-3.65	-8	4.34	43.4	1.9
pos3	26.4	-38.61	65.78	62.19	3.59	55.4	1.6
pos4	25.4	-79.98	67.91	62.81	5.1	55.3	2.3
pos5	26.9	-52.4	59.57	60.6	-1.03	53.2	-0.5

Table 4.6 The hole-drilling test results from the constrained 141RE rail in the Large-scale CWR Test-bed. $\hat{\sigma}_{\Delta T}$ and $\widehat{NT}$ represent estimated values.

	Current rail temperature T	**Measured vertical stress (residual alone) σ_{Ry}**	**Estimated thermal stress $\sigma_{\Delta T}$**	**"Ground truth" thermal stress $\sigma_{\Delta T}$**	**Error thermal stress $\sigma_{\Delta T} - \hat{\sigma}_{\Delta T}$**	**Estimated Neutral Temperature**	**Error Neutral Temperature $NT - \widehat{NT}$**
	℃	MPa	MPa	MPa	MPa	℃	℃
pos1	25.1	-55.92	50.06	42.33	7.72	47.2	3.3
pos2	25.7	-65.02	37.65	42.95	-5.31	42.3	-1.6
pos3	25.7	-53.37	30.47	35.85	-5.38	39.1	-2.6
pos4	26.4	-54.12	25.99	35.65	-9.65	37.9	-3.8
pos5	26.4	-54.95	40.47	35.65	4.83	44.3	2.6

For the 136 RE rail, the thermal stress measurement errors ranged from -1.03 MPa (-0.15 ksi) to 8.4 MPa (1.22 ksi), translating into *NT* estimation errors between -0.5℃ (-0.8°F) and 3.7℃ (6.7°F). For the 141RE rail, the thermal stress errors ranged from -9.7 MPa (-1.40 ksi) to 7.7 MPa (1.11 ksi), corresponding to *NT* estimation errors between -3.8℃ (-6.9°F) and 3.3℃ (5.9°F). The values of the vertical residual stress components, also shown in the second column of Tables 5 and 6, lie in the favourable range identified previously in Figs. 4.14(c) and 4.14(d), and hence the *NT* predictions could be indeed expected within the industry standard of ±2.78℃ (±5°F). These results therefore show the potential for the proposed hole-drilling technique to provide *in-situ* rail *NT* measurements with an acceptable level of accuracy.

4.6. Discussion and conclusions

In this chapter, an investigation was conducted to examine the applicability of the hole-drilling method to estimate the in-situ longitudinal thermal stresses in CWR, and therefore the rail Neutral Temperature. This information is badly needed by the railroad industry to conduct appropriate rail maintenance and prevent derailments caused by rail buckling in hot weather and broken rail in cold weather.

A series of FEAs were first conducted to compute the updated calibration coefficients for the finer hole depth increments required by drilling in the hard rail steel so as to avoid plastic deformations and drill bit erosion. The FEA mesh configuration was first established by

a convergence study that compared the numerical results with closed-form solutions for a through-hole case in a thin plate. Subsequently, The feasibility of using the hole-drilling method for thermal stress measurements was validated by comparing the applied thermal stress with the stress relaxation obtained numerically from a 2-step nonlinear FEA, that projected the thermal stress field from a constrained intact geometry to a constrained geometry with a blind hole. In order to compute the calibration coefficients with the finer depth increments, a 3-D FEA that accounted for traction terms at the entirety of the hole boundaries (hole wall and bottom) was conducted, and the results were compared with the applicable ASTM standard and with a more simplified 3-D FEA that only considered the hole wall. The discrepancies between these sets of coefficients were found to decrease with increasing hole depth, as a result of the smaller sensitivity of the surface strains to stress released at depth. Besides the different analysis, a possible other cause of discrepancy is the specific way that surface strains were averaged over the strain gage area. The new updated set of calibration coefficients from the 3D FEA was experimentally validated on a thick aluminum plate subjected to a uniaxial uniform tensile load in an MTS machine.

Two sets of hole-drilling experiments were then conducted on free 136RE and 141RE rail sections containing only residual stresses (Test 1), and on constrained rail sections subjected to thermal excursions producing added thermal stresses at UCSD's Large-scale CWR Test-bed (Test 2). The purpose of Test 1 was to build up the statistics of the residual

stress profile at the rail N.A., and specifically the linear relationship between the longitudinal and the vertical residual stress components. This linear relationship was statistically interpreted and tested with a two-sided test with the goal of a 90% confidence interval. The results from Test 1 were then utilized in Test 2, where the longitudinal residual stress component was subtracted from the total (residual + thermal) longitudinal stress relieved by hole-drilling. The hole-drilling thermal stress estimations were compared with "ground truth" measurements from temperature-compensated strain gages. In turn, the measured thermal stresses allowed to estimate the rail Neutral Temperature. The final results showed that the hole drilling technique has indeed the potential to determine the Neutral Temperature within the desired ±2.78° C (±5° F) accuracy with a 90% confidence interval within a realistic range of vertical residual stress levels.

The accuracy of the Neutral Temperature estimation depends on several factors, and primarily the assumed relationship between the longitudinal and the vertical residual stresses. Although this relationship depends on the rail rolling process, that is quite standardized in the industry, unavoidable differences may exist among different rail manufactures. Therefore, "calibrating" the residual stress field for a given rail manufacturer would likely yield the best compensation, in line with what found by magneto-elastic techniques [28].

The measurement of thermal stress in CWR would, of course, also be affected by the traditional sources of errors of hole-drilling measurements, including hole eccentricity, hole

depth measurement errors, and uncertainties from hole diameter and material properties, among others, which were not considered in this work. Finally, although the results presented in this study pertain to hole-drilling bonded strain gage rosettes, the measurements could be performed by non-contact means (e.g. optical techniques) as done in many other hole-drilling applications.

4.7 Acknowledgements

This chapter, in part, has been accepted by Experimental Mechanics, Zhu, Xuan; Lanza di Scalea Francesco. The title of this paper is **Thermal Stress Measurement in Continuous Welded Rails Using the Hole-Drilling Method**. The dissertation author was the primary investigator and primary author of this paper.

5 . Conclusions and future works

5.1 Review of the research performed and summary of novel contributions

This dissertation focuses on the thermal stress measurement in structures, particularly, the CWR, using both non-destructive and semi-destructive methods.

As a non-destructive method, the EMI technique features easiness of implementation, and low-cost implementation. A novel comprehensive analytical model is proposed to incorporate shear-lag behavior for the PZT-structure strain transfer, the nonlinear piezoelectric constitutive relations through effective dielectric and piezoelectric constants to account for the prestress/temperature in the PZT element, and the point-wise dynamic stiffness of the host structure subjected to the PZT spatially hyperbolic excitation. This model was not existent before. The modelling effort allows to predict the behavior of the EMI signature including structural resonances, capacitance and electric resonances both under uniaxial loading and temperature influences.

The variations of the EM susceptance were experimentally observed, and were unexplained in prior studies. Also, it is the first time that the electrical resonance was explored as a stress indicator for EMI measurements. The effectiveness of the proposed model was validated by its close agreements with the experimental results from both the uniaxial loading test (stress only) and the environmental chamber test (temperature only). Based on the analytical and experimental studies, selected features across the full EMI spectrum were

investigated for thermal stress characterization, including the conventional structural resonances, the in-plane and out-of-plane PZT resonances, the electrical resonance, and the capacitance of the PZT. Regression analysis and the Principal Component Analysis were successfully implemented to suppress the temperature influences on the features, and highlight the role of the stress.

As the semi-destructive method, this study has examined the hole-drilling method to estimate the in-situ longitudinal thermal stresses in CWR, and therefore the rail Neutral Temperature. A series of FEAs were first conducted to compute the updated calibration coefficients for the finer hole depth increments required by drilling in the hard rail steel so as to avoid plastic deformations and drill bit erosion. The feasibility of using the hole-drilling method for thermal stress measurements was validated by comparing the applied thermal stress with the stress relaxation obtained numerically from a 2-step nonlinear FEA, that projected the thermal stress field from a constrained intact geometry to a constrained geometry with a blind hole. In order to compute the calibration coefficients with the finer depth increments, a 3-D FEA that accounted for traction terms at the entirety of the hole boundaries (hole wall and bottom) was conducted, and the results were compared with the applicable ASTM standard and with a more simplified 3-D FEA that only considered the hole wall. This updated set of calibration coefficients was also experimentally validated on a thick aluminum plate subjected to a uniaxial uniform tensile load in an MTS machine.

The linear relationship between the longitudinal and the vertical residual stress components of the residual stress profile at rail neutral axis was established, which was statistically interpreted and tested with a two-sided test with the goal of a 90% confidence interval. Based on this relationship, the longitudinal residual stress component was subtracted from the total longitudinal stress of the in-service CWR relieved by hole-drilling. The hole-drilling thermal stress estimations were compared with "ground truth" measurements from temperature-compensated strain gages. In turn, the measured thermal stresses allowed to estimate the rail Neutral Temperature. The final results showed that the hole drilling technique has indeed the potential to determine the Neutral Temperature within the desired $\pm 5^{\circ}$ F accuracy with a 90% confidence interval within a realistic range of vertical residual stress levels.

5.2 Recommendations for future studies

This dissertation concludes that it is possible to characterize the thermal stress by using the impedance-based monitoring system, given a known initial stress state; and it is also feasible to determine the rail neutral temperature by using the hole-drilling method with appropriate calibration procedure to eliminate the effect of residual stresses.

For the EMI method, the potential nonlinear features based on the admittance signatures should be investigated further to determine their sensitivity to thermal stress, and

potentially extended for damage detection. The analytical/numerical models of the in-plane and out-of-plane PZT resonances should be further studied, along with their sensitivities to applied mechanical load, temperature and local damage. Since the EMI method is sensitive to environmental and operational variability, the uncertainties quantification of the EMI method should be established to discriminate the signature variations led from the change of structural integrity or the non-structural variability.

The *in-situ* stress determination framework based on hole-drilling method relies on the assumption of the residual stress that is uniformly distributed through the hole depth. The possible non-uniform residual stress along the drilling depth shall be further investigated, such that in the effort to advance to a reference-free method, which will require no calibration procedure. The measurement of thermal stress in CWR are also affected by the traditional sources of errors of hole-drilling measurements, including hole eccentricity, hole depth measurement errors, and uncertainties from hole diameter and material properties, among others, which were not considered in this work. A more comprehensive uncertainty analysis should be performed for future study. Finally, if the procedure of bonding strain gages is found to be impractical in the railroad maintenance procedures, effective means of measuring the hole drilling relieved strains (e.g. optical techniques) can be considered for this application

References

1. Liang C, Sun FP, Rogers CA (1994) Coupled electro-mechanical analysis of adaptive material systems determination of the actuator power consumption and system energy transfer. J Intell Mater Syst Struct. doi: 10.1177/1045389X9400500102

2. Liang C, Sun FP, Rogers CA (1996) Electro-mechanical impedance modeling of active material systems. Smart Mater Struct 5: 171–186

3. Zhou S, Liang C, Rogers CA (1996) An Impedance-Based System Modeling Approach for Induced Strain Actuator-Driven Structures. Journal of Vibration and Acoustics. doi:10.1115/1.2888185

4. Giurgiutiu V, Zagrai AN (2000) Characterization of Piezoelectric Wafer Active Sensors. J Intell Mater Syst Struct. doi: 10.1106/A1HU-23JD-M5AU-ENGW

5. Park G, Inman DJ (2007) Structural health monitoring using piezoelectric impedance measurements. Phil Trans R Soc A. doi: 10.1098/rsta.2006.1934

6. Bhalla S, Soh CK (2004) Electromechanical Impedance Modeling for Adhesively Bonded Piezo-Transducers. J Intell Mater Syst Struct. doi: 10.1177/1045389X04046309

7. Giurgiutiu V, Rogers CA (1998) Recent advancements in the electromechanical (E/M) impedance method for structural health monitoring and NDE. Proc SPIE 3329, Smart

   Structures and Materials 1998: Smart Structures and Integrated Systems. doi: 10.1117/12.316923

8. Mathar J (1934) Determination of initial stresses by measuring the deformation around drilled holes. Trans ASME 56: 4, 249–254

9. Beaney E M (1976) Accurate measurement of residual stress in any steel using the centre hole method. Strain 12: 3, 99–106

10. American Society for Testing and Materials (2008) Determining residual stresses by the hole-drilling strain-gage method. ASTM Standard test method E837-08

11. American Society for Testing and Materials (2013) Determining residual stresses by the hole-drilling strain-gage method. ASTM Standard test method E837-13a

12. Vishay Measurements Group Inc. (1996) Measurement of residual stresses by the hole drilling strain-gage method. http://www.vishaypg.com/docs/11053/tn503.pdf

13. Schajer G S (2010) Hole-Drilling Residual Stress Measurements at 75: Origins, Advances, Opportunities. Experimental Mechanics, pp 50:245, 253

14. Rendler N J, Vigness I (1966) Hole-drilling strain-gage method of measuring residual stresses. Experimental Mechanics, 6:12, 577-586

15. Schajer G S (1981) Application of finite element calculations to residual stress measurements. J Eng Mater Technol, 103: 2, 157–163

16. Schajer G S (1988) Measurement of non-uniform residual stresses using the hole-drilling

method. J Eng Mater Technol, 110: 4, Part I: 338–343, Part II: 344–349

17. Aoh J, Wei C (2002) On the improvement of calibration coefficients for hole-drilling integral method: Part I, Analysis of calibration coefficients obtained by a 3-D FEM model. J. Eng. Mater. Technol., 124: 2, 250
18. Xiao B, Li K, Rong Y (2011) Automatic determination and evaluation of residual stress calibration coefficients for hole-drilling strain gauge integral method. Strain, DOI: 10.1111/j.1475-1305.2009.00650.x
19. Schajer G S (1991) Strain data averaging for the hole-drilling method. Exp. Tech., 15:2, 25-28.
20. http://safetydata.fra.dot.gov/officeofsafety/publicsite/Query/inccaus.aspx
21. http://www.ntsb.gov/investigations/AccidentReports/Reports/RAR0302.pdf
22. http://columbiariverkeeper.org/featured/coal-train-derails-near-pasco/
23. http://articles.chicagotribune.com/2012-07-17/news/chi-union-pacific-officialsglenview-residents-meet-over-fatal-train-derailment-20120716_1_train-derailment-train-cars-fatal-derailment
24. Federal Railroad Administration (2016) Broad Agency Announcement BAA-2016: Research initiatives in support of rail safety. https://www.fra.dot.gov/eLib/Details/L17360. Accessed 7 June 2016
25. Association of American Railroads (AAR) / Transportation Technology Center, Inc. (TTCI) (2012) Railway technology needs: a 20-year perspective. Research Review of the Federal Railroad Administration, Washington, DC, May 22
26. Kerr A (1978) Analysis of thermal track buckling in the lateral plane. Acta Mechanica, 30, 17–50.
27. Tunna J (2000) Vertical rail stiffness equipment (VERSE) trials. Letter Report for Vortex International Transportation Technology Center, Inc. (TTCI), Pueblo, CO
28. Hayes A P (2008) MAPS-SFT, a new tool in the infrastructure manager's toolbox. Railway Condition Monitoring, 2008 4th IET International Conference, 18-20 June 2008, ISSN: 0537-9989
29. Hurlebaus S (2011) Determination of longitudinal stress in rails. Final Report Safety IDEA Project 15, Transportation research Board, Washington, DC
30. Nucera C, Lanza di Scalea F (2014). Nondestructive measurement of neutral temperature in continuous welded rails by nonlinear ultrasonic guided waves. J Acoust Soc Am 136:5, 2561-2574
31. Kelleher J, Prime M B, Buttle D, Mummery P M, Webster P J, Shackleton J, Withers P J (2003) The measurement of residual stress in railway rails by diffraction and other methods. J Neutr Res 11:4, 187-193.

32. Park S, Lee J, Yun C, Inman DJ (2008) Electro-Mechanical Impedance-based Wireless Structural Health Monitoring Using PCA-Data Compression and k-means Clustering Algorithms. J Intell Mater Syst Struct. doi: 10.1177/1045389X07077400

33. Yang Y, Liu H, Annamdas VGM, Soh CK (2009) Monitoring damage propagation using PZT impedance transducers. Smart Materials and Structures. doi: 10.1088/0964-1726/18/4/045003

34. Kim JT, Park JH, Hong DS, Cho HM, Na WB, Yi JH (2009) Vibration and impedance monitoring for pre-stress loss prediction in PSC girder bridges. Smart Structures and Systems. doi: 10.12989/sss.2009.5.1.081

35. Mascarenas DL, Todd MD, Park G, Farrar CR (2007) Development of an Impedance-based wireless sensor node for structural health monitoring. Smart Materials and Structures 16 6: 2137-2145

36. Datasheet for AD5933 (2005) http://www.analog.com/media/en/technical-documentation/data-sheets/AD5933.pdf. Accessed March 13th 2016

37. Ho D, Nguyen K, Yoon H, Kim JT (2012) Multiscale Acceleration-Dynamic Strain-Impedance Sensor System for Structural Health Monitoring. International Journal of Distributed Sensor Networks. doi:10.1155/2012/709208

38. Yang Y, Xu J, Soh CK (2005) Generic Impedance-Based Model for Structure-Piezoceramic Interacting System. Journal of Aerospace Engineering 18: 93-101

39. Giurgiutiu V, Zagrai AN (2002) Embedded Self-Sensing Piezoelectric Active Sensors for On-line Structural Identification. Journal of Vibration and Acoustics. doi:10.1115/1.1421056

40. Ong CW, Yang Y, Naidu ASK, Lu Y, Soh CK (2002) Application of the electro-mechanical impedance method for the identification of in-situ stress in structures. Proc SPIE 4935, Smart Structures, Devices, and Systems: 503–514

41. Annamdas VGM, Yang Y, Soh CK (2007) Influence of loading on the electromechanical admittance of piezoceramic transducers. Smart Materials and Structures. doi:10.1088/0964-1726/16/5/045

42. Phillips R, Zhu X, Lanza di Scalea F (2012) The Influence of Stress on Electro-mechanical Impedance Measurements in Rail Steel. Materials Evaluation 70: 1213-1218

43. Lim YY, Soh CK (2012) Effect of Varying Axial Load Under Fixed Boundary Condition on Admittance Signatures of Electromechanical Impedance Technique. J Intell Mater Syst Struct. doi:10.1177/1045389X12437888

44. Crawley EF, de Luis J (1987) Use of piezoelectric actuators as elements of intelligent structures. AIAA Journal. doi: 10.2514/3.9792

45. Lanza di Scalea F, Salamone S (2008) Temperature effects in ultrasonic Lamb wave structural health monitoring systems. J Acoust Soc Am. doi: 10.1121/1.2932071

46. Hall DA (2001) Review nonlinearity in piezoelectric ceramics. Journal of Materials Science 36: 4575-4601

47. Krueger HHA (1967) Stress sensitivity of piezoelectric ceramics: Part 1. Sensitivity to compressive stress parallel to the polar axis. J Acoust Soc Am 42: 636-645

48. Krueger HHA (1968) Stress sensitivity of piezoelectric ceramics: Part 3. Sensitivity to compressive stress Perpendicular to the polar axis. J Acoust Soc Am 43: 583-591

49. Lynch CS (1996) The effect of uniaxial stress on the electro-mechanical response of 8/65/35 PLZT. Acta Mater. doi:10.1016/S1359-6454(96)00062-6

50. Sherrit S, Stimpson RB, Wiederick HD, Mukherjee BK (1998) Stress and temperature dependence of the direct piezoelectric charge coefficient in lead zirconate titanate ceramics. Proc SPIE.doi:10.1117/12.305584

51. Sherrit S, Van Nice DB, Graham JT, Mukherjee BK, Wiederick HD (1992) Domain wall motion in piezoelectric materials under high stress. Proceedings of the Eighth IEEE International Symposium. doi:10.1109/ISAF.1992.300653

52. Zhang QM, Zhao J (1999) Electromechanical properties of lead zirconate titanate piezoceramics under the influence of mechanical stresses. IEEE transactions on ultrasonics, ferroelectrics and frequency control. doi: 10.1109/58.808876

53. Wang QM, Zhang T, Chen Q, Du XH (2003) Effect of DC bias field on the complex materials coefficients of piezoelectric resonators. Sensors and actuators A. doi:10.1016/j.sna.2003.08.008

54. Beige H, Schmidt G (1982) Electromechanical resonances for investigating linear and nonlinear properties of dielectrics. Ferroelectrics 41: 39-49

55. Aleksandrov KS, Zaitseva MP, Sysoev AM, Kokorin YI(1982) The piezoelectric resonator in a dc electric field. Ferroelectrics. doi: 10.1080/00150198208210608

56. Baumhauer JC, Tiersten HF (1973) Nonlinear electroelastic equations for small fields superposed on a bias. J Acoust Soc Am 54: 1017-1034

57. Tiersten HF (1978) Perturbation theory for linear electroelastic equations for small fields superposed on a bias. J Acoust Soc Am 64: 832-837

58. Chee CYK, Tong L, Steven GP (1998) A review on the modelling of piezoelectric sensors and actuators incorporated in intelligent structures. J Intell Mater Syst Struct. doi: 10.1177/1045389X9800900101

59. Ljamov VE (1972) Nonlinear acoustical parameters of piezoelectric crystals. J Acoust Soc Am 52:199-202

60. Kang HD, Song WH, Sohn SH, Jin HJ, Lee SE, Chung YK (2006) Polarization state-dependent stress effect on the dielectric properties of lead zirconate titanite thin films. Applied Physics Letters. doi: 10.1063/1.2198801

61. Rao SS (2004) Mechanical vibrations. Pearson Prentice Hall, Upper Saddle River, New Jersey 07458

62. Zhu X, Rizzo P (2012) A unified approach for the structural health monitoring of waveguides. Structural health monitoring. doi:10.1177/1475921712438569

63. Zhu X, Lanza di Scalea F, Fateh M (2014) Temperature and axial stress effects in electro-mechanical impedance method-based structural health monitoring. Proc. SPIE 9064, Health Monitoring of Structural and Biological Systems 2014. doi:10.1117/12.2045111

64. APC International, Ltd. (2016) Physical and piezoelectric properties of APC materials. https://www.americanpiezo.com/apc-materials/piezoelectric-properties.html. Accessed 7 June 2016

65. Foster FS, Ryan LK, Turnbull DH (1991) Characterization of lead zirconate titanate ceramics for use in miniature high-frequency (20-80 MHz) transducers. IEEE Transactions on Ultrasonics, Ferroelectrics, and Frequency Control. doi: 10.1109/58.84289

66. Briot R, Gonnard P, Troccaz M (1990) Studies on dielectric and mechanical properties of PZT doped ceramics, using a model of losses. Applications of Ferroelectrics 1990 IEEE 7th International Symposium. doi: 10.1109/ISAF.1990.200319

67. Yang G, Ren W, Liu S F, Masys A J, Mukherjee B K (2000) Effects of uniaxial stress and dc bias field on the piezoelectric, dielectric, and elastic properties of piezoelectric ceramics. Ultrasonics Symposium, 2000 IEEE. doi: 10.1109/ULTSYM.2000.921494

68. H Sohn, Effects of environmental and operational variability on structural health monitoring. Phil. Trans. R. Soc. A (2007) 365, 539-560

69. H Sohn, M Dzwonczyk, E G Straser, A S Kiremidjian, K H LAW, T Meng. An experimental study of temperature effect on modal parameters of the Alamosa canyon bridge. *Earthquake Engng. Struct. Dyn.* 28, 879-897 (1999)

70. B Peeters, G De Roeck. One-year monitoring of the Z24-Bridge: environmental effects versus damage events. *Earthquake Engng Struct. Dyn.* 2001; 30:149-171

71. B Peeters, J Maeck and G De Roeck. Vibration-based damage detection in civil engineering: excitation sources and temperature effects. *Smart Mater. Struct. 10* (2001) 518–527

72. H Sohn, C Farrar, N Hunter, K Worden. Applying the LANL statistical pattern recognition paradigm for structural health monitoring to data from a surface-effect fast patrol boat. LA-13761-MS

73. H Sohn, K Worden, C R Farrar. Statistical damage classification under changing environmental and operational conditions. *Journal of intelligent material systems and structures*, 13, 561-574

74. Manson, G. 2002 Identifying damage sensitive, environment insensitive features for damage detection. In Proc. of the IES Conf., Swansea, UK.

75. C K Oh, H Sohn. Damage diagnosis under environmental and operational variations using unsupervised support vector machine. Journal of sound and vibration, 325, 2009, 224-239

76. D Hong, K Nguyen, I Lee, J T Kim. Temperature-compensated damage monitoring by using wireless acceleration-impedance sensor nodes in steel girder connection. International Journal of distributed sensor networks, Vol. 2012, doi: 10.1155/2012/167120

77. N Sepehry, M Shamshirsz, F Abdollahi. Temperature variation effect compensation in

impedance based structural health monitoring using neural networks. Journal of Intelligent Material Systems and Structures

78. H J Lim, M K Kim, H Sohn, C Y Park. Impedance based damage detection under varying temperature and loading conditions. NDT&E International 44 (2011) 740-750

79. Park, S., Lee, J., Yun, C., Inman, D. J. (2008). Electro-Mechanical Impedance-based Wireless Structural Health Monitoring Using PCA-Data Compression and k-means Clustering Algorithms. J. Intell. Mater. Syst. Struct., 19.

80. C. Pardo De Vera, J. A. Guemes. Embedded self-sensing piezoelectric for damage detection. Proc International workshop on SHM, Stanford, 445-455, 1997.

81. K. Koo, S. Park, J. Lee, C. Yun. Automated impedance-based structural health monitoring incorporating effective frequency shift for compensating temperature effects. Journal of intelligent material systems and structures, Vol. 20, March 2009.

82. F. G. Baptista, J. V. Filho, D. J. Inman. Real-time multi-sensors measurement system with temperature effects compensation for impedance-based structural health monitoring. Structral Health Monitoring, 11(2) 173-186, 2011.

83. Park, G., Kabeya, K., Cudney, H. H., Inman, D. J. (1999). Impedance Based Structural Health Monitoring for temperature Varying Applications. JSME International Journal, 2, 42.

84. Lee, H.-L. , and Saravanos, D. A. (1998). "The effect of temperature dependent material properties on the response of piezoelectric composite materials," J. Intell. Mater. Syst. Struct. 9, 503–508.

85. Tiersten, H. F., "Thickness vibrations of piezoelectric plates". J. Acoustic Society of America, 35, 53-58 (1963).

86. T. Kamas, V. Giurgiutiu, B. Lin. Thickness mode EMIS of constrained proofmass piezoelectric wafer active sensors. Smart Material and structures, 24 (2015)

87. Schajer G S, Altus E (1996) Stress calculation error analysis for incremental hole-drilling residual stress measurements. J. Eng. Mater. Technol. 118(1), 120-126

88. Ajovalasit A, Scafidi M, Zuccarello B, Beghini M, Bertini L, Santus C, Valentini E, Benincasa A, Bertelli L (2010) The hole-drilling strain gauge method for the measurement of uniform or non-uniform residual stresses. Working Group on Residual Stresses, AIAS TR-01:2010

89. Scafidi M, Valentini E, Zuccarello B (2011) Error and uncertainty analysis of the residual stresses computed by using the hole drilling method. Strain, 47:4, 301–312

90. http://resources.schoolscience.co.uk/Corus/16plus/steelch3pg4.html. Accessed 9 March 2016

91. Kelleher J, Prime M B, Buttle D, Mummery P M, Webster P J, Shackleton J, Withers P J (2002) The measurement of residual stress in railway rails by diffraction and other methods. Journal of Neutron Research, 11(4), 187-193, 2003

92. Kutner M H, Nachtsheim C J, Neter J, Li W (2004) Applied linear statistical models. McGraw-Hill/Irwin ISBN-10: 007310874X